UNIVERSITY of the WESTERN CAPE

A STUDY OF HIGH-GRADE CALC-SILICATE ROCKS IN THE SOUTHERN BUSHMANLAND DOMAIN, NAMAQUA METAMORPHIC PROVINCE, INCLUDING THE GARIES WOLLASTONITE DEPOSIT

By

Carmenlite van Wyk

Thesis submitted in fulfilment of the requirements for the degree of Master of Science in the Faculty of Natural Sciences at the University of the Western Cape

Supervisor: Dr. Juergen Reinhardt

Department of Earth Sciences

February 2023

Declaration

I, Carmenlite van Wyk, hereby declare that this Masters (MSc.) thesis, submitted to the Faculty of Natural Sciences at the University of the Western Cape, is my work and has not been previously submitted either entirely or partly to any other university or institution of higher education for obtaining a qualification.

Signature: _____

Date: 21 February 2023   Place: Brackenfell, Cape Town, South Africa

i

Abstract

In the Namaqualand region, Northern Cape, South Africa, calc-silicate rocks are present in the highest-grade metamorphic zone (upper amphibolite to granulite facies) of the southern Bushmanland Domain, Namaqua Province. Minor amounts of calc-silicate rocks occur as small isolated discontinuous layers, pods and lenses in the investigated area just outside of Kliprand, while the Garies area exposes a larger occurrence of calc-silicate rocks which involves relatively pure concentrations of wollastonite that are presently mined. Both these sites are characterised by wollastonite-rich calc-silicate assemblages. The rocks from these areas provide a unique opportunity to study the physical conditions and fluid regime of granulite facies metamorphism in the Bushmanland Domain. Mineral chemistry and petrology of fifty calc-silicate samples from the Garies area were studied in detail, and twenty calc-silicate samples from the Kliprand area were studied for comparison to constrain the P-T conditions of granulite facies metamorphism and understand the characteristics of fluid compositions.

The Kliprand banded calc-silicate pod occurs as an isolated outcrop bounded by granulite facies quartzofeldspathic gneiss that experienced peak metamorphic temperatures at 800-870°C. The calc-silicate pod is dominated by scapolite, diopside, quartz, calcite, wollastonite, K-feldspar and plagioclase. The Garies wollastonite quarry represents the largest known economic wollastonite occurrence in South Africa. The quarry is dominated by wollastonite, garnet, diopside, calcite and vesuvianite and is surrounded by high-grade granulitic gneiss that experienced peak metamorphic temperatures at 800-860°C. In conformity with previous studies the pressure gradient in both areas (Kliprand and Garies) is estimated at 5 kbar and 4-6 kbar respectively. The Garies calc-silicates are divided into five rock groups (CS1, CS2, CS3, CS4 and M1), with each rock group containing a different mineral assemblage. Major critical assemblages include Cal + Wo + Di + Grt +Ves ± Ttn ± Ep (CS1), Grt + Di + Ves + Wo ± Fld ± Cal (CS2), Grt + Di + Ves ± Wo ± Cal ± Mc (CS3), Grt + Ves ± Di ± Prh (CS4) and Mc + Grt + Hbl+ Di ± Ttn (M1). Mineral analyses have been obtained for all major phases of the calc-silicate rocks, including clinopyroxene, wollastonite, vesuvianite and garnet. Two generations of garnet were identified which included a group of homogeneous, isotropic and anhedral garnets, and a less common group of garnets that displayed distinctive zonation patterns and were more heterogeneous and birefringent. Mineral parageneses and T-X_{CO2} diagrams imply that the

calc-silicate assemblages from the two different localities (Kliprand and Garies) do not so much reflect different P-T conditions, but are rather due to highly contrasting CO_2 activities ($X_{CO2} > 0.5$ and $0.2 < X_{CO2} > 0.15$ respectively). This is expressed by the abundance of vesuvianite and grossular at Garies versus absence of those two phases and abundance of scapolite at Kliprand. Due to lithological evidence and previous studies, it is implied that the Garies calc-silicate rocks represent a hydrothermal skarn which developed through water-rock interaction between the carbonate wall rock and a felsic magma. The rocks from the Garies area equilibrated under externally buffered H_2O-rich conditions, probably due to fluid infiltration from the surrounding gneisses during prograde metamorphism. In contrast, mineral assemblages of the Kliprand calc-silicate pod equilibrated under CO_2-rich fluid conditions, internally controlled by CO_2 release from reactive layers within the pod.

Acknowledgments

Table of Contents

List of Figures

UNIVERSITY *of the*

WESTERN CAPE

List of Tables

1. Chapter 1: Introduction and previous work

1.1. Introduction

Calc-silicate rocks are metamorphic rocks that consist mainly of Ca-Mg-Fe-Al silicate minerals such as diopside, grossular, Ca-amphiboles, vesuvianite, epidote and wollastonite (Winter, 2010). Calc-silicate rocks are also known to contain a wide range of mineral parageneses and textures, and, apart from the previously mentioned minerals, they contain additional mineral phases such as plagioclase, accessory apatite and zircon (De Jager and Simpson, 1962). These rocks can form by metamorphism of impure carbonate rocks, such as limestone or dolomite that contain substantial amounts of clays and quartz (SiO_2) in addition to calcite ($CaCO_3$) and dolomite ($CaMg(CO_3)_2$), (Best, 2003). Based on the chemical composition of the original rock, calcareous protoliths can either be metamorphosed to marble (dolomitic marble, calcitic marble) if the original protolith is pure dolomite/pure limestone or calc-silicate rocks if the protolith contains silicate minerals. Additionally, calc-silicate rocks can be produced through metasomatism in contact metamorphic aureoles between carbonate country rocks and hydrothermal silica-saturated fluids, sourced from a hot, hydrous, silicate intrusion such as granite (Barker, 1998; Winter, 2010). Calc-silicate rocks that formed through metasomatic processes are more commonly referred to as skarns.

Metamorphism of impure carbonate rocks involves several devolatilization reactions (decarbonisation and dehydration reactions) which are dependent on the pressure, temperature, rock composition and the composition of the associated pore fluid. Impure carbonates comprising dolomite, calcite and silica (chert, detrital quartz or SiO_2 in solution) corresponds to the simple-five-component system: $CaO-MgO-SiO_2-H_2O-CO_2$ (Winter, 2010). As the number of constituents increases, the chemical composition and mineralogical composition become more complex and variable, requiring a more comprehensive approach to calc-silicate petrogenesis. For example, the addition of components such as Al_2O_3, FeO, Na_2O and K_2O causes the introduction of several new phases, hence the chemical system can become very complex (Winter, 2010). In general, calc-silicate rocks are known to provide specific information on metamorphic processes, such as:

1

(1)   information on fluid compositions as they preserve reaction textures in response to changes in the P-T-fluid history (Satish-Kumar and Harley, 1998).

(2)   They preserve peak P-T conditions quite well due to their ability to preserve characteristic mineral assemblages representing peak metamorphic conditions (Harley and Buick, 1992).

(3)   They have higher solidus temperature than, for example, metapelitic rocks, which means they remain in a solid-state at granulite facies temperatures; Therefore, unlike metapelites, their bulk composition will not be modified by partial melting.

(4)   They are geochemically quite distinct from their associated clastic-derived metasedimentary rocks, thus helping us to understand the mobility of elements and metasomatism in the lower crust (Buick et al., 1993; Ferry, 1992).

This study focuses on the regions within the Namaqualand area situated in the Northern Cape Province of South Africa. There are two locations featured in this study known for their abundant wollastonite-rich calc-silicate rocks. They include the wollastonite deposit near Garies and a small patch of calc-silicate rocks near Kliprand (Fig. 3). Garies and Kliprand are located approximately 446- and 430 km North of Cape Town, respectively. The emphasis of this study is on the Garies wollastonite mine, presently operated by Namwol, which is located 18 km outside of Garies and is the only active wollastonite mine in South Africa. The Garies wollastonite mine is also considered the largest-known wollastonite occurrence in South Africa.

Both of the investigated calc-silicate exposures are situated in the highest-grade metamorphic zone (upper amphibolite to granulite facies) of the southern Bushmanland Domain, Namaqua Province. The Namaqua Province forms part of the Namaqua-Natal Belt which is a Mesoproterozoic orogenic belt belonging to the global Grenville event during which the supercontinent Rodinia was assembled. The calc-silicate rocks of both study areas form part of the Kamiesberg Group within the Bushmanland Domain.

In the Bushmanland Domain, calc-silicate rocks mainly occur as small isolated discontinuous layers, pods and lenses and are commonly observed in association with other supracrustal rocks such as pelitic and semi-pelitic gneisses (Macey et al., 2011). In the Garies area, calc-

silicate rocks are well exposed through mining activity with small isolated pods and lenses located further away from the mined quarry.

Although calc-silicate rocks are mainly found to be minor in occurrences, they tend to have the ability to preserve essential information, such as the formation of solid solution and exsolution structures which can be related to the very high temperatures the host rocks experienced during metamorphism. These characteristics of calc-silicate rocks can be used to aid in the deduction of the metamorphic and deformational evolution of high-grade terrains (Satish-Kumar et al., 2006).

1.2. Background

1.2.1. Previous work on calc-silicate rocks in the Garies and Loeriesfontein areas

Previous work carried out by De Beer (2010) and Macey et al. (2011) in the Namaqualand region included regional study, describing the entire geology of the Garies and Loeriesfontein areas along with the deformational and metamorphic history of the supracrustal rocks located in these areas. Their description includes occurrences, mineral assemblages and reaction textures of calc-silicate rocks observed. Occurrences of calc-silicate gneisses along with pretectonic pelitic, semipelitic and quartzitic gneisses are observed in supracrustal belts and lenses surrounded by voluminous granites and orthogneisses. According to Macey et al. (2011) the metasedimentary gneisses are associated with bands of heterogeneous migmatitic grey biotite gneisses, and together, these units form the Kamiesberg Group.

1.2.2. Specialised study on the Garies wollastonite deposit

Previous work carried out by Seto et al. (2006) included a detailed study of wollastonite collected at the Garies wollastonite mine. Studies included the description of chemical and crystallographic properties of clinopyroxene exsolution in wollastonite-bearing calc-silicate granulites, following a study by Hiroi et al. (2001) which included findings of diopside exsolution lamellae in wollastonite from Namaqualand granulites. Geological observations conducted by Waters (1986, 1991) and Nowicki et al. (1995) have characterized the highest-grade zone in which the wollastonite mine lies. This zone is defined by upper granulite facies conditions, with temperature and pressure (P-T) estimated to be between 800 and 860°C at 7 kbar according to Zelt (1980), and 800-860°C at 4-6 kbar according to Waters (1989). Nowicki et al. (1995) identified an osumilite locality suggesting a temperature of 870°C at 7

kbar. Seto et al. (2006) concluded that the exsolution of clinopyroxene lamellae in the studied wollastonite was a result of high-temperature conditions at the peak of upper granulite facies metamorphism and later exsolution, but no specific temperature was derived.

Harris and Maboane (2021) provided a detailed study of the Garies wollastonite deposit which focussed on stable isotopes. They concluded that the Garies wollastonite mine mineralogically and isotopically equilibrated at granulite facies conditions. However, according to their results, the $\delta^{18}O$ values in the minerals of the calc-silicate rocks were unusually low. Low- $\delta^{18}O$ values require interaction with $\delta^{18}O$ -depleted surface fluids, which must have occurred prior to peak metamorphism. Given the rarity of low- $\delta^{18}O$ rocks, especially low- $\delta^{18}O$ carbonates, Harris and Maboane (2021) suggested that it is most likely that the deposit represented a metamorphosed hydrothermal skarn that developed at the contact between the original carbonate rocks and intruding felsic magmas.

1.3. Problem statement

Apart from the specialised electron backscatter diffraction study on wollastonite from the Garies quarry locality carried out by Seto et al. (2006) and the study made by Harris and Maboane (2021), no detailed work has been done on any of the calc-silicate rocks in the Bushmanland Domain so far. Consequently, not enough basic petrographic data are available on these rocks. Because of the unique characteristics of calc-silicate rocks, they are considered suitable rocks for exploring the geodynamic evolution of high-grade terrains (Satish-Kumar et al., 2006) and can be tied in with a longer-term study of metamorphism and deformation in the high-grade Namaqua-Natal Belt.

1.4. Aims and objectives

Calc-silicate rocks tend to remain in a solid state at granulite-facies conditions and commonly preserve peak P-T conditions quite well. Therefore, the main aim of this study will be exploring the role of calc-silicate rocks to help constrain the peak and post-peak metamorphic data pertinent to the geodynamic evolution of high temperature and ultra-high-temperature metamorphic terrains, and the specific significance for the tectonic and thermal history of the Namaqua-Natal Belt. A comparison between exposures from Garies and Kliprand will be carried out, describing the differences and/or similarities in these rocks that can be incorporated in the deduction of the geodynamic evolution of this high-grade terrain.

4

1.5.   Methodology

The following steps describe the methodology followed from sampling to analytical work:

1.   Conduct fieldwork and sampling of the Garies wollastonite deposit and the associated rocks. The fieldwork involved investigating the extent of the wollastonite mineralisation and the related calc-silicate rocks, providing a description of the rocks surrounding the mine area, describing primary and secondary structures and the extent of metasomatism. A geological map of the area has been done. Mine access was provided by the mine manager, Conrad Stutte.

2.   Provide a detailed microscopic-petrographic analysis of the rocks, including the study of critical mineral equilibria and reaction textures. Standard thin sections and polished thin sections were prepared at the University of the Western Cape.

3.   Perform electron microprobe analyses of selected samples to obtain mineral compositions as well as compositional zoning profiles. These analyses are complemented by BSE images as well as compositional maps of minerals and multiphase rock domains.

Electron microprobe analyses (WDS) of the various minerals was carried out using the JEOL-8230 Superprobe housed at the Shared Instrument Facility (SIF) of Louisiana State University (LSU), by Dr Peter Horvath. Operating conditions included a 15 kV acceleration voltage, 20 nA probe current (except for titanite analysed at 100 nA), a focused beam was used for all analyses except for vesuvianite (5 micron) and titanite (10 micron). Both natural and synthetic minerals were used as standards as listed in Appendix 1.

4.   Evaluate metamorphic pressures and temperatures as well as fluid compositions (H_2O-CO_2).

5

Chapter 2: Geological setting

2.1. Regional Geology

2.1.1. The Namaqua-Natal Province

The 400 km wide and 1400 km long Namaqua-Natal orogenic belt (Fig. 1) consists of highly deformed medium- to high-grade metamorphic terranes that stretch from southern Namibia south-eastwards through the Northern Cape province of South-Africa to Kwazulu-Natal (McCourt et al., 2006). The Mesoproterozoic (ca. 1.3–1.0 Ga) Namaqua-Natal Metamorphic Province (NNMP) is described as a granitoid-rich orogen (Macey et al., 2018). Juvenile crust formation within the Namaqua-Natal Belt occurred during two principal periods at ~1.4 and ~2.2 Ga with little evidence for significant contributions from older crustal sources (Eglington, 2006). According to Cornell et al. (2006) the Namaqua-Natal Province is divided into two sectors, namely the Namaqua Sector in the west and the Natal Sector in the east. The Namaqua Natal Province is associated with the global Grenville orogenic event during which the supercontinent Rodinia was assembled, and covers the southern flanks of the Kaapvaal Craton. The Namaqua-Natal Province includes igneous and metamorphic rocks which were formed or deformed during the Namaquan Orogeny at approximately 1200- 1000 Ma. This study focuses on the Bushmanland Domain of the Namaqua Sector.
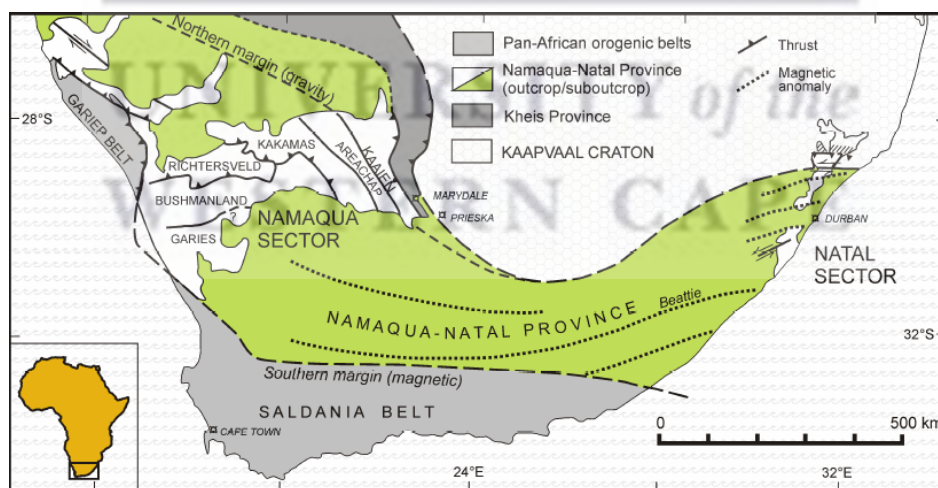
Figure 1: Geology of southern Africa showing the Namaqua-Natal Province, after Cornell et al. (2006).

2.1.2. The Namaqua Sector

The Namaqua Sector forms the western part of the Namaqua-Natal Province (Fig. 1) and covers an area of approximately 100000 km^2 (Cornell et al., 2006). The Namaqua Sector is a sequence of intensely deformed high-grade ortho- and para-gneisses and mafic granulites

6

that were intruded by large volumes of late-tectonic granitoids and minor post-tectonic noritoids. The polydeformed and polymetamorphosed granitic gneisses and supracrustal rocks comprising the Namaqua Sector developed during two major tectono-magmatic cycles in the Paleoproterozoic (2050 Ma to 1800 Ma) and Mesoproterozoic (1350 Ma to 950 Ma) (Clifford et al., 2004; Eglington, 2006; Cornell et al., 2006, 2009; Cornell and Pettersson, 2007; Thomas et al., 2016; Macey et al., 2017). Several large transcurrent faults which crosscut the Namaqua Sector, allow for the sector to be subdivided into different domains (Fig. 2) typically described as a stack of laterally extensive thin SW- directed thrust-bounded sheets. These sheets form individual tectonostratigraphic domains which are distinguished based on their lithostratigraphy, tectonic and metamorphic history (Hartnady et al., 1985; Thomas et al., 1994; Macey et al., 2017). The domains making up the Namaqua Sector are, from west to east: The Bushmanland Domain, the Richtersveld Magmatic Arc (Reid, 1979, 1997; Macey et al., 2017), the Kakamas Domain, the Areachap Domain, the Kaaien Domain and the Kheis Domain (Table 1). The largest tectonic domain of the Namaqua Sector is the Bushmanland Domain, also termed the Bushmanland Subprovince in other studies (e.g., Cornell et al., 2006; Macey et al., 2018).
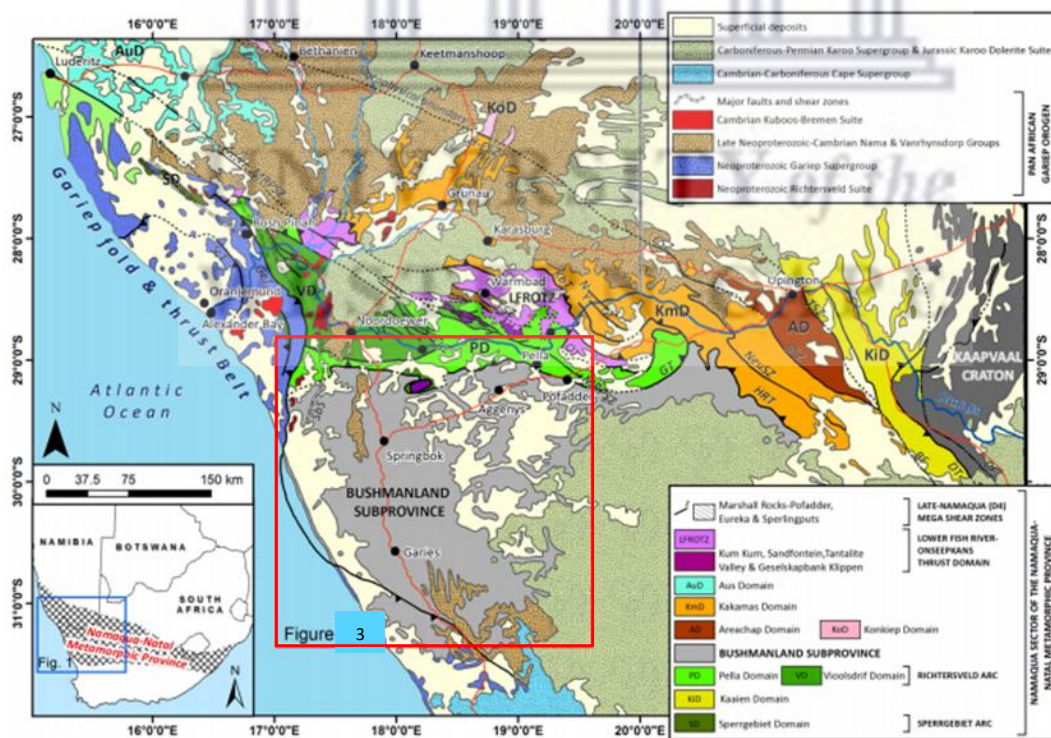
Figure 2: Regional geology of the Namaqua sector of the Namaqua-Natal Belt, compiled from Blignault et al. (1983), Hartnady et al. (1985) Thomas et al. (1994), Colliston and Schoch (1998), Moen and Toogood (2007), Miller (2008), Macey et al. (2015, 2017), Gresse et al. (2016) and Thomas et al. (2016). Red outlined area is shown in Fig. 3.

7

Table 1: Different divisions of the Namaqua Sector

Domain	Notes
Bushmanland	Forms the southerly and lowermost domain of the Namaqua Sector. North-western parts are dominated by 1.83 Ga Granitic gneisses and migmatites known as the Gladkop Suite while the remainder is dominated by pre- and post-tectonic Mesoproterozoic granites and discontinuous belts of high-grade paragneisses.
Richtersveld	Low- to medium grade Paleoproterozoic domain which contains the oldest crustal material in the Namaqua Sector. It is dominated by the 1.9 Ga Vioolsdrif Intrusive Suite which intruded the Orange River Group (Reid, 1979, 1997; Macey et al., 2017).
Kakamas	comprises lenticular rafts of granulite-facies meta-sedimentary rocks (~1220–1200 Ma) intruded by igneous rocks dated at between 1.21 and 1.08 Ga.
Areachap	Consists of 1.30–1.22 Ga arc-generated amphibolite-facies grade supracrustal rocks intruded by younger ~1.20 to ~1.10 Ga granitoids ((Geringer et al., 1986, 1994; Cornell et al., 1990, 2014; Pettersson et al., 2007; Cornell and Pettersson, 2007; Bailie et al., 2010, 2011, 2017).
Kaaien	Forms a tectonic transition zone between the Kaapvaal Craton and Kheis Province and the Namaqua Sector. It is composed of ~1.77 Ga metaquartzites, ~1.37 and 1.17–1.10 Ga bimodal volcano-sedimentary rocks and 1.10 Ga granitic intrusions (Van Niekerk, 2006; Bailie et al., 2012).
Kheis	The easternmost tectonic domain of the Namaqua Sector and represents a Mesoproterozoic thin-skinned fold and thrust belt deformed during the early stages of the Namaquan Orogeny (van Niekerk, 2006; Moen, 1999; Eglington, 2006).

2.1.3. The Bushmanland Domain
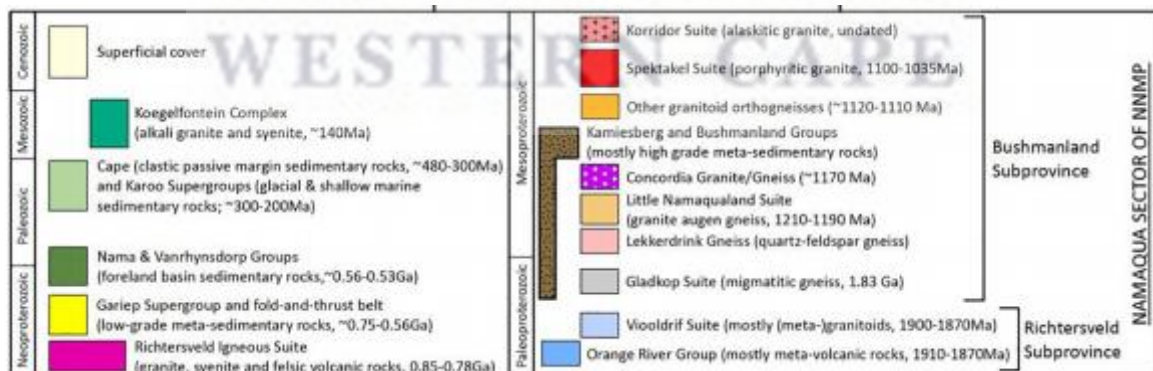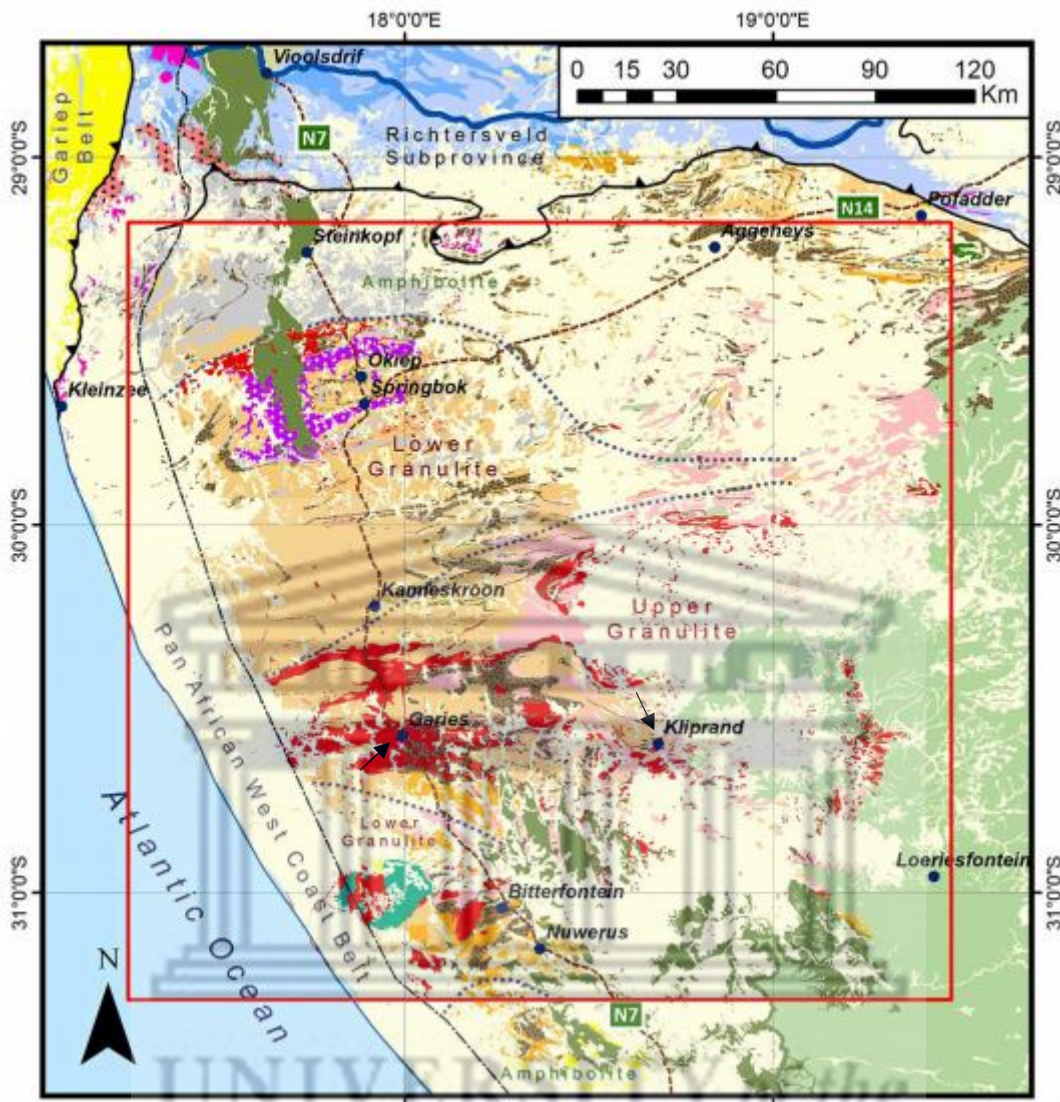
Figure 3: Geology of the Bushmanland Subprovince. Modified after Marais et al. (2001), De Beer et al. (2002), Agenbacht (2007), De Beer (2010) and Macey et al. (2011). Black arrows indicate location of study areas Garies and Kliprand.

The Bushmanland Domain is comprised of high-grade amphibolite- to granulite-facies supracrustal rocks (Fig. 3), early to mid-Proterozoic in age, as well as syn- to late- kinematic intrusives (Clifford et al. 1995; Robb et al. 1999). According to Cornell et al. (2006), the Bushmanland Domain covers an area of approximately 60 000 km², but is also known to be the most poorly exposed and thus, the least understood (Schmitz and Bowring, 2004). According to van Aswegen (1983) and Robb et al. (1999), the oldest units of the north-western parts of the Bushmanland Domain are dominated by 1.83 Ga granitic gneisses and migmatites known as the Gladkop Suite. The remainder of the Bushmanland Domain is subdivided into two units known as the Bushmanland and Kamiesberg Groups (Agenbacht, 2007; de Beer, 2010; Macey et al., 2011). The Bushmanland- and Kamiesberg Group has consistent lithostratigraphy, with extensive intrusions of pre- and post-tectonic Mesoproterozoic granites. These granites are interspersed with thin layers and bands of high-grade paragneisses (Marais et al., 2001; De Beer et al., 2002; Agenbacht, 2007; Moen and Toogood, 2007; de Beer, 2010; Macey et al., 2011). Recent studies have yielded a range of detrital age profiles (e.g., Raith et al., 2003; Bailie et al., 2007a; McClung, 2006; Cornell et al., 2009; Rudnick, 2016) indicating that further subdivision of these units will be required.

2.2. Local Geology

2.2.1. Kamiesberg Group

The exact age and origin of the supracrustal rocks of the Kamiesberg Group remain uncertain owing to limited geochronological data, Although, according to Raith et al. (2003) detrital zircon grains in the lowermost section of the Kamiesberg Group dated back to 1200-1250 Ma, prior to a tectonothermal event at 1187 Ma. In contrast, zircon grains in a metapelitic granulite from the upper Kamiesberg Group were deposited during an unrecognized sedimentation stage after 1157 Ma. The rocks comprising the Kamiesberg Group are Mesoproterozoic in age and include rocks such as metapelitic and semi-pelitic gneisses, metaquartzites, calc-silicate gneisses and migmatitic grey biotite gneisses (Albat, 1984; Macey et al., 2011). These rocks that make up the Kamiesberg Group were subjected to upper granulite facies metamorphism at about 750-800°C and pressures between 4.5-6 kbar (Waters, 1986, 1989; Raith and Harley, 1998) and are essentially products of incongruent partial melting (Waters, 1986, 1989). The ages of the intrusive rocks and the timing of the metamorphic peak has been fairly well constrained (Robb et al., 1999; Clifford et al., 2004;

Eglington, 2006). Between approximately 1200 Ma and 1030 Ma ago, the Kamiesberg Group was intruded by voluminous granitoids and minor mafic rocks currently known as the Little Namaqualand, Oorkraal, Spektakel and Koperberg Suites (De Beer, 2010).

Table 2: The geological subdivision pertaining to the intrusive and metamorphic rocks present in the Kamiesberg Group (Modified after De Beer (2010) and Macey et al. (2011))

age	Era	Supracrustal succession	Intrusive and metamorphic Rocks
1200 Ma	Mesoproterozoic	Kamiesberg Group	Koperberg Suite
			Spektakel Suite
			Oorkraal Suite
			Little Namaqualand Suite

2.2.2. Little Namaqualand Suite

The Little Namaqualand Suite intruded the Bushmanland Domain at approximately 1190-1150 Ma. It is dominated by granitoids and is pre- to syn-tectonic (Macey et al., 2011). According to de Beer, (2010) the Little Namaqualand Suite is characterised by strongly foliated and crenulated granite gneisses which is also a representation of the dominant granitoids found in the Garies area. Rocks from this suite are distinguished from the Spektakel Suite by the presence of alkali-feldspar- augen porphyroclasts (recrystallised K-feldspar megacrysts wrapped by a biotite-bearing matrix), multiple leucosome generations and penetrative ductile deformation (de Beer, 2010). These rocks are characterised by their strong penetrative and augen streaky gneiss fabrics and are typically leucocratic, occurring in shades of pale pink, cream and grey (Macey et al., 2011). Rock units associated with the Little Namaqualand Suite include the Mesklip-, Karebees-, Soetheuningberg-, Darter's Poort- and Langklip Gneisses.

2.2.3. Oorkraal Suite

The Oorkraal Suite is considered a pre-syn tectonic mafic intrusive suite, which intruded the Bushmanland Domain about 1160 Ma (Raith et al., 2003). It is characterised by pretectonic two pyroxene granulite rocks and amphibolites (De Beer, 2010) that are typically melanocratic black, fine- to medium-grained and have a moderate to strong granoblastic equigranular texture, with a locally compositionally banded gneissic texture (Macey et al., 2011). According to De Beer et al. (2002) the Oorkraal Suite is a group of mafic dykes and sills that intruded the Little Namaqualand Suite before the peak of D_2 deformation and according to Robb et al.

11

(1999) some of these dykes intruded about 100 m.yr. before peak metamorphism was reached.

2.2.4. Spektakel Suite

The Spektakel Suite is late- to post-tectonic and Mesoproterozoic in age. According to Bailie et al. (2019), the Spektakel Suite is 1.10-1.03 Ga in age. The Spektakel Suite is undeformed and characterised by a granitic composition, which is typically leucocratic (excluding charnockitic varieties), and essentially consisting of quartz, K-feldspar and plagioclase with minor mafic minerals of which biotite is the most common (Macey et al., 2011). According to Macey et al. (2018) the Spektakel Suite comprises mostly undeformed granites and charnockites that previous studies have dated between 1086 and 1033 Ma (Thomas et al., 1996; Ashwal et al., 1997; Robb et al., 1999; Grantham et al., 2000; Clifford et al., 2004). Eight major rock units are identified in the Spektakel Suite: the Garies Granite, Windpoort Granite, Jakkalshoek Granite, Strandfontein Granite, Banke Granodiorite, Kliphoek Granite, Paardekraal Granite and the Bloukop Granite.

2.2.5. Koperberg Suite

The Koperberg Suite is believed to have intruded the Bushmanland Domain approximately 1030 Ma. It is characterised as a mafic to intermediate intrusive suite which is dominated by melanocratic noritoids but also comprises a variety of rocks ranging from andesine anorthosite, biotite diorite, leuconorite, enderbrite (orthopyroxene tonalite), norite to melanorite hypersthenite (Andreoli et al., 1987; Clifford et al., 1995).

2.3. Deformation and metamorphism

The Namaqua-Natal Belt is characterised by five major tectonic events ($D_1 – D_5$) as described by Diener et al. (2017). D_1 is Paleoproterozoic in age and related to the c. 1905–1865 Ma Orange River Orogeny, while D_2-D_3 are Meso- to earliest Neoproterozoic in age (c. 1230–950 Ma) and related to the Namaqua Orogeny. D_5 is related to the Pan-African Gariep orogeny ranging from Late Neoproterozoic to Cambrian in age (Diener et al., 2017).

2.3.1. Deformational history of the Bushmanland Domain

Joubert (1971, 1986) established four tectonic phases in the Bushmanland Domain, while more recent studies carried out by Bailie et al. (2019) established four major ductile, and one brittle deformation phase. The D_1 tectonic phase is the oldest Paleoproterozoic phase and has

since been overprinted by a second deformational phase (D_2) leaving traces of it only preserved in the Richtersveld Domain and as relict structures in the Gladkop Suite in the northern Bushmanland Domain (van Aswegen, 1983; Macey et al., 2017). D_1 is characterized by intrafolial or tight isoclinal F_1 folds within the dominant gneissic banding (Joubert, 1971; Blignault et al., 1983; Albat, 1984). The D_2 deformational event is considered the regionally dominant tectonic phase (Cornell et al., 2006; Macey et al., 2011) and is characterised by heterogeneous, locally intense, subhorizontal fabric that is parallel to axial planes of tight to isoclinal, east-trending recumbent folds (Cornell et al., 2006). It is also characterised by a regional E-W-trending moderate to shallow dipping penetrative S_2 ductile foliation and an L_2 stretching lineation (Joubert, 1971, 1986) which was produced by regional folding during the Namaqua orogeny.

S_2 is pervasive and well developed in the Little Namaqualand Suite (Cornell et al., 2006) and is defined by elongated ENE-oriented K-feldspar augen porphyroclasts and preferred orientation of platy minerals such as biotite (Cornell et al., 2006; Macey et al., 2011). The L_2 elongation lineations are NW-trending in the southern Bushmanland Domain, following a change to a N-trend around the Garies area with the central and northern parts trending NE (Macey et al., 2018).

The fact that an S_2 planar fabric is found almost completely absent from the Spektakel Suite (except along the basal contact of the Concordia Granite) may imply that the D_2 tectonic event ended at approximately 1060 Ma (Cornell et al., 2006). This statement was supported by more regional studies conducted by Thomas et al. (1996); De Beer et al. (2002); Raith et al. (2003); Bailie et al. (2007a); Petterson, (2008) and Cornell et al. (2009). They have shown that the termination of the D_2 event must have been between 1110 and 1065 Ma.

The D_3 tectonic phase is characterised by E-W-trending F_3 folds which are associated with upright to inclined shallow-plunging open folds (Macey et al., 2011). Accompanying the D_3 event is an S_3 planar fabric, described as a non-penetrative, discrete sub-vertical planar cleavage. According to Albat, (1984); Kisters et al. (1994); Macey, (2001) and Macey et al. (2011) the S_3 planar fabric developed due to shearing along the limbs of minor F_3 folds and is filled with leucosomes composed of quartz-feldspar ± biotite ± magnetite.

The D_4 tectonic deformational event is characterised by large-scale, NW- trending, sub-vertical transcurrent shear zones with right-lateral movements as evident in reoriented S_2 and S_3 foliations (Albat, 1984; Macey, 2001). According to Macey et al. (2011), D_5 is a brittle deformational event associated with NNW-trending faults.

2.3.2. Metamorphic History of the Bushmanland Domain

Supracrustal rocks from the Bushmanland Domain are characterised by high-grade metamorphic conditions ranging from upper amphibolite to granulite facies. According to Waters, (1986, 1989) the northern, northeastern and southern sectors of the Bushmanland Domain are defined by upper amphibolite metamorphic conditions ranging from 650-700°C while the ENE-trending belt around the Garies-Kliprand area in the south is defined by upper granulite facies conditions with temperatures reaching approximately 830°C (Waters, 1991).

Field observation and the interpretation of mineral assemblages, particularly in the Southern Bushmanland Domain (SBD), supported an anti-clockwise P-T-t path attaining upper granulite facies conditions, with temperatures of ~750–870°C and pressures of 4.5–6 kbars (Albat, 1984; Waters, 1986, 1989; Baars, 1990), during late- to post-kinematic times (~1.02–1.03 Ga) (Raith et al., 2003).

Metamorphism during the Namaquan orogeny, specifically the major episodes (M_2, M_3), is commonly correlated with the major ductile- deformational events (D_2, D_3). It is observed that metamorphism typically occurs subsequent to these major deformational events. The highest-grade metamorphism in the Bushmanland Domain occurred at around 1030 Ma (M_3, e.g., Robb et al., 1999; Eglington and Armstrong, 2003; Bailie et al., 2007a, b; Cornell et al., 2009), 35 to 80 m.yr. after the termination of the main, regional amphibolite grade metamorphism of the Namaqua orogeny M_2. The M_2 metamorphic event is reported to have occurred at ~1.19–1.17 Ga in the northern Bushmanland Domain. The timing of M_2 amphibolite facies metamorphism in the southern Bushmanland Domain remains poorly constrained, but likely also occurred at ~1.22–1.18 Ga (Raith et al., 2003), similar to that in the northern Bushmanland Domain. According to Raith et al. (2003) M_3 coincides with the emplacement of the post-tectonic members of the Spektakel Suite and the nickeliferous mafic rocks of the Koperberg Suite, but was subsequent to the D_2 deformation event.

According to Waters (1986, 1989) the earlier M_2 metamorphism is defined by amphibolite facies conditions at > 550°C, ~3.5 kbar (Waters, 1986, 1989) that coincides with the D_2 deformation event due to the preservation of deformed leucosomes within the migmatitic gneisses (Macey et al., 2011). The effects of M_2 were largely obliterated by the later granulite-facies metamorphism.

By contrast, Clifford et al. (2004) and Clifford and Barton (2012) argued that peak M_2 metamorphism (T: ~800–850°C, P: ~5–6 kbar) occurred at ~1.18–1.14 Ga in the Northern Bushmanland Domain due to crustal thickening following the earlier D_2 deformation event at ~1.21–1.18 Ga. This was followed by slow isobaric cooling giving rise to a clockwise P-T-t path. The subsequent ~1.04–1.02 Ga metamorphism is then deemed to have been at lower grade (amphibolite facies: ~580–680°C, ~5.5–6.5 kbar – Clifford and Barton, 2012).

Metamorphic conditions in the Bushmanland Domain are defined by mineral assemblages that include biotite-sillimanite-quartz in the amphibolite facies, cordierite-garnet-K-feldspar-quartz in the lower granulite facies and hercynite-quartz in the upper granulite facies zone (Waters, 1988).

Specific to the Kliprand-Garies area, the Bushmanland Domain has undergone granulite facies metamorphism. Metamorphic studies of supracrustal rocks have shown a symmetrical arrangement of metamorphic zonation about a central domain of upper granulite peak metamorphism (Waters 1986, 1989; Macey et al. 2011; De Beer, 2010) which was confirmed by boundaries between major parageneses in pelitic rocks that includes garnet + cordierite + quartz in the melanosome and garnet + cordierite + K-feldspar + liquid in the leucosome. The following prograde melting reaction:

Biotite + sillimanite + quartz = garnet + cordierite + K-feldspar + H_2O/liquid
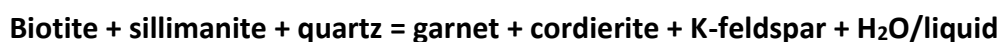
marks the change from upper amphibolite to granulite facies conditions and coincides with the change from amphibolites to two-pyroxene granulites in metabasites of the Oorkraal Suite (Waters, 1986; De Beer, 2010; Macey et al., 2011). At higher metamorphic grades (upper granulite facies) the following reaction confirms the zonation pattern proposed by Waters (1986) in which dark-green hercynite spinel is formed.

Cordierite + magnetite solid solution = spinel solid solution + quartz

Chapter 3: Results

3.1. Field relations and field petrography

3.1.1. Kliprand calc-silicate pod

The studied rock is a banded calc-silicate pod located near the village of Kliprand (S 30°35.939'
E 018°38.815'). It forms part of the Kliprand dome belonging to the Little Namaqualand Suite.
The surrounding rock types include different types of granitic gneisses (seen in Fig. 4 and
observed in this study) such as quartzofeldspathic pink gneiss, pink biotite gneiss, feldspar-
rich pink gneiss, streaky augen gneiss, feldspathic garnet gneiss, biotite hornblende gneiss,
and mafic two-pyroxene granulite. This study is focused on describing the dominant features
of calc-silicate rocks sampled, and the rock types found close to it. No mineral analysis was
obtained. Field photos provided by Woolf (2017).
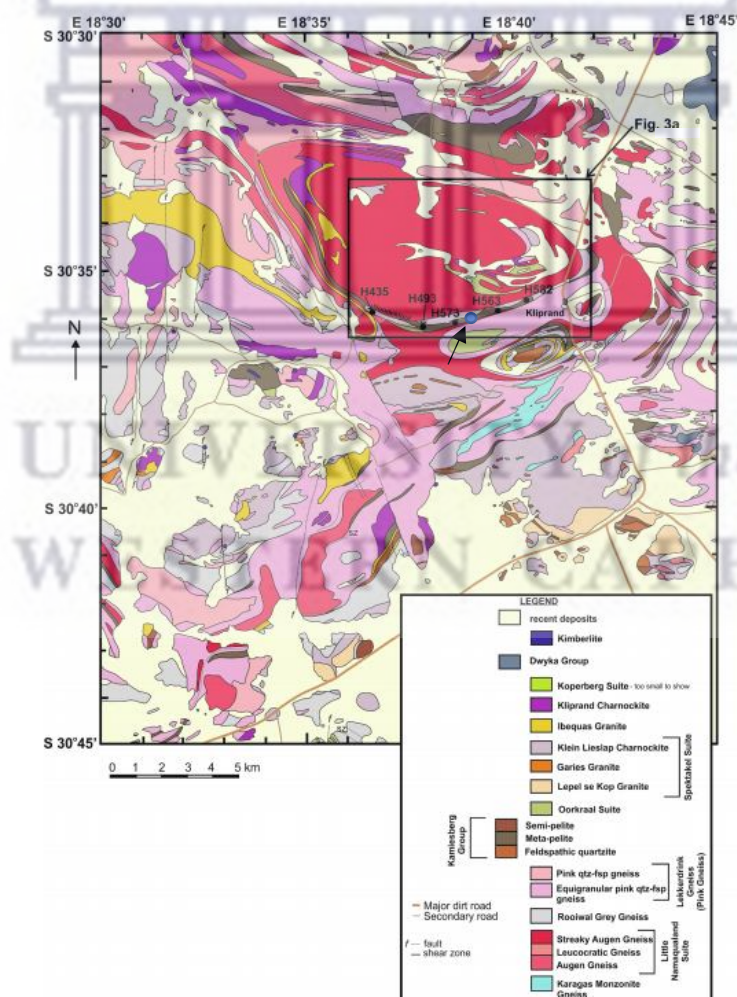
Figure 4: Geological map of the Kliprand area. (Modified after Macey (2001) revision after Albat (1984)). Numbers shown
on the map indicate exploration drillholes from a study by Bailie et al. (2018). The black arrow indicates location of calc-
silicate pod (represented by blue dot on the map between drillholes H573 and H563).
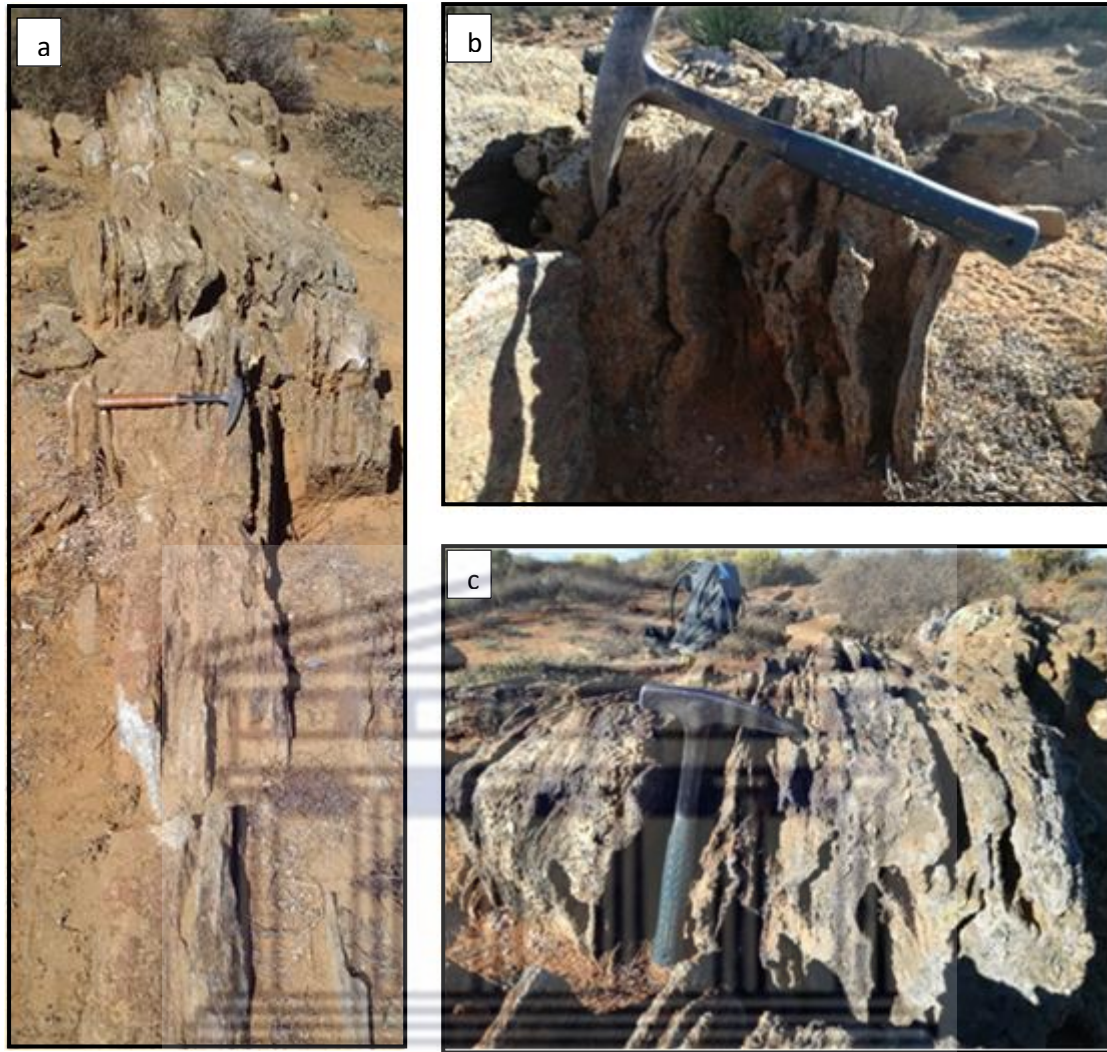
Figure 5: Field photographs of the calc-silicate pod. (a) Extent of the calc-silicate pod (facing East). (b-c) Disharmonic folding within the calc-silicate pod. From Woolf (2017). Length of sharp mouth hammer= 29.5cm.

The calc-silicate pod is of limited extent, about 1m at its greatest thickness and about 8m in length, thinning out at both ends. It occurs as an isolated outcrop adjacent to the quartzofeldspathic pink gneiss of the Lekkerdrink Gneiss, which forms either large flat outcrops or long ridges. The quartzofeldspathic pink gneiss is the dominant rock type in the Kliprand study area and is moderately foliated, with the foliation defined by preferentially aligned quartz rods and feldspar crystals.

17
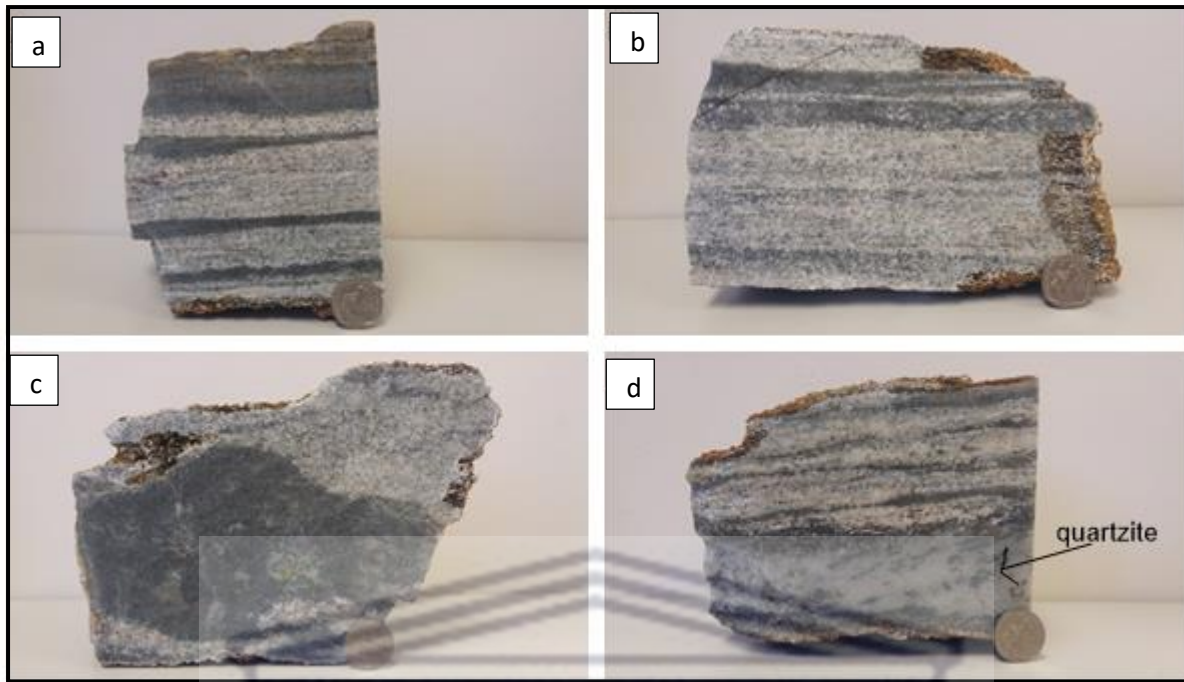
Figure 6: Photographs of calc-silicate samples showing compositional layering (a) Sample 19, (b) Sample 21, (c) Sample 23 – boudin structure of dark layer, (d) Sample 24 – quartzite layer, (Woolf, 2017). Diameter of R2 coin=23mm. Diameter of 10c coin=16.0 mm.

The calc-silicate rocks are characterised by highly weathered surfaces that penetrated the rock on an mm- to cm-scale on the outermost surface, giving the surface an oxidised (brownish) appearance (Fig. 5 a-c). The exterior has a rusty brown colour, masking the appearance of layering and foliation patterns. The rock interior has pronounced banding, which is predominantly compositionally controlled, defined by alternating diopside-and wollastonite-quartz-rich layers on an mm- to cm-scale (Fig. 6 a-b). Some layers display boudinage structures along the horizontal plane (Fig. 6 c), which become discontinuous along strike. Intense disharmonic folding and strong foliation patterns (S_2 planar features), oriented parallel to the internal layering of the rock, are the main structural features shown by the calc-silicate outcrop. The foliation is defined by the alignment of elongate wollastonite and elongated quartz grains. The alignment of minerals is mostly found evident in the wollastonite-quartz- rich layers. Both fine banding and the orientation in which foliation occurs are found parallel to an E-W trend. Large quartzite layers are also present (Fig. 6 d).

18

There is still evidence that the calc-silicate pod was a bedded feature and in its current state is dominated by joints oriented in an N-S direction.

3.1.2 Garies wollastonite quarry and its surroundings

The primary open pit has a restricted spatial extent. Due to ongoing mining operations, the conditions within the pit are in a constant state of change, with existing mine walls regularly subjected to blasting. Consequently, many of the photographs taken and also exact sample locations relate to previous exposures of the quarry walls that are no longer preserved. Every photograph lacking a GPS location, originates exclusively from the quarry.

The Garies deposit is situated in a structurally complex area that has been tightly folded (Fig. 7). The mapped area lies within a valley, with the wollastonite quarry located at the northern end (Fig. 8). Rocks in the area are cut by pegmatite veins (Fig. 9 a-b) which are present in the surrounding rocks of granites, migmatitic metapelitic gneisses, mafic metamorphic rocks and biotite-rich gneisses. Rocks found at the quarry are largely devoid of solid-state fabrics (e.g., foliation), while the surrounding host rock of garnet and biotite gneisses exhibit a distinct foliation (Fig. 9 c) and contain several deformational structures such as boudinage structures, stretched quartz lenses and tightly folded veins (Fig. 9 d-f). The spatial relationship between the quarry exposures and the surrounding rocks is difficult to establish due to the intense refolding of rocks closer to the quarry. The main deposits (consisting of wollastonite-bearing calc-silicate rocks and marble calcite-dominated rocks) are in contact with a feldspar-garnet-hornblende-rich metamorphic rock surrounded by metapelitic gneisses, granites and biotite-rich gneisses further away from the quarry. Granitic rocks are observed further away from the quarry. Other calc-silicate pockets and lenses located further away from the quarry are also surrounded by mafic metamorphic rocks, metapelites, and biotite-rich quartzofeldspathic gneisses. The area is also defined by granitic intrusions (dykes, Fig. 10 a-b).

There are two varieties of biotite-rich quartzofeldspathic gneisses (leucocratic and melanocratic; Fig. 10 a-b). These gneisses are commonly accompanied by garnet-rich melt segregations in the western part of the study area, becoming more frequent closer to the quarry and other calc-silicate pockets observed west of the mapped area (Fig. 10 c-d). Several z and s folds indicate extensive folding (Fig. 10 e-i). Rocks in the eastern and western parts of the mapped area have predominantly the same orientation, dipping towards the SW.

19

Figure 7: Tightly folded calc-silicate rocks. Part of the exposure at the mine site.

Table 3: Description of photographs of exposures outside of the active mining area

Figure	Location	Description
9 a	S 30 28 49.1 E 018 03 40.4	Joints filled with pegmatite veins.
9 b	S 30 28 31.2 E 018 03 35.3	Pegmatite vein.
9 c	S E	Foliation in biotite-rich gneiss.
9 d	S 30 29 12.1 E 018 03 08.4	Stretched coarse-grained quartz lenses.
9 e	-	Boudinage of coarse-grained quartz vein.
9 f	Loose	Tightly folded granitoid vein (veins).
10 a	S 30 28 54.8 E 018 03 25.1	Undulating contact between melanocratic and leucocratic biotite-rich gneiss.
10 b	S 30 28 54.8 E 018 03 25.1	Undulating contact between melanocratic and leucocratic biotite-rich gneiss.
10 c	S 30 27 59.4 E 018 03 10.7	Garnet-rich melt segregation.
10 d	S 30 29 24.1 E018 03 25.5	Migmatitic metapelitic gneiss.
10 e	S 30 27 57.4 E 018 03 08.6	Tight z and s folds with leucosomes.
10 f	S 30 27 57.3 E 018 03 08.5	Tight z and s folds with leucosomes.
10 g	S 30 28 04.5 E 018 03 09.4	Folds in metapilitic gneiss.
10 h	S 30 28 07.9 E 018 03 09.8	Very well defined open and closed isoclinal folds in biotite-rich quartzofeldspathic gneiss
10 i	S 30 28 13.5 E 018 03 08.6	Garnet-rich s folds formed in metapelitic gneiss.
10 j	S 30 28 05.3 E 018 03 09.5	Layer of mafic rock in between biotite-rich quartzofeldspathic gneissic layers.
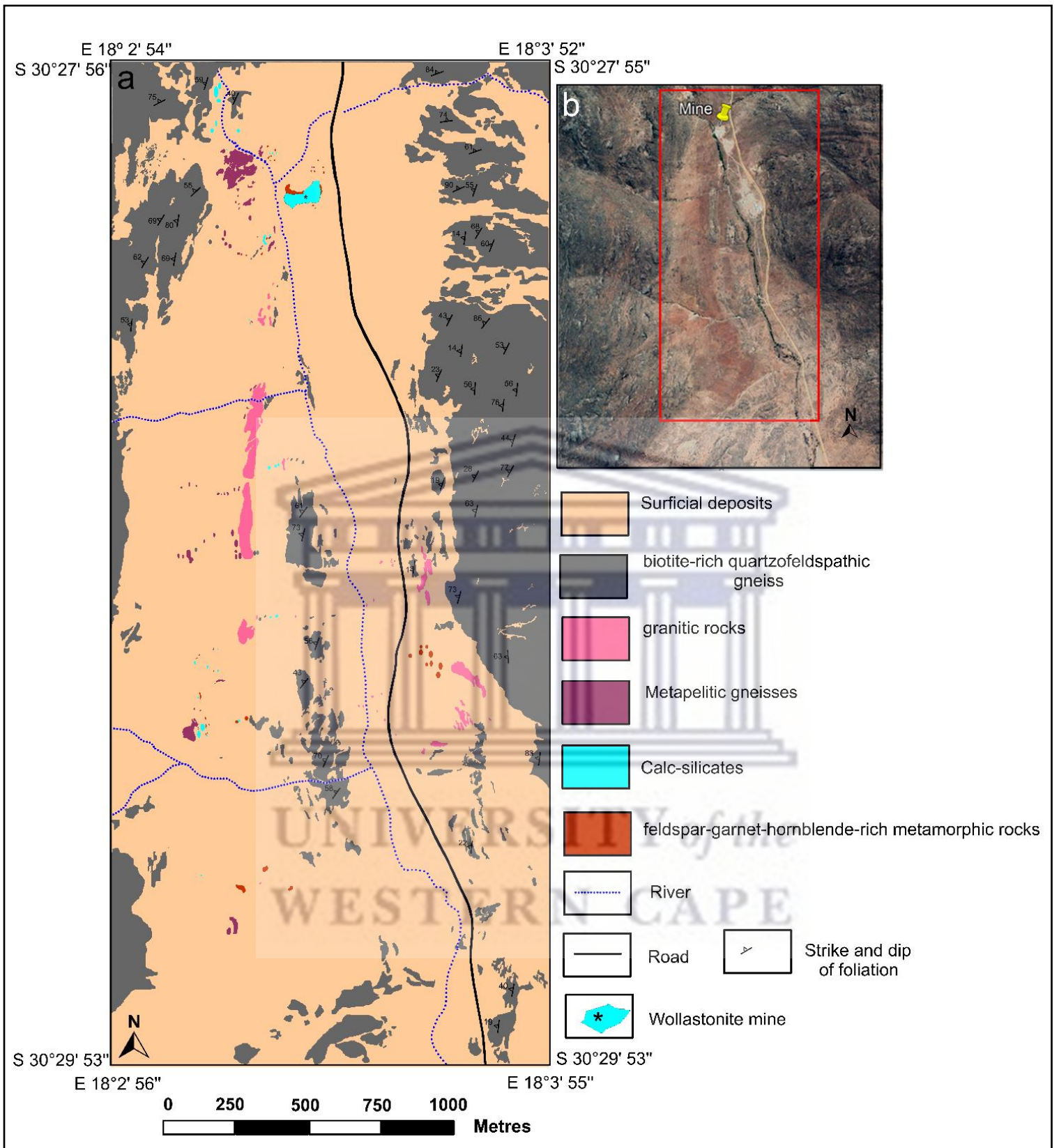
Figure 8: Geological map of the Garies study area. Red square box indicates the mapped area a. (a) Major lithological distributions of the study area. (b) Aerial photograph of study area.
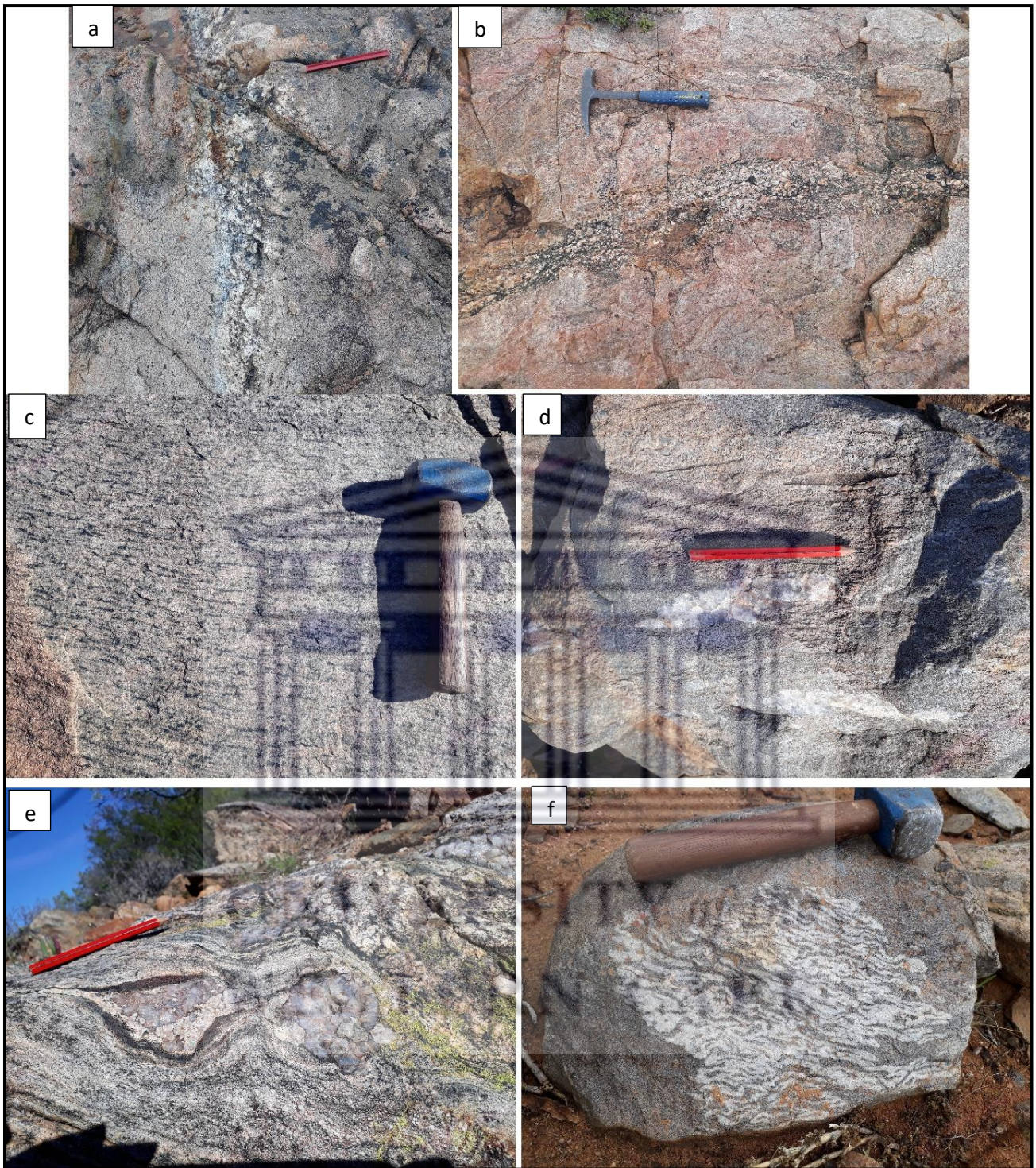
Figure 9: Field photographs of rocks and structures in the Garies study area. (a-b) Pegmatite veins cutting through the surrounding rocks types. (c) Strong foliation present in biotite-rich gneiss. (d) Stretched coarse-grained quartz lenses in the surrounding biotite-rich quartzofeldspathic gneiss (e) Boudinage of coarse-grained quartz vein in the surrounding biotite-rich quartzofeldspathic gneiss. (f) Thin tightly folded granitoid vein (veins) in a feldspar-garnet-hornblende-rich metamorphic rock. Length of sharp mouth hammer= 29.5cm. Length of club hammer= 28cm. Length of pencil= 10cm.
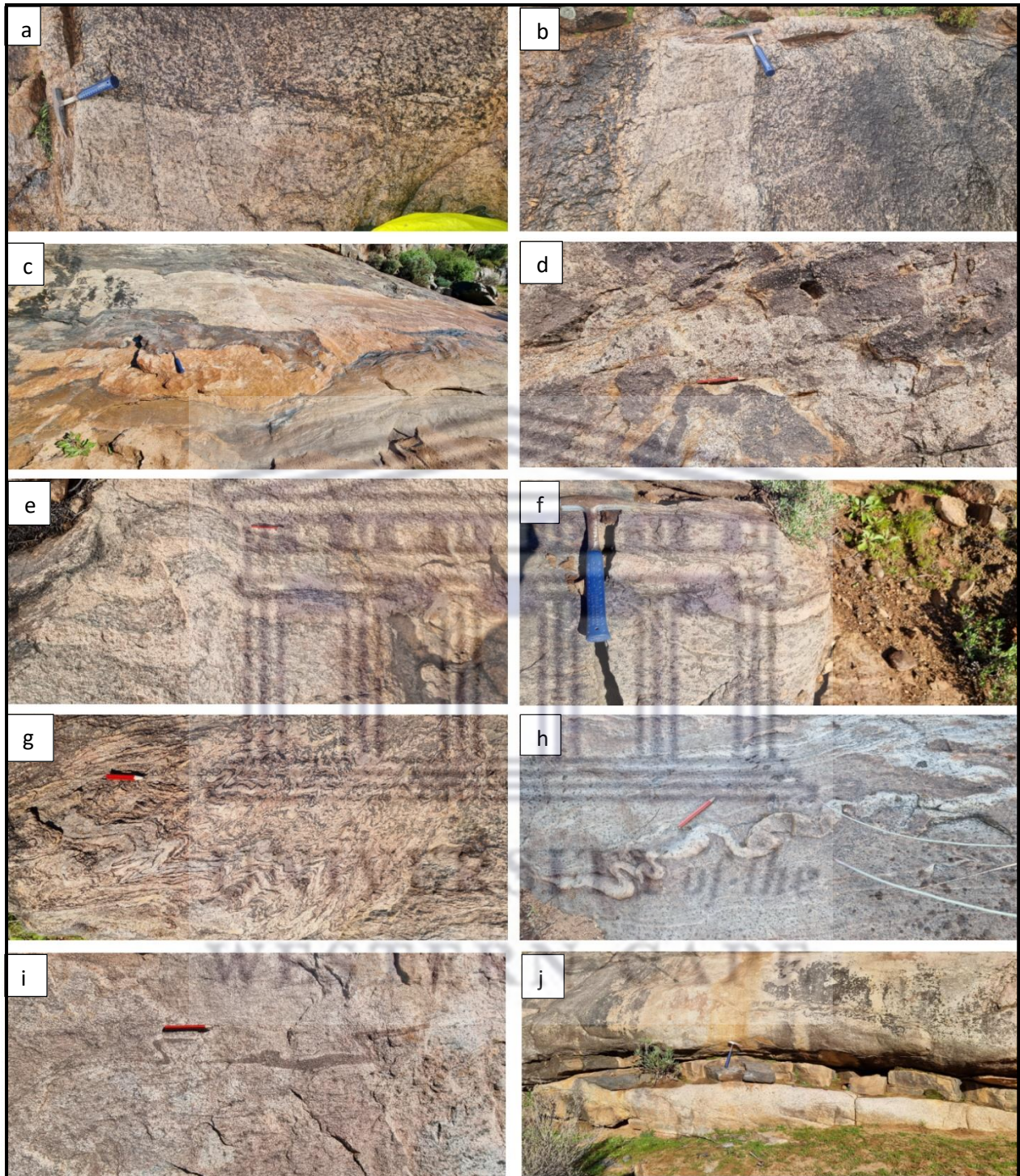
Figure 10: Field photographs of the various rock types and structures in the Garies study area. (a-b) Undulating contact between melanocratic and leucocratic biotite-rich gneiss. Leucocratic material suggests a granitic dyke with an orientation parallel to foliation. The melanocratic variety is also coarser grained than its counterpart. (c) Garnet-rich melt segregation in gneissic rocks. (d) Migmatitic metapelitic gneiss with leucosomes, containing garnet grains. (e-f) Tight z and s folds with leucosomes containing small garnet grains. (g) Folds in metapilitic gneiss. (h) Very well defined open and closed isoclinal folds in biotite-rich quartzofeldspathic gneiss. (i) Garnet-rich s folds formed in metapelitic gneiss. (j) Layer of mafic rock in between biotite-rich quartzofeldspathic gneissic layers. Length of sharp mouth hammer= 29.5cm. Length of pencil= 10cm.

Figure 11: Large fold in the exposed area of the Garies wollastonite quarry. Fold is defined by pyroxene-rich layer. Length of sharp mouth hammer= 29.5cm.

The Garies wollastonite mine exposes a wide range of fresh rocks at the surface with tight folding (Fig. 11). The Ca-rich rocks present within or close to the quarry can be grouped petrologically as follows:

I.   **Wollastonite-calcite-garnet-diopside-vesuvianite rocks**
II.   **Pure Wollastonite**
III.   **Marble (Calcite-dominated)**
IV.   **Garnet-diopside-vesuvianite rocks**

Wollastonite-calcite-diopside-garnet-vesuvianite-rich rocks (Fig. 12 a-b) are observed throughout the quarry and are the most dominant rock type, containing the highest number of coarse-grained assemblages in the quarry. The mineral assemblages include wollastonite, calcite, diopside, garnet, vesuvianite with rare quartz and titanite. They are medium- to coarsely- crystalline and predominantly greyish-white in colour as a result of the abundant carbonate and wollastonite minerals comprising the rocks. Characteristic reddish-brown and dark green spots on the rocks are garnet and diopside, respectively. These rocks may exhibit a more prominent banding defined by alternating garnet- and wollastonite-carbonate-rich layers. Field evidence also suggests the development of garnet-diopside/garnet-vesuvianite-rich patches along with veins of wollastonite and calcite forming parallel to the banding of the host calc-silicate rocks.

24
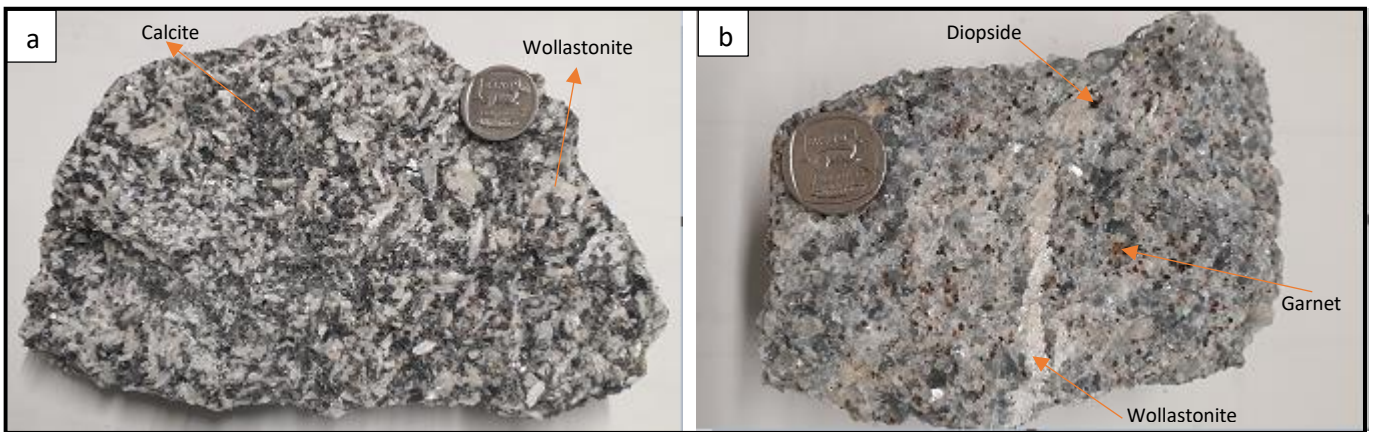
Figure 12: (a-b) Calc-silicate samples (Na219) containing the coarsest grain assemblages in the Garies wollastonite quarry. Notice that garnet and diopside in sample b are more readily distinguishable. Diameter of R1 coin=20.0 mm.

Pure wollastonite often appears milky white to transparent in colour. It is comprised of numerous elongated, intergrown wollastonite crystals and are the coarsest grained mineral in the quarry. The growth of such pure wollastonite crystals is commonly observed to have developed as large clusters, discontinuous patches or veins (Fig. 13) within the outcrop. The clusters of wollastonite range between 1- 1.5 m in diameter. The diopside inclusions, due to their green colour, change the appearance of wollastonite from its original milky white/ transparent colour to a slightly lighter green shade. Wollastonite veins are typically associated with garnet-rich zones (Fig. 13 a-b). Some of the large wollastonite crystals are poikilitic with inclusions of fine-grained diopside and garnet crystals (Fig. 13c).

Apart from wollastonite, calcite-dominated marble (Fig. 13 d-e), commonly developed either as clusters or veins within the main calc-silicate assemblages, are also present. The marbles are dark grey, coarsely crystalline and are comprised of numerous calcite grains each expressing a perfect rhombohedral cleavage (Fig. 13 d). Calcite veins are commonly observed with garnet-rich reaction seams around them (Fig. 13 e).

25
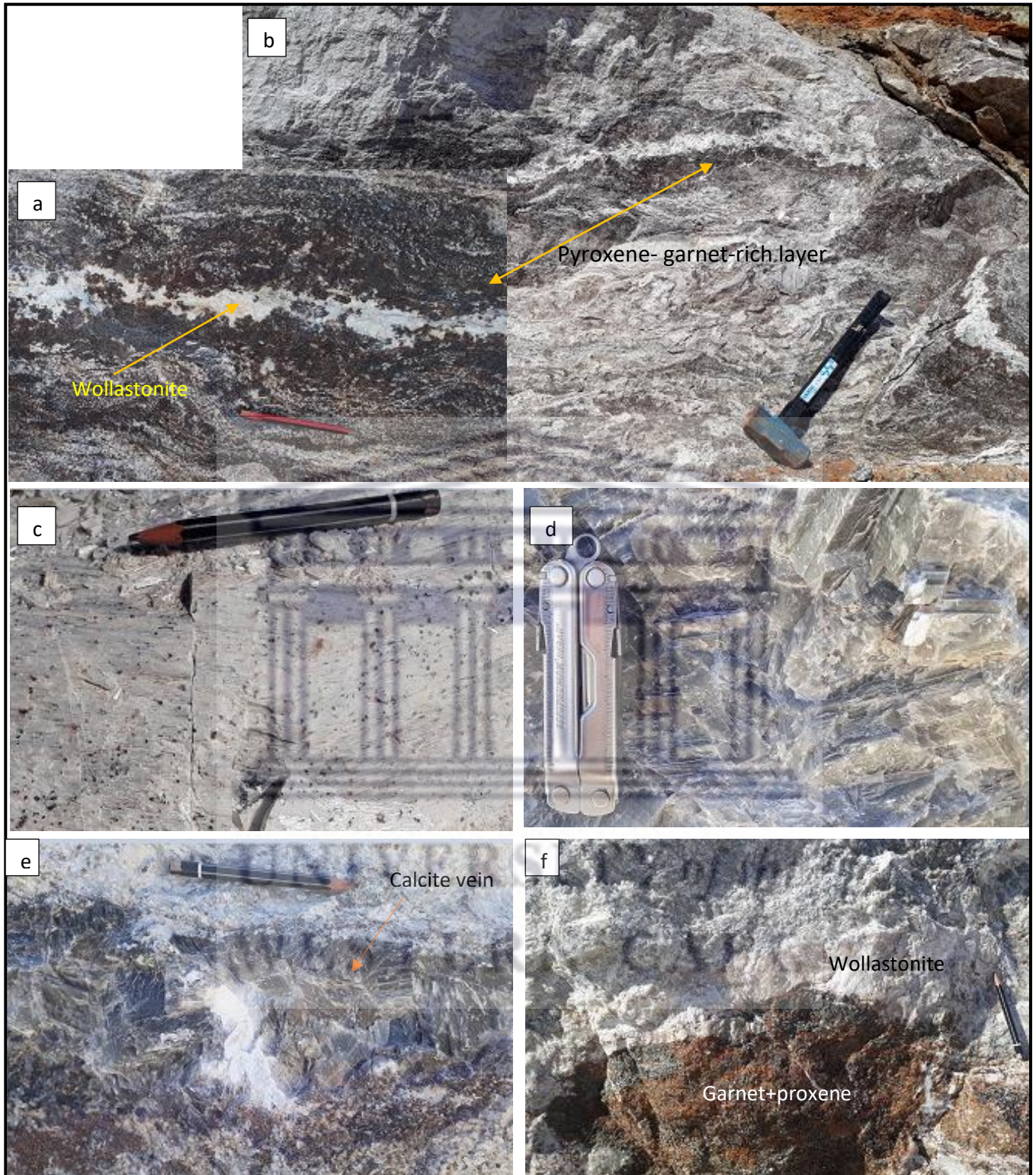
Figure 13: Field photographs from the Garies wollastonite quarry. (a-b) Wollastonite vein with adjacent garnet-diopside rich zones. (c) Pure wollastonite clusters enclosing diopside and garnet grains. (d) Very coarse-grained calcite-dominated marble (e) Calcite vein zoned by a garnet-rich reaction formed in calc-silicate deposit. (f) Garnet-diopside patches enclosed in massive wollastonite. Length of sharp mouth hammer= 29.5cm. Length of club hammer= 28cm. Length of red pencil= 10cm. Length of black pencil= 5cm. Leatherman wave= 10cm.

26

Garnet-diopside-vesuvianite-rich rocks are observed as random discontinuous patches (Fig. 13 f). They are developed within wollastonite-rich clusters or more commonly as patches or layers surrounded by thin wollastonite-rich veins in the carbonate-rich calc-silicate assemblages. The relative proportions of Ca-silicates differ from one patch to another (Fig. 14 a-b) and include pairings of garnet-diopside, garnet-vesuvianite, diopside-vesuvianite and garnet-diopside-vesuvianite. When these types of rocks form layers, they commonly alternate with wollastonite-carbonate-rich layers (Fig. 14 c-d). They are extremely brittle, fine to coarsely crystalline and either have a predominantly dark reddish-brown or dark green appearance depending on which mineral is more abundant (i.e., garnet or diopside). These types of assemblages may or may not contain wollastonite, while microcline, quartz, sphene and prehnite are also seen as part of the calc-silicate assemblages.
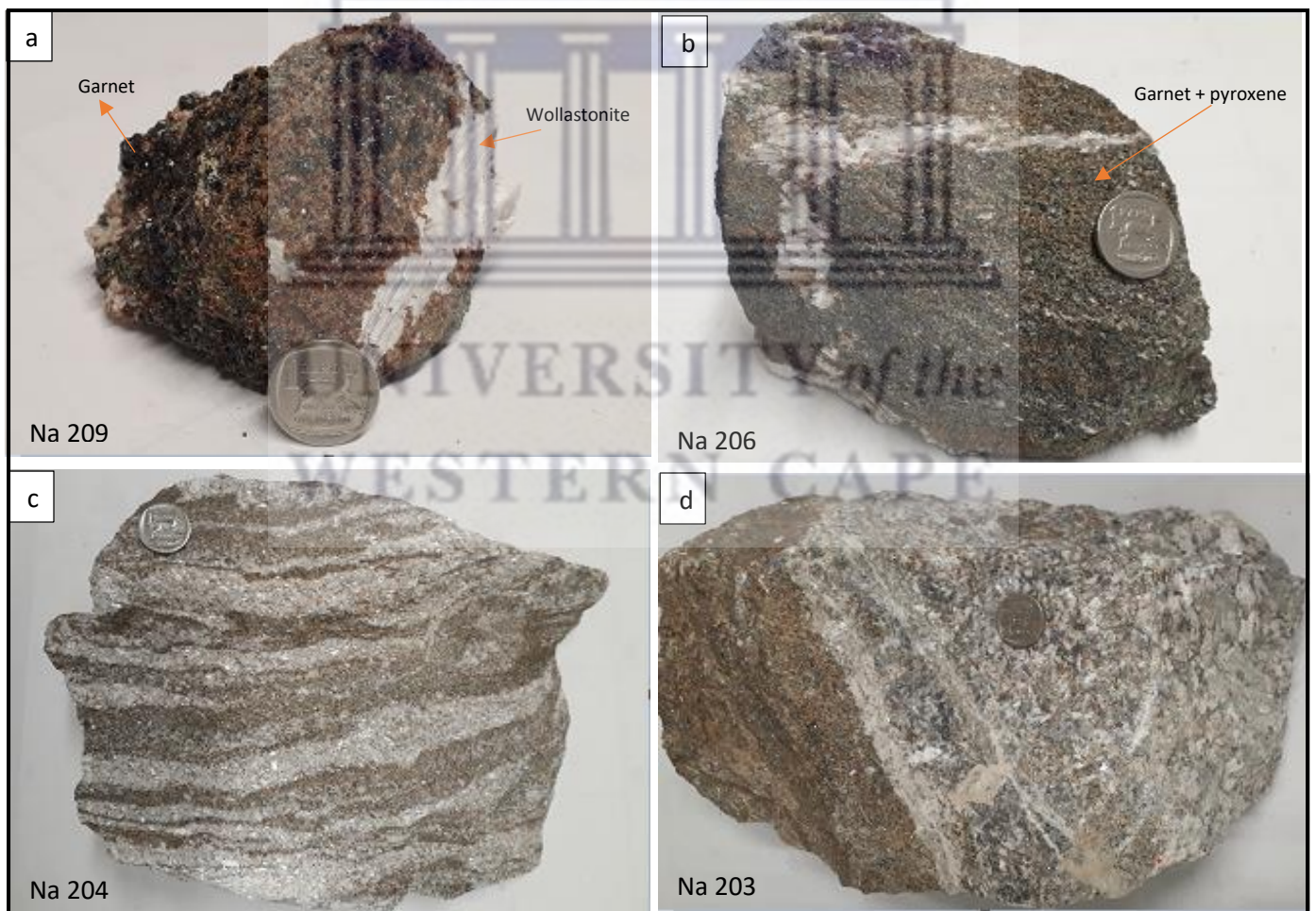
Figure 14: Calc-silicate samples from the Garies wollastonite quarry. (a) Garnet- rich samples (b) Diopside-rich samples (c) Alternating garnet- and wollastonite-rich layers (d) Banded calc-silicate sample. Sample numbers provided in the bottom left corner. Diameter of R1 coin is 20.0

Textural features such as compositional banding are defined by banded structures of garnet-diopside assemblages alternating with bands of calcite-wollastonite-rich assemblages (Fig. 14 c-d). Most of these banded structures are only observed in garnet-rich rocks apart from a few calc-silicate samples which have banding defined by wollastonite-rich assemblages. In these types of calc-silicate rocks, wollastonite grains display an unusual orientation that is partially perpendicular to the direction of banding. Structural features such as foliations are absent from the studied samples, whereas other structural features such as garnet-diopside-rich boudins (Fig. 15 a), are present and surrounded by bands of alternating garnet and calcite-rich layers. Folding (Fig. 15 b-c) are quite common structural features observed in rock samples throughout the quarry.
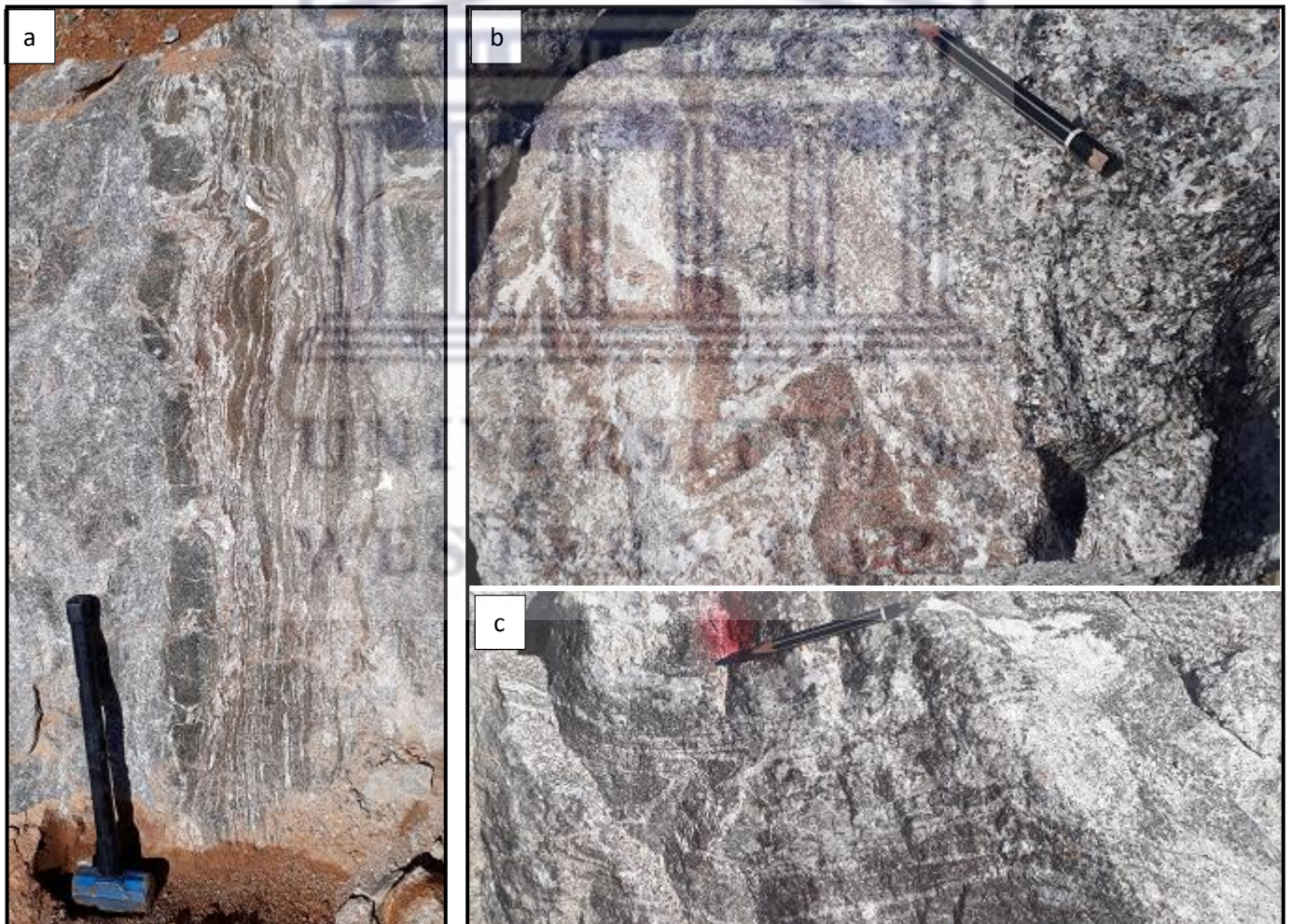
Figure 15: Deformational structures in the Garies wollastonite quarry. (a) Boudinage structures defined by garnet-diopside rich zones. (b) Tightly folded garnet-rich layers. (c) Thin folded layers. Length of pencil= 5cm.

3.2. Thin section petrography

3.2.1. Microscopic study of the Kliprand calc-silicate pod

Twenty thin sections were cut from the calc-silicate pod as a roughly continuous profile for further analysis.

All of the analysed sections exhibit the same mineralogical composition, with variable amounts of scapolite, diopside (clinopyroxene), wollastonite, quartz, accessory titanite and opaques. Calcite, K-feldspar and plagioclase also occur in minor proportions (Fig. 16 a). Garnet is absent in all the samples. Calcite occurs as medium- to fine-grained prismatic or tabular grains (Fig. 16 b). It is, however, in disequilibrium with the surrounding minerals either replacing wollastonite (in association with quartz) or replacing scapolite (in association with plagioclase). Plagioclase occurs either as very fine-grained crystals replacing scapolite or as medium-fine grained subhedral- to anhedral- crystals, with some being partially or completely altered to sericite. Medium- to fine-grained subhedral diopside and scapolite grains are predominantly found close to each other forming diopside-scapolite granoblastic layers. Scapolite has two main end members in the solid solution series, sodic marialite and, calcic meionite. The birefringence of scapolite is sensitive to its composition. Interference colours between the two end-members range from low first-order yellow for sodic scapolite to upper second-order blue for the calcic-rich varieties. Scapolite is commonly replaced by fine-grained plagioclase, calcite, and locally, minor quartz. The replacement of scapolite by quartz is evident from symplectic and embayed reaction textures (Fig. 16 c).

Wollastonite occurs as elongate, medium- to coarse-grained blades or laths, some of which are up to 4.5-5mm in length and exhibiting symmetrical twinning. Wollastonite is commonly observed to be partially replaced by calcite and quartz (Fig. 16 d), mostly along its cleavage planes and shows a clear preferred orientation parallel to gneissic banding. Quartz either appears as large 3-4mm elongate grains (Fig. 16 e) or fine-grained anhedral grains and occasionally, when forming part of retrograde reactions, quartz also appears as fine-grained needle-like remnants (Fig. 16 f). Quartz typically exhibits undulose extinction in most of the analysed sections.
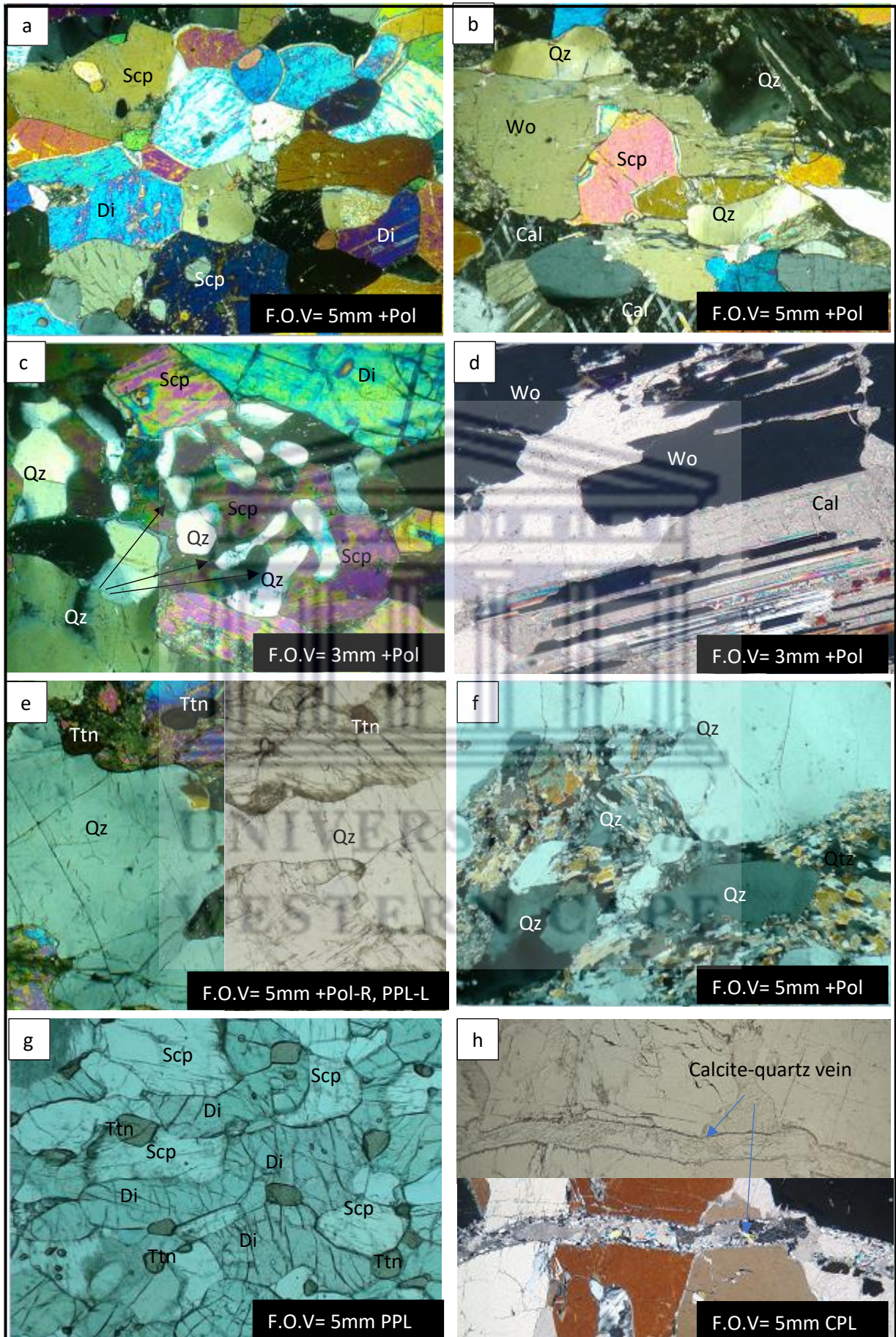
Figure 16: Microphotographs of minerals from the Kliprand calc-silicate pod. (a) Scapolite and diopside grains in calc-silicate pod (b) Quartz, calcite and wollastonite in calc-silicate gneiss with quartz and calcite being retrograde products from the breakdown of wollastonite (c) Scapolite-quartz symplectites (d) Calcite and quartz replacing wollastonite grains along its cleavage planes (e) Elongated quartz grains along with small brown titanite grains in the calc silicate gneiss. (f) Breakdown of scapolite. (g) Titanite crystals along with diopside and scapolite. (h) Evidence of E-W extension void in the rock filled with remnants of calcite and quartz. Field of view (F.O.V), Crossed polarizers (+Pol), Plane polarised light (PPL). R-right, L-left.

Titanite is occasionally present as small inclusions in pyroxene and scapolite but it is more commonly observed as isolated, fine-grained, subhedral brown crystals (Fig. 16 g). Opaque crystals, where present, are commonly in contact with calcite-quartz rims.

Other textural features of the calc-silicate pod include granoblastic and foliated deformation textures. This is correlated with gneissic bands defined by the layering observed within most of the sections. Granoblastic layers alternate between each other with only a difference in the grain size distinguishing each layer. Banding ranges between 1-3mm in width across the sections while some sections display no banding at all.

Granoblastic textures are mostly defined by randomly oriented subhedral to anhedral scapolite, diopside and quartz grains. Lineations are mostly defined by large elongated and stretched quartz along with bladed wollastonite grains. The alternation between foliated and granoblastic layers is not always distinctive, as elongated quartz or wollastonite grains defining this texture are not always present. In one of the analysed sections, banding is defined by a thin titanite- scapolite- diopside-rich layer (Fig. 16 g).

Sericitization is the only alteration texture observed within most layers. It is commonly shown by scapolite and plagioclase, which range from being partially to completely sericitized in most samples. The alteration of plagioclase resulted in the formation of partially formed fine-grained fibrous white mica as a product of sericitization. Numerous deformations (undulose extinction displayed by quartz), replacement and reaction textures (sericitization) are observed within some of the analysed samples. These metamorphic features tend to be more prominent in some sections compared to the rest of the samples or just in certain layers of the same analysed sample.

Evidence that the rock was stretched and fractured is observed in a few sections (Fig. 16 h). The void between the minerals is filled by a continuous quartz-calcite assemblage.

3.2.2. Microscopic study of the samples from the Garies wollastonite quarry

fifty thin sections were cut and prepared for microscopic analysis. A summary of the mineralogical composition and description of each section is provided in Table 3.

The analysed sections are divided into five rock groups **(CS1, CS2, CS3, CS4, M1)** based on their differing mineralogical components. Five metamorphic assemblages were identified. In

this thesis, abbreviations from Whitney and Evans (2010) are used. Metamorphic assemblages include:

i.   **Cal + Wo + Di + Grt +Ves ± Ttn ± Ep** (CS1) (calcite-rich)

ii. **Grt + Di + Ves + Wo ± Fld ± Cal** (CS2) (Garnet-diopside-rich)

iii. **Grt + Di + Ves ± Wo ± Cal ± Mc** (CS3) (Garnet-diopside-vesuvianite-rich)

iv. **Grt + Ves ± Di ± Prh** (CS4) (Garnet-vesuvianite-rich)

v.   **Mc + Grt + Hbl+ Di ± Ttn** (M1) (Microcline-garnet-hornblende-diopside-rich)

<u>CS1 group</u>

The main minerals consistently present in the CS1 group include calcite, wollastonite, diopside, garnet and vesuvianite. Associated minerals include rare titanite, epidote and recrystallised quartz. These samples are very calcite-rich and can be referred to as calc-silicate marbles. In thin section, calcite is the most abundant mineral. It occurs as colourless, coarse-grained, anhedral grains with a large variation in their twin geometry. Calcite crystals ranges from thick to thin and straight to curved (Fig. 17 a-b), typically showing internal deformation. Calcite exhibits a very high relief that changes with rotation, with some grains displaying their characteristic lamellar twinning. Moreover, some calcite grains contain a large number of inclusions consisting of garnet, wollastonite, vesuvianite and diopside.
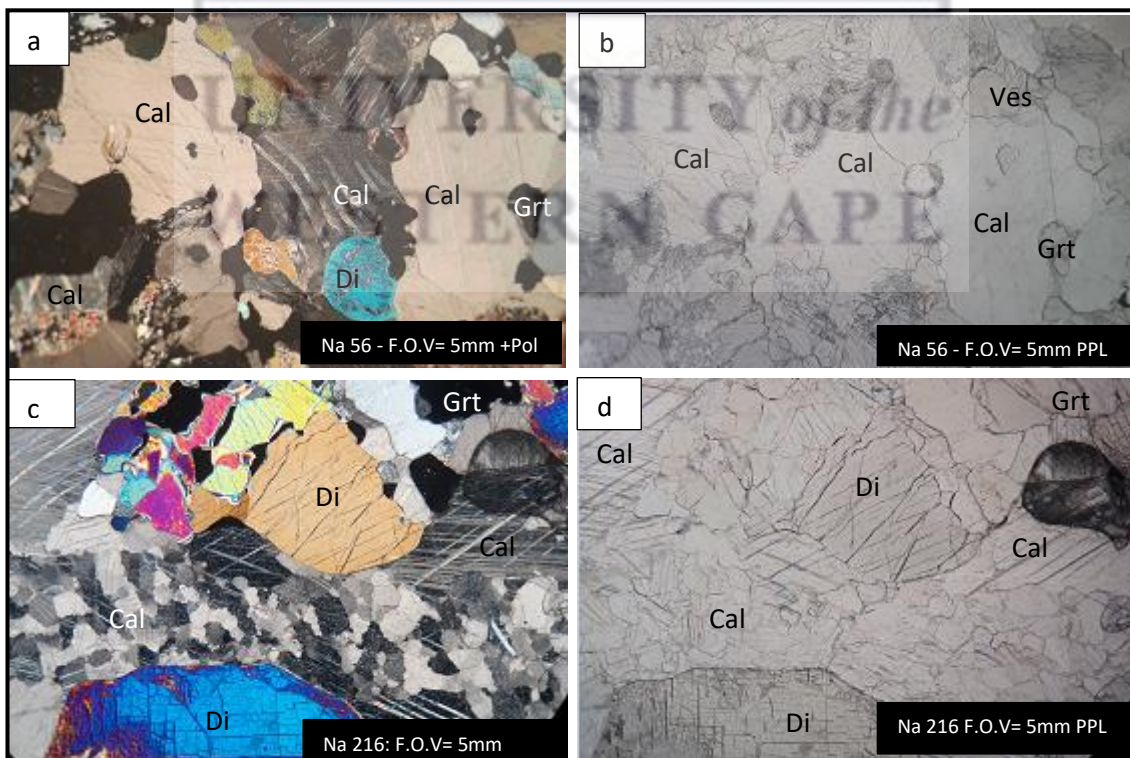
Figure 17: Microphotographs of minerals present in the CS1 rock group from the Garies rock samples. (a-b) Deformed calcite grain. (c-d) Recrystalised calcite grains across thin section. Field of view (F.O.V), Crossed polarizers (+Pol), Plane polarised light (PPL).

32

Although rare, some calcite grains are distinctly finer-grained than the bulk of the calcite and appear recrystallized (Fig. 17 c-d). Occasionally, calcite forms reaction rims around garnet (Fig. 18 a-d). This type of reaction texture is only observed in the CS1 samples.
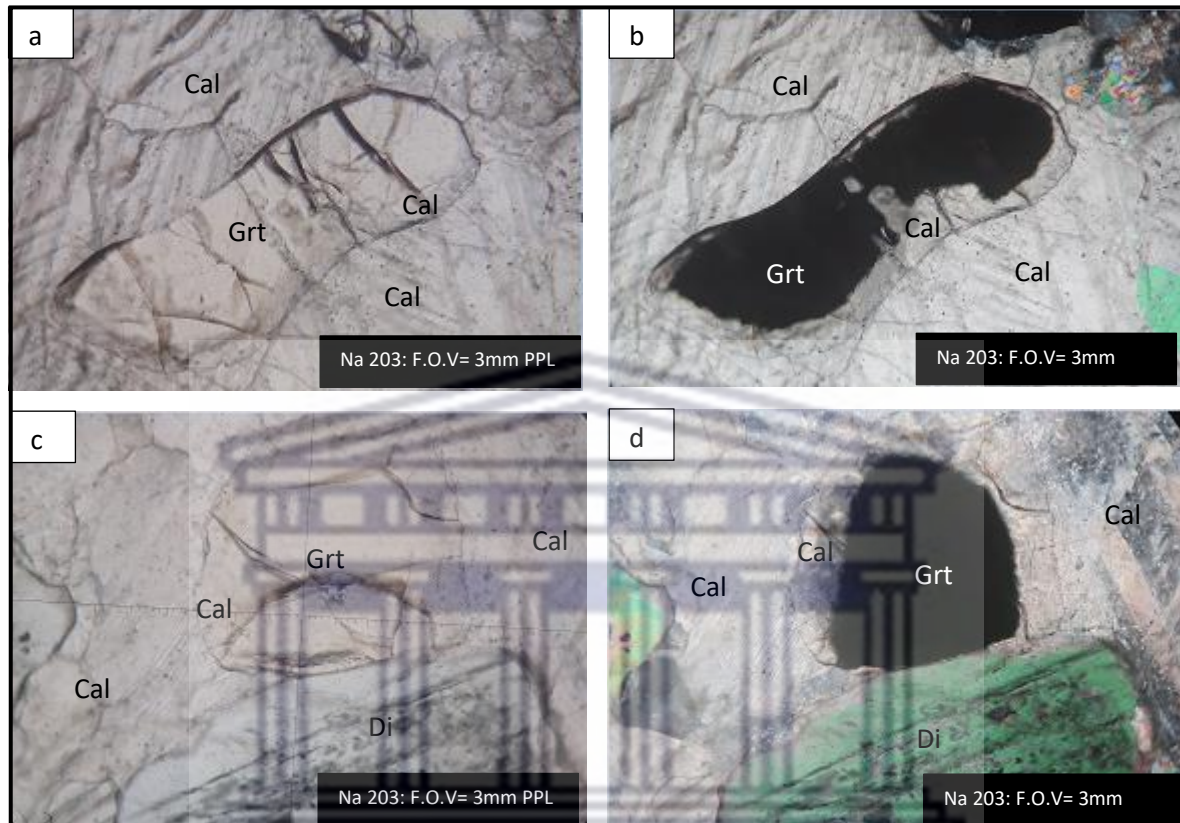
Figure 18: (a-d) Microphotographs of calcite reaction rims around garnet grains replacing garnet at the mineral grain boundary. Field of view (F.O.V), Crossed polarizers (+Pol), Plane polarised light (PPL).

Wollastonite occurs as colourless, elongated blades or laths and is predominantly medium- to coarsely-grained with some grains exhibiting simple twinning. They enclose numerous anhedral aggregates of calcite, quartz, diopside, garnet and vesuvianite (Fig. 19 a) and tend to have moderate to high relief. Very small anhedral recrystallised quartz grains are observed along the cleavage planes and grain boundaries of wollastonite in association with calcite, typically replacing wollastonite (Fig. 19 b-c). Very fine-grained exsolution lamellae of diopside that grew parallel and perpendicular across the length of wollastonite grains are observed (Fig. 19 d-e-f). Epidote and apophyllite grains are also found replacing wollastonite, parallel to its cleavage planes (Fig. 19 g-h).
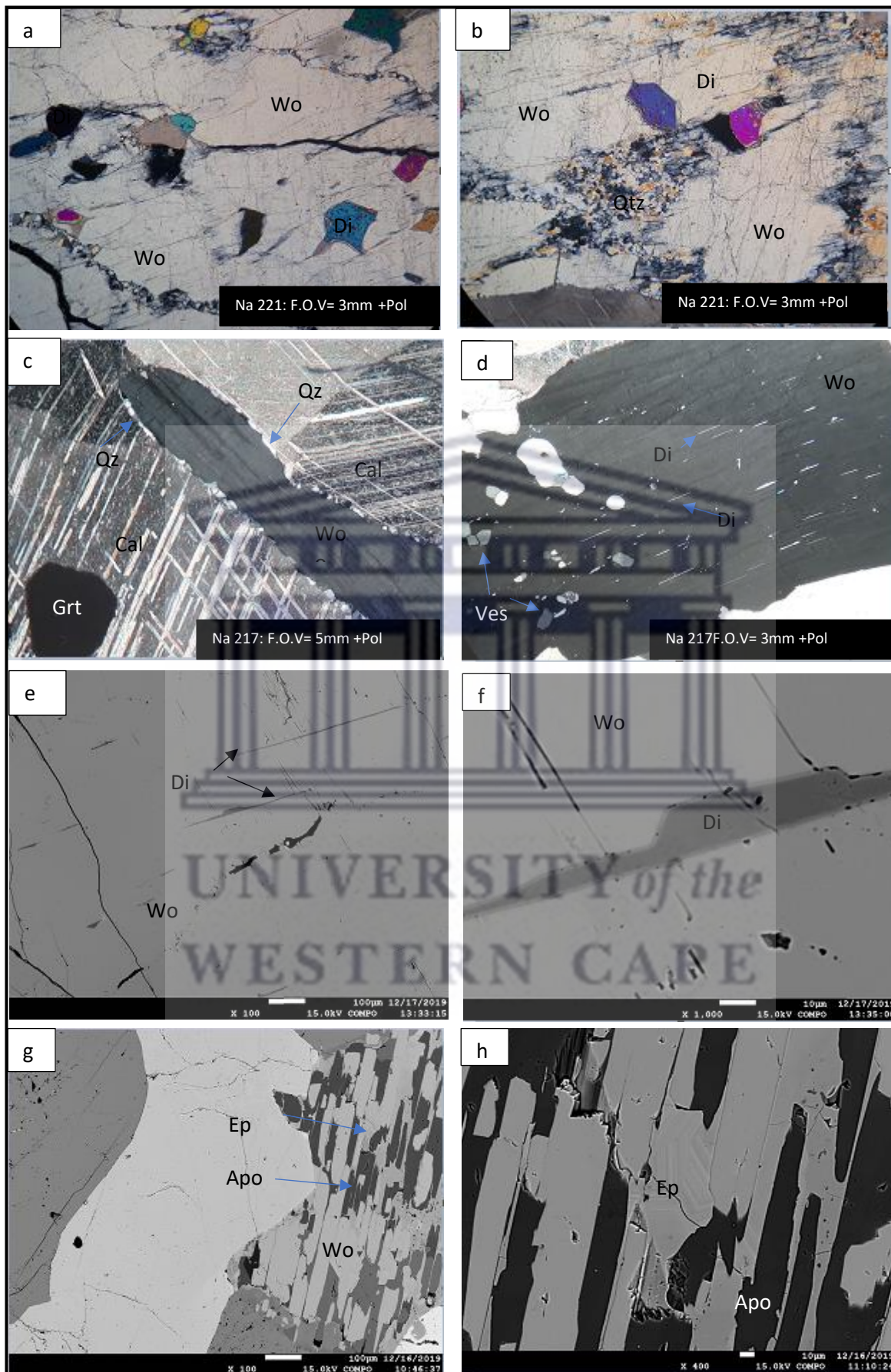
Figure 19: Microphotographs of wollastonite. (a) Coarse-grained wollastonite with numerous inclusions of diopside, garnet and vesuvianite. (b) Recrystallised quartz forming in the cleavage planes of wollastonite. (c) Quartz forming at the grain boundary of wollastonite. (d) Exsolution lamellae of diopside forming in the cleavage planes of wollastonite. Also notice some vesuvianite inclusions. (e-f) BSE images of diopside lamellae forming across the length of wollastonite. (g-h) BSE images of apophyllite and epidote forming in the cleavage planes of wollastonite. Field of view (F.O.V), Crossed polarizers (+Pol), Plane polarised light (PPL).

Table 4: Summary of mineralogical composition and textures of studied calc-silicates

Group	CS1	CS2	CS3	CS4	M1
Sample number	Na203c, Na213, Na218, Na221c, Na109, Na217, Na221a, Na216a, Na263, Na215, Na56b, Na56b, Na221b, Na203b, Na221	Na216, Na216c, Na204a, Na204b, Na206, Na214, Na210a,	Na216, Na203a, Na209, Na210b, Na200	Na203a, Na203b, Na207, Na208	Na223, Na224, Na212
Mineralogical composition	Cal / Grt / Di / Wo / Ves / Qz / Ep	Grt / Di / Ves / Wo / Mc / Cal	Grt / Di / Ves / Wo / Cal	Grt / Ves / Qz / Di / Prh	Mc / Grt / Di / Ttn / Qz
Description	Calcite-rich. Predominantly medium-coarsely crystalline. Calcite crystal exhibit internal deformation.	Garnet diopside-rich. Predominantly fine-medium-grained. Garnet display poikiloblastic and spongy texture. Display Banded deformational features.	Garnet-vesuvianite-rich.	Garnet-vesuvianite-quartz-rich. Interlocking texture. Carbonate alteration products visible.	Microcline-garnet-diopside-rich. Sericitization of microcline. Interlocking texture between garnet and diopside.
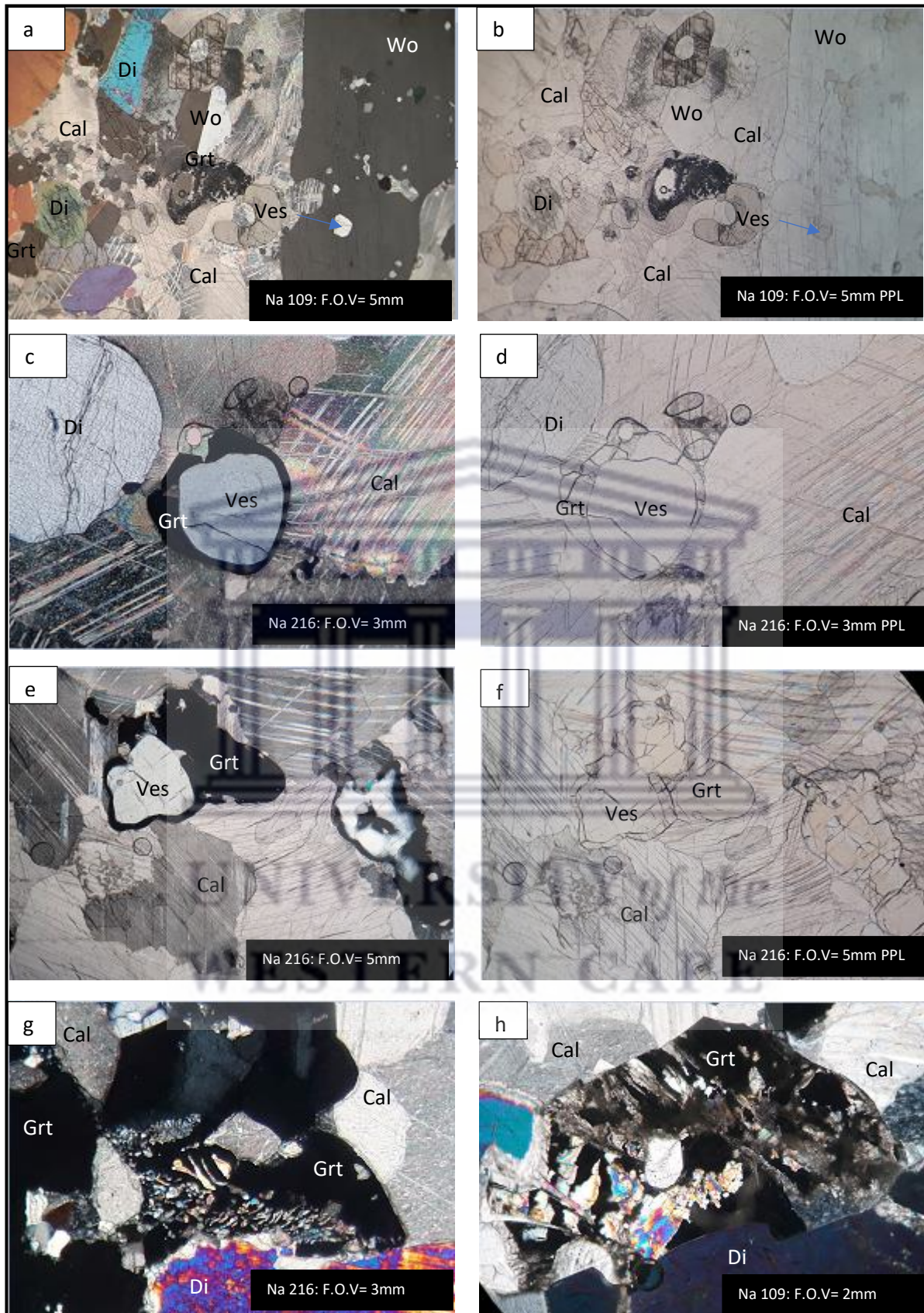
Figure 20: Microphotographs of minerals and textures observed in the CS1 rock group (a-b) Calcite-rich sample with garnet, vesuvianite, diopside and wollastonite. Notice inclusions of garnet and vesuvianite in wollastonite grains. (c-f) Coronal garnet around vesuvianite. (g-h) Symplectic diopside grains within garnet porphyroblast. Field of view (F.O.V), Crossed polarizers (+Pol), Plane polarised light (PPL).

In the CS1 group (Fig. 20 a-b) garnet mainly occur as pale brown to nearly colourless granoblasts. Mostly they appear anhedral, fine- to medium-grained grains with a very high relief commonly displaying evidence of fracturing. Garnet is also preserved as relict inclusions in calcite and wollastonite. Garnet commonly forms a reaction rim around vesuvianite (Fig. 20 c-f). Garnet is also observed being partially replaced by intergrowths of diopside and occasionally, calcite (Fig. 20 g-h).

Vesuvianite mainly occurs as colourless to pale brown, anhedral grains (Fig. 20 a-b), mostly observed in close proximity to garnet. Vesuvianite has a very high relief and displays evidence of fracturing. Under crossed polarizers vesuvianite can be distinguished from garnet as it is birefringent. In crossed polarisers (CPL) vesuvianite appears light grey and anisotropic while garnet is black and isotropic. Modal amounts of vesuvianite and garnet are typically similar, both making up approximately 5% of the rock volume in the CS1 group.

Diopside grains (Fig. 21 a-d) occur either as inclusions in wollastonite, garnet and calcite or as isolated grains randomly dispersed in the CS1 group. They are typically colourless to pale green, anhedral and ranging from fine- to medium-grained with a moderate to high relief. Some diopside grains are observed exhibiting their characteristic cleavage planes in two directions, intersecting at a 90° angle. Simple twinning is observed in some diopside grains.
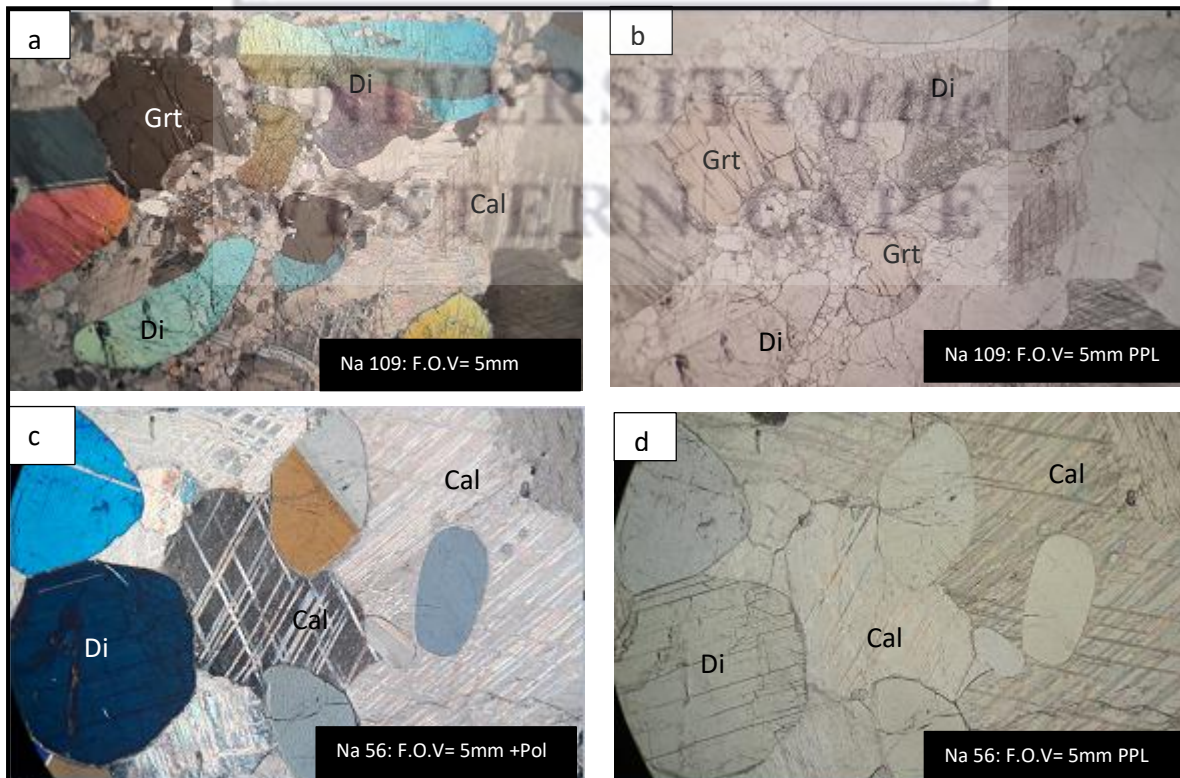
Figure 21: (a-d) Microphotographs of diopside within CS1 rock group from the Garies quarry. Notice distinctive cleavage and simple twinning diopside displays. Field of view (F.O.V), Crossed polarizers (+Pol), Plane polarised light (PPL).

37

Accessory titanite is randomly dispersed, typically occurring as isolated pale brown, slightly elongated diamond-shaped grains.

CS2 group

The main minerals consistently present in the CS2 group include garnet and diopside (Fig. 22 a-b) with associated vesuvianite, wollastonite, titanite, and locally plagioclase and calcite as accessory phases. Evidence does not suggest any significant variation in the mineral assemblage compared to the CS1 group although differences in the modal abundances of garnet and diopside are observed.

The CS2 group is banded and predominantly fine- to medium-grained while reaction textures are rarely observed. Some coarse-grained bladed wollastonite grains exhibit partial replacement by fine-grained quartz and calcite grains. Banding is not easily recognised but can be distinguished based on each layer's mineral assemblage. Banding is characterised by garnet-diopside rich layers, alternating with layers comprised of calcite, garnet, wollastonite, diopside and occasionally, vesuvianite. Garnet-diopside-rich layers are predominantly associated with accessory wollastonite, calcite, microcline and, vesuvianite.

Garnet is observed as anhedral, pale brown, fine- to medium-grained with very high relief. Garnet also occurs as inclusions in diopside. In section Na 204a and Na 204b, a garnet encloses numerous inclusions of diopside, wollastonite, elongated (deformed) titanite, calcite and rare feldspar crystals, typically exhibiting a spongy garnet texture (Fig. 22 c-d). Diopside occurs as colourless to pale green, fine- to medium-grained crystals with high relief. Most diopside grains contain a large number of fine-grained, anhedral garnet inclusions. Simple twinning is also common. Microcline crystals are colourless with a very low relief occurring as fine-grained, anhedral to subhedral crystals. In cross polarizers, they display their characteristic cross-hatch twinning. Titanite is mostly observed as isolated dark brown elongated diamond-shaped grains.

CS3 group

The main minerals consistently present in the CS3 group include garnet, vesuvianite, diopside with accessory microcline, wollastonite and calcite (Fig. 22 e-f).
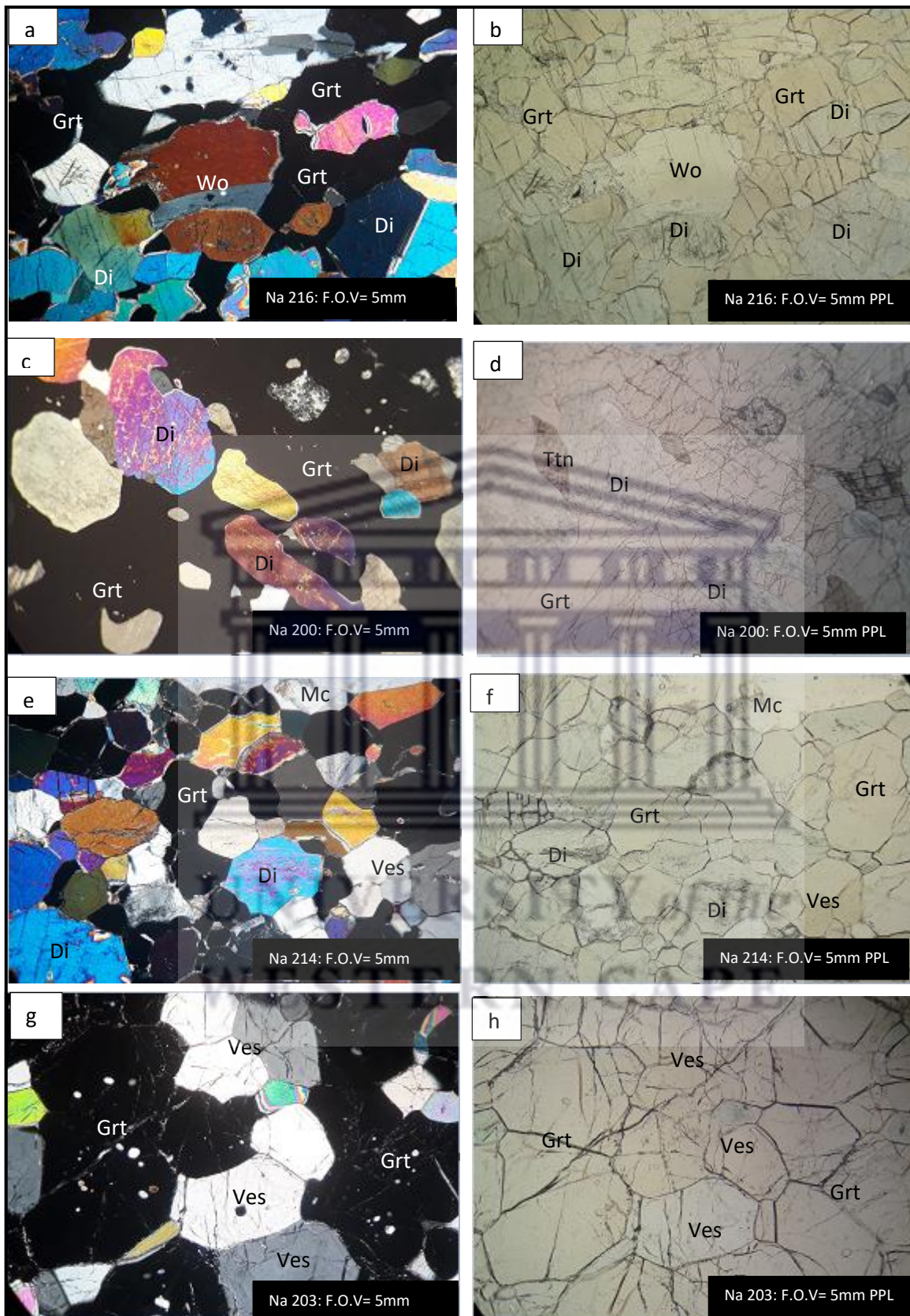
Figure 22: Microphotographs of garnet-rich samples from the CS2 and CS3 rock group. (a-b) Garnet- diopside-rich assemblages present in the CS2 rock group. (c-d) Garnet containing numerous inclusions of diopside, titanite, wollastonite forming a spongy garnet texture. (e-f) Mineral assemblages present in the CS3 group. (g-h) Garnet-vesuvianite-rich assemblages present in the Cs4 group. Field of view (F.O.V), Crossed polarizers (+Pol), Plane polarised light (PPL).

39

Garnet and vesuvianite are similar in size and shape, colour and relief. Both garnet and vesuvianite occur pale brown to nearly colourless, subhedral to euhedral, fine- to medium-grained with a very high relief. Diopside appears as pale green, fine- to medium-grained anhedral crystals.

CS4 group

Mineral assemblages in the CS4 group are characterised by the presence of predominantly subhedral-euhedral garnet and vesuvianite grains (Fig. 22 g-h). CS4 rock samples are further subdivided into CS4a- and CS4b groups.

The main discerning feature of the CS4a group is the large quartz percentage and absence of wollastonite while the amount of vesuvianite and garnet are more or less the same. Two generations of garnet are identified which include a group of pale brown, fine- to medium-grained, homogeneous, isotropic and anhedral garnets, and a less common group of late-formed garnets that displayed distinctive zonation patterns and are more heterogeneous and birefringent. The zoned garnets display a very high positive relief with the outer zone of the garnet grain appearing colourless and the inner zone pale brown (Fig. 23). In CS4a samples, vesuvianite and garnet grains are enclosed in finer-grained quartz grains (Fig. 24 a-b) filling the interstitial spaces in the rock. Fine-grained diopside, prehnite and very fine-grained carbonate grains are present as accessory phases. Prehnite occurs as low relief, colourless, needle-like remnants that developed as vein-like features in the interstitial spaces of the rock. The optical properties of garnet and vesuvianite, along with the grain size, are similar compared to CS1 minerals; however, most of the garnet and vesuvianite grains do not show any evidence of internal strain such as fracturing. In CS4a samples, very fine-grained carbonate-rich alteration products are also observed in the form of fine-grained carbonate rings in the centre of garnet grains (Fig. 24 c). In CS4b the amount of garnet is substantially less than the garnet observed in CS4a.

 CS4b is dominated by coarse-grained subhedral vesuvianite grains which are mainly poikilitic with numerous inclusions of garnet and diopside (Fig. 24 d). No quartz is observed in the CS4b samples, although modal amounts and the grain size of vesuvianite increases significantly.

The main discerning feature for the M1 group is the abundant microcline content (Fig. 24 e) along with large volumes of fractured, subhedral, brown garnet grains forming a network with hornblende (Fig. 24 f). Large medium-grained microcline occurs within the interstitial spaces along with isolated subhedral titanite grains while rare calcite commonly occurs within the fractured parts of garnet. Rare plagioclase is also observed. Minor amounts of quartz are locally observed replacing garnet (Fig. 24 g). Hornblende partially replaced by carbonate-rich material, occur as fine- to medium-grained green anhedral crystals. Microcline occurs as fine-medium-grained subhedral, colourless crystals with some exhibiting their characteristic cross-hatch twinning. Microcline also displays some weak alteration of sericitization (Fig. 24 h).
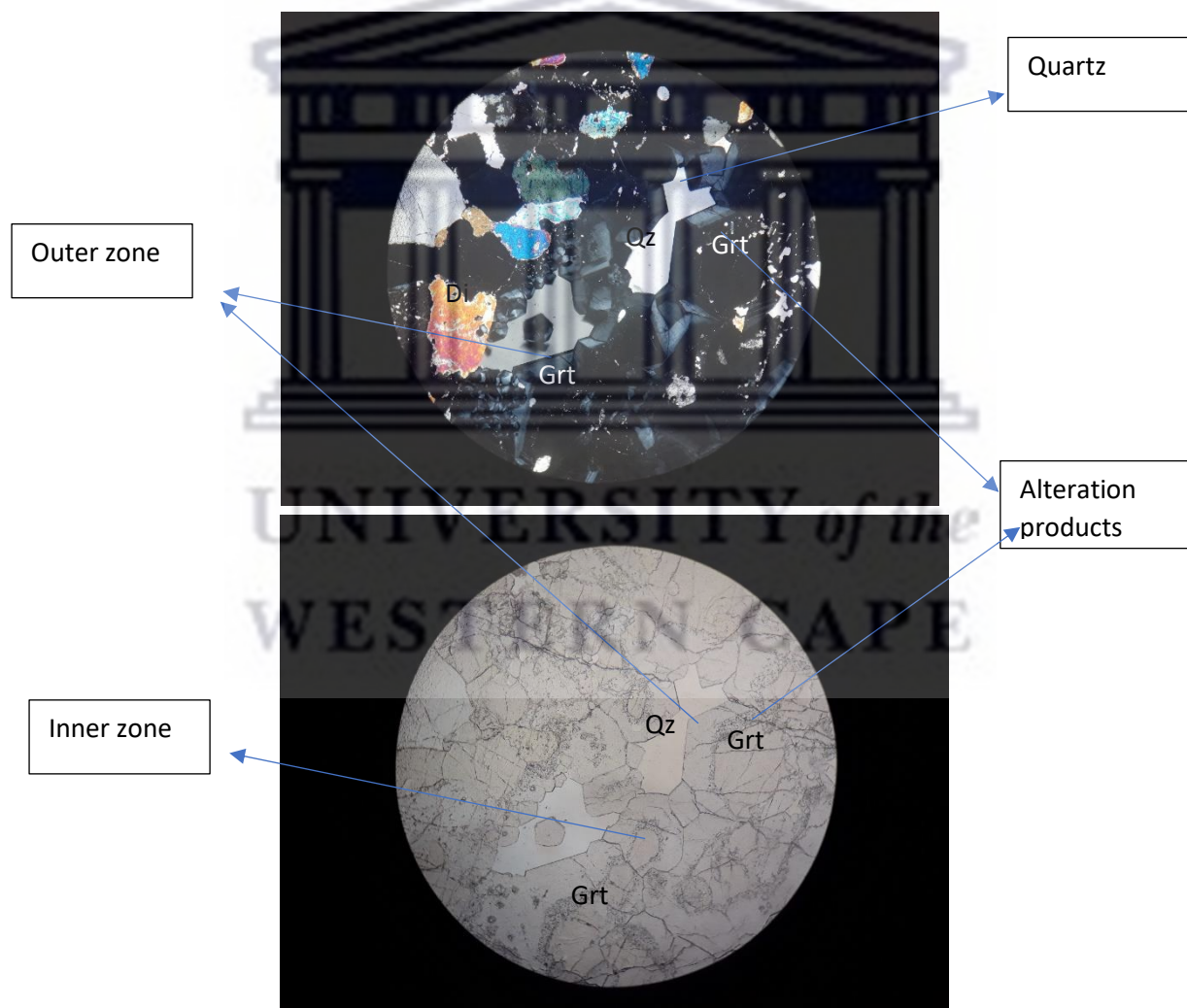
Figure 23: Anisotropic zoned garnet grains with perfect crystal faces. F.O.V. 5mm. Sample number 203.
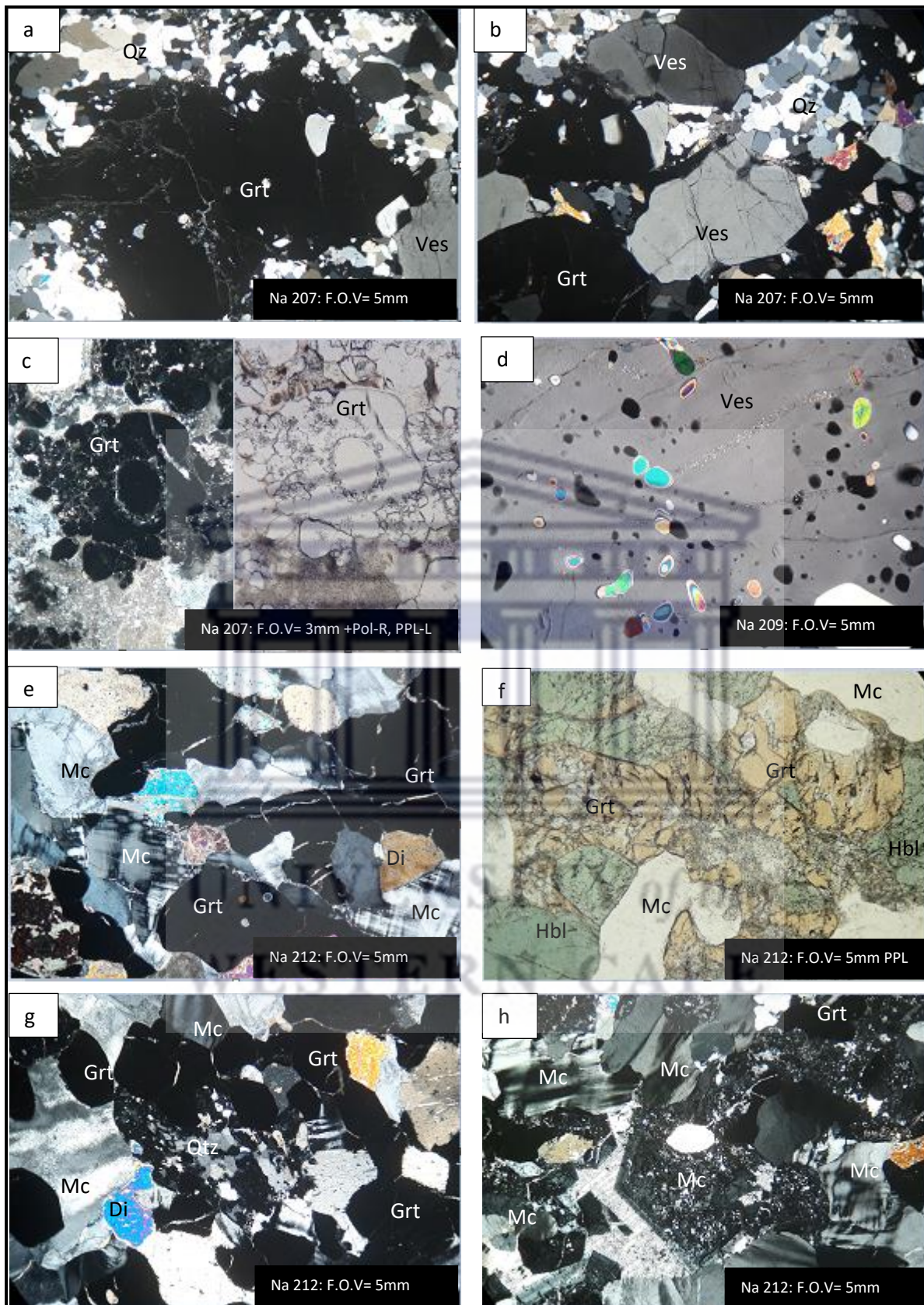
Figure 24: Microphotographs of rock samples from the CS4 and M1 rock group. (a-b) Garnet and vesuvianite grains surrounded by fine-grained quartz grains in CS4 group. (c) Fine-grained material crystallised in the centre of garnet grains. (d) Coarse-grained poikilitic vesuvianite grains with numerous inclusions of garnet and diopside. (e) Microcline-rich rock forming part of the M1 rock group. (f) Interlocking texture between garnet and hornblende. (g) Microcline-rich section with quartz overgrowing garnet. (h) Microcline displaying alteration. Field of view (F.O.V), Crossed polarizers (+Pol), Plane polarised light (PPL). R-right, L-left.

3.3. Mineral chemistry

Electron microprobe analyses (Wavelength Dispersive Spectrometry, i.e., WDS) were carried out on a selection of 10 samples, including spot analyses, line scans and element maps. The analysed phases include garnet, clinopyroxene, wollastonite, and vesuvianite. The number of point analyses along with line scans (if any) for each mineral are shown in Tables 4 and 5. Stoichiometric calculations were performed using spreadsheets of Locock (2008), Brady et al. (2022) and Spreadsheets (2011).

Table 5: Number of point analyses for each mineral

Sample	Number of point analyses for each mineral per sample			
	Garnet	Clinopyroxene	Vesuvianite	Wollastonite
Na200		14		3
Na203	21	38	11	3
Na206	5	3		6
Na207	12		12	
Na208	18	14	7	
Na209	12	18	6	2
Na210	6	25		5
Na213	21	10		12
Na216	18	24	6	
Na221	9	28		3

Table 6: Number of line scans for each mineral

Sample	Number of line scans for each mineral per sample	
	Garnet	Clinopyroxene
Na200	1	
Na203	6	
Na206	1	1
Na210	7	2
Na213	1	
Na216	3	2
Na221	1	

3.3.1. Garnet

The analysed garnets form texturally different types. There are two main groups of garnets that can be distinguished. A group of commonly isotropic, anhedral, homogenous garnets that give reasonable calculated endmember compositions, and a second group that is relatively heterogeneous and birefringent with crystal faces developed. These types of garnets are also compositionally zoned. Representative point analyses are given in Table 6. The mineral abbreviations are according to Whitney and Evans (2010).

The more homogenous, garnets exhibit relatively small deviations from the ideal composition. The results indicate that the garnets are essentially a grossular-andradite- solid solution with only small amounts of Mg and Mn. The grossular component is the dominant endmember, ranging between 63.2-77.5 mol%. The andradite content varies from 17.8-30.6 mol% while pyrope is restricted to a very narrow range of 0.5-1.8 mol%. There are also notable contents of calculated exotic endmembers in the analysed garnets. These include hutcheonite ($\{Ca_3\}[Ti_2](SiAl_2)O_{12}$) with a range of 0.8-1.2 mol%, morimotoite ($\{Ca_3\}[TiFe](Si_3)O_{12}$) with a range of 0.0-3.1 mol% and morimotoite-Mg ($\{Ca_3\}[TiMg](Si_3)O_{12}$) with a range of 0.0-2.0 mol%. Very small amounts of spessartine and almandine are present in a few of the garnets with mol percentages ranging from 0-0.5 mol% and 0-0.1 mol%.

Representative line scan analyses are given in Table 7. A few garnet grains from sample Na203 show major element zonation, as indicated by the variations in grey scale, reflecting the atomic number contrast, in BSE (Backscattered Electron) images shown in Fig. 25a. Sample Na203 contains both groups of garnets described, which are distinguishable based on their optical properties (i.e., garnets that are euhedral with perfect faces developed, zoned with an inner part that is slightly yellow to pale brown and an outer part that is colourless, anisotropic with a very high relief and a second type of garnet that is anhedral, isotropic with high relief). Zoned garnets contain a number of two to three zones in a single grain. A garnet grain that consists of three different zones is divided into the innermost part, also referred to as the centre/core, while the part close to the grain surface is called the rim and the area in between are referred to as the intermediate zone. Garnet 1, 2 and 3 from sample Na203 are distinctly zoned belonging to the second group of garnets described in the analysed samples. Garnets Na203-1 and Na203-2 are similar in composition, each displaying three distinctive zones. According to the BSE images, the centres of garnet Na203-1 and Na203-2 have higher average

atomic numbers and appear light grey, similar to the rim. The intermediate zone of these garnet grains has a lower atomic number and appears medium-dark grey. Transitions between zones are relatively abrupt.

Compositional zoning profiles of zoned garnets for Na203-1-2-3 are shown in Fig. 25 b-c-d. The ratio between grossular and andradite in zoned garnets fluctuates a lot. The compositional profiles of garnet along with element distribution maps indicate chemical variation with Fe-enriched centres and rims relative to the intermediate zone. The grossular component in all zoned garnet grains decreases with an increase in andradite and vice versa. In Na203-1 and Na203-2, andradite increases slightly towards the rim with a decrease in the grossular component. The centres of these grains are higher in the andradite component compared to the rim with a major drop in grossular. The intermediate zones are very high in the grossular component with very low amounts of andradite. Pyrope and uvarovite show low amounts at the core, being absent at the rim and intermediate zone. From rim-to-rim spessartine content remains relatively constant with very low concentrations (≤ 0.5 mol%). Element distribution maps (Fig. 29) for Al show lower concentrations at the rim and in the centre compared to the intermediate zone while the Fe content at the rim and centre is significantly higher, indicating a substitution between Al and Fe^{3+}. The intermediate zone of garnet grains contains slightly higher levels of Al with lower levels of Fe. In garnet 203-3 (Fig. 25d) andradite increases slightly towards the rim while grossular shows a weak rimward decrease. Garnets from sample Na216 (Fig. 26) show a slight increase in grossular towards the rim while andradite show a weak rimward decrease. Concentrations of Mn and Mg are very low.

Some garnet grains, along with coronal garnet in the same samples, have homogeneous chemical compositions with no systematic zoning developed as shown by element distribution maps (Fig. 30), compositional profiles and the BSE images. Garnets from samples Na203-4, Na203-5 shown in Fig. 27, and garnets from Na210-1, Na210-2, Na210-3 and Na210-4 shown in Fig. 28, are essentially homogeneous with respect to grossular, andradite and pyrope.

45

Table 7: Representative point analyses of garnet

Sample	Na 203			Na 206	Na 207			Na 208			Na 209		Na 210		Na 213		Na 216	
	Grt 1	Grt 2	Grt3	Grt 1	Grt 1	Grt 2	Grt 3	Grt 1	Grt 2	Grt 3	Grt 1	Grt 2	Grt 1	Grt 2	Grt 1	Gr t2	Grt 1	Grt 2
Oxide weight percentage																		
SiO_2	38,95	38,80	38,72	38,86	39,01	39,14	39,04	38,92	38,90	38,93	38,87	38,50	38,28	38,55	38,42	38,99	38,54	38,44
TiO_2	0,51	0,61	0,62	0,98	0,27	0,30	0,26	0,63	0,69	0,61	0,65	0,76	1,07	1,07	0,53	0,53	1,33	0,71
Al_2O_3	17,19	17,42	17,17	16,29	17,79	18,31	18,03	16,67	16,81	16,70	16,99	17,10	14,51	14,88	17,81	18,08	16,18	17,57
Cr_2O_3	0,01	0,00	0,01	0,00	0,00	0,01	0,02	0,00	0,00	0,05	0,05	0,02	0,00	0,01	0,00	0,00	0,01	0,01
Fe_2O_3	0,00	0,00	0,00	0,00	0,00	0,00	0,00	0,00	0,00	0,00	0,00	0,00	0,00	0,00	0,00	0,00	0,00	0,00
FeO	6,80	6,73	6,79	7,31	6,26	5,60	5,97	7,40	7,28	7,22	6,89	7,26	9,73	9,38	6,18	6,11	7,49	6,32
MnO	0,19	0,26	0,20	0,14	0,18	0,17	0,20	0,14	0,14	0,19	0,14	0,16	0,21	0,21	0,34	0,38	0,15	0,21
MgO	0,43	0,46	0,42	0,40	0,43	0,44	0,40	0,42	0,44	0,44	0,38	0,45	0,38	0,42	0,25	0,26	0,52	0,29
CaO	36,05	35,72	35,85	36,09	36,10	36,11	36,12	35,85	35,88	35,86	35,92	35,75	35,54	35,60	36,32	36,08	35,73	36,45
Total	100,13	100,00	99,78	100,06	100,04	100,08	100,04	100,03	100,15	100,00	99,89	100,01	99,72	100,12	99,85	100,42	99,96	100,00
Formula																		
Si	2,976	2,967	2,969	2,981	2,975	2,978	2,976	2,983	2,977	2,984	2,980	2,949	2,969	2,974	2,940	2,966	2,963	2,939
Al	0,024	0,033	0,031	0,019	0,025	0,022	0,024	0,017	0,023	0,016	0,020	0,051	0,031	0,026	0,060	0,034	0,037	0,061
Sum Tet	3,000	3,000	3,000	3,000	3,000	3,000	3,000	3,000	3,000	3,000	3,000	3,000	3,000	3,000	3,000	3,000	3,000	3,000
Ti	0,029	0,035	0,036	0,056	0,015	0,017	0,015	0,036	0,040	0,035	0,037	0,044	0,062	0,062	0,030	0,031	0,077	0,041
Al	1,524	1,538	1,521	1,454	1,575	1,620	1,595	1,488	1,493	1,492	1,515	1,493	1,295	1,327	1,546	1,587	1,428	1,522
Cr	0,001	0,000	0,001	0,000	0,000	0,000	0,001	0,000	0,000	0,003	0,003	0,001	0,000	0,001	0,000	0,000	0,001	0,001
Fe^{2+}	0,000	0,003	0,000	0,017	0,000	0,000	0,000	0,018	0,016	0,012	0,014	0,000	0,020	0,031	0,000	0,000	0,027	0,000
Fe^{3+}	0,434	0,425	0,435	0,452	0,399	0,356	0,381	0,456	0,450	0,451	0,427	0,465	0,611	0,574	0,395	0,386	0,454	0,404
Mn^{3+}	0,007	0,000	0,002	0,000	0,012	0,010	0,013	0,000	0,000	0,000	0,000	0,003	0,000	0,000	0,022	0,000	0,000	0,014
Mg	0,005	0,000	0,005	0,020	0,000	0,000	0,000	0,001	0,001	0,007	0,003	0,000	0,011	0,005	0,007	0,000	0,012	0,019
sum A	2,000	2,000	2,000	2,000	2,001	2,004	2,005	2,000	2,000	2,000	2,000	2,007	2,000	2,000	2,000	2,004	2,000	2,000
Fe^{2+}	0,000	0,003	0,000	0,000	0,000	0,000	0,000	0,000	0,000	0,000	0,000	0,000	0,000	0,000	0,000	0,003	0,000	0,000
Mn^{2+}	0,005	0,017	0,011	0,009	0,000	0,001	0,000	0,009	0,009	0,012	0,009	0,007	0,014	0,014	0,000	0,024	0,010	0,000
Mg	0,044	0,053	0,043	0,025	0,049	0,050	0,045	0,047	0,049	0,043	0,040	0,052	0,033	0,044	0,022	0,029	0,047	0,014
Ca	2,951	2,927	2,946	2,966	2,950	2,944	2,950	2,944	2,942	2,945	2,950	2,934	2,953	2,943	2,978	2,941	2,943	2,986
Sum B	3,000	3,000	3,000	3,000	2,999	2,996	2,995	3,000	3,000	3,000	3,000	2,993	3,000	3,000	3,000	2,996	3,000	3,000
Endmember																		
Blythite	0,2%	0,0%	0,1%	0,0%	0,0%	0,1%	0,0%	0,0%	0,0%	0,0%	0,0%	0,2%	0,0%	0,0%	0,0%	0,0%	0,0%	0,0%
Hutcheonite	1,2%	1,6%	1,5%	1,0%	0,8%	0,9%	0,8%	0,9%	1,2%	0,8%	1,0%	2,2%	1,6%	1,3%	1,5%	1,5%	1,9%	2,0%
Morimotoite	0,0%	0,3%	0,0%	1,7%	0,0%	0,0%	0,0%	1,8%	1,6%	1,2%	1,5%	0,0%	2,0%	3,1%	0,0%	0,0%	2,7%	0,0%
Morimotoite-Mg	0,5%	0,0%	0,5%	2,0%	0,0%	0,0%	0,0%	0,1%	0,1%	0,7%	0,3%	0,0%	1,1%	0,5%	0,0%	0,0%	1,2%	0,0%
Uvarovite	0,0%	0,0%	0,0%	0,0%	0,0%	0,0%	0,1%	0,0%	0,0%	0,2%	0,2%	0,1%	0,0%	0,0%	0,0%	0,0%	0,0%	0,0%
Spessartine	0,0%	0,6%	0,3%	0,3%	0,0%	0,0%	0,0%	0,3%	0,3%	0,4%	0,3%	0,1%	0,5%	0,5%	0,0%	0,8%	0,3%	0,0%
Pyrope	1,5%	1,8%	1,5%	0,8%	1,6%	1,7%	1,5%	1,6%	1,6%	1,4%	1,3%	1,7%	1,1%	1,5%	0,7%	1,0%	1,6%	0,5%
Almandine	0,0%	0,1%	0,0%	0,0%	0,0%	0,0%	0,0%	0,0%	0,0%	0,0%	0,0%	0,0%	0,0%	0,0%	0,0%	0,1%	0,0%	0,0%
Grossular	74,7%	74,5%	74,4%	71,6%	77,1%	79,4%	78,3%	72,6%	72,7%	72,8%	74,1%	72,9%	63,2%	64,4%	76,6%	77,5%	69,5%	75,6%
Andradite	21,7%	21,2%	21,8%	22,6%	20,0%	17,8%	19,0%	22,8%	22,5%	22,6%	21,4%	22,7%	30,6%	28,7%	19,8%	19,0%	22,7%	20,2%
Remainder	0,2%	0,0%	0,0%	0,0%	0,5%	0,2%	0,4%	0,0%	0,0%	0,0%	0,0%	0,2%	0,0%	0,0%	1,4%	0,1%	0,0%	1,6%
Total	100,0%	100,0%	100,0%	100,0%	100,0%	100,0%	100,0%	100,0%	100,0%	100,0%	100,0%	100,0%	100,0%	100,0%	100,0%	100,0%	100,0%	100,0%

Table 8: Representative analyses of garnet from line scans

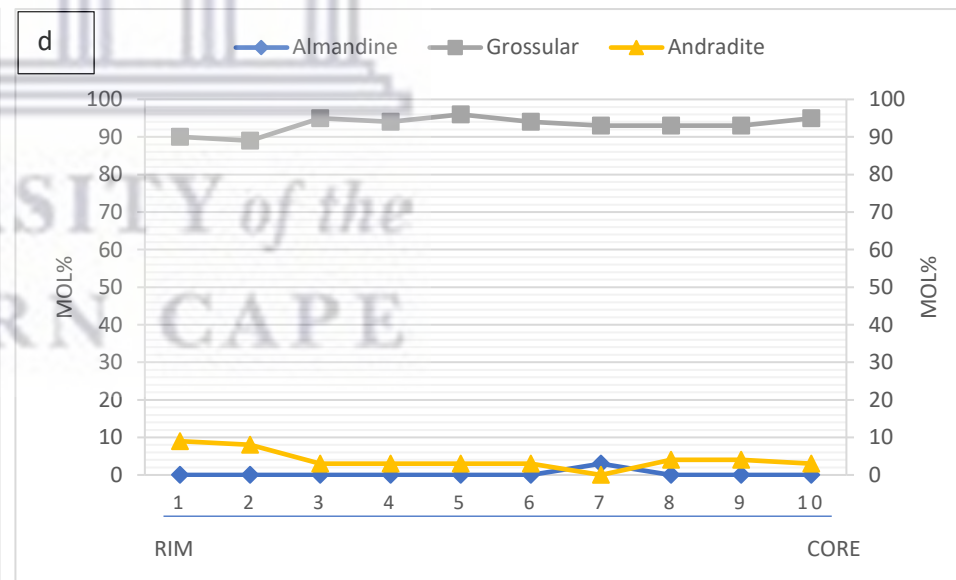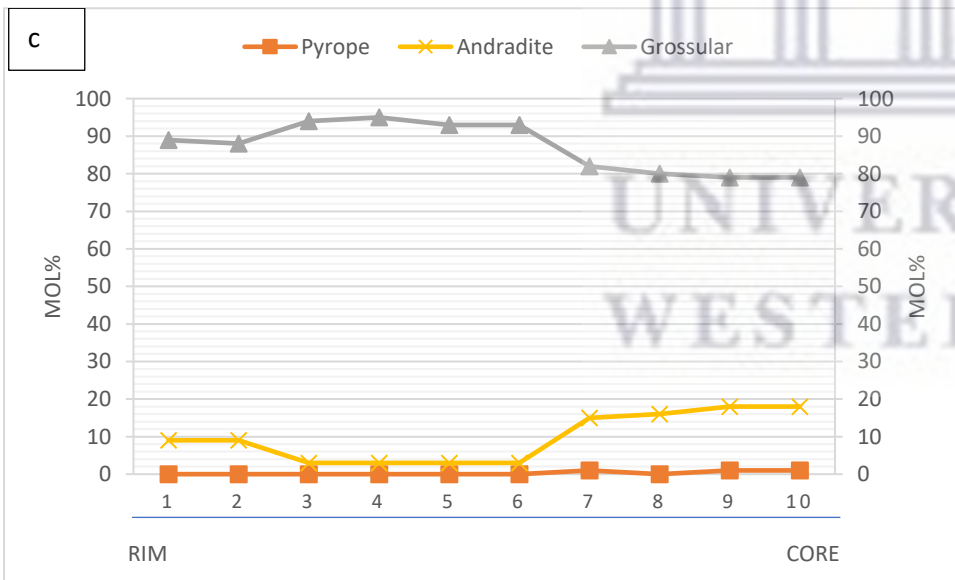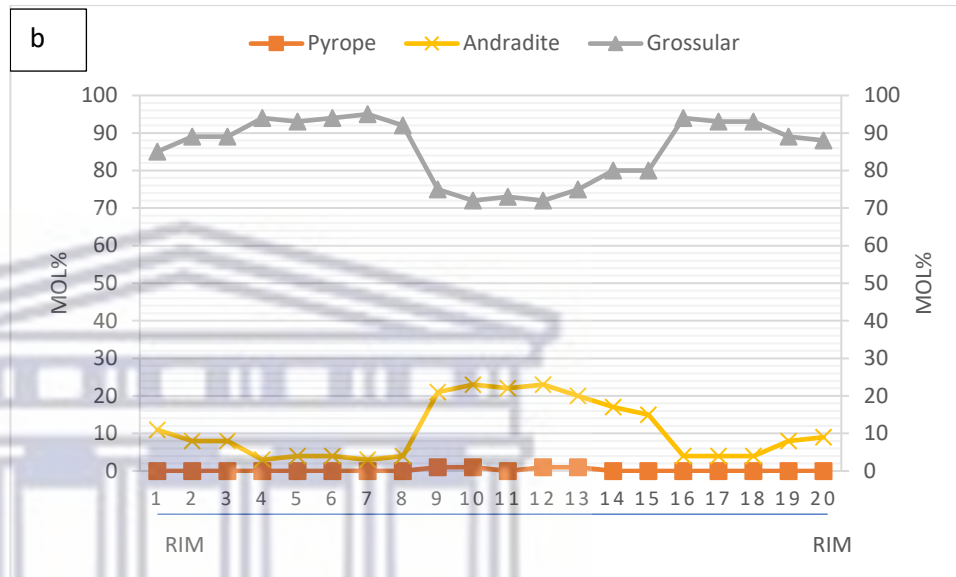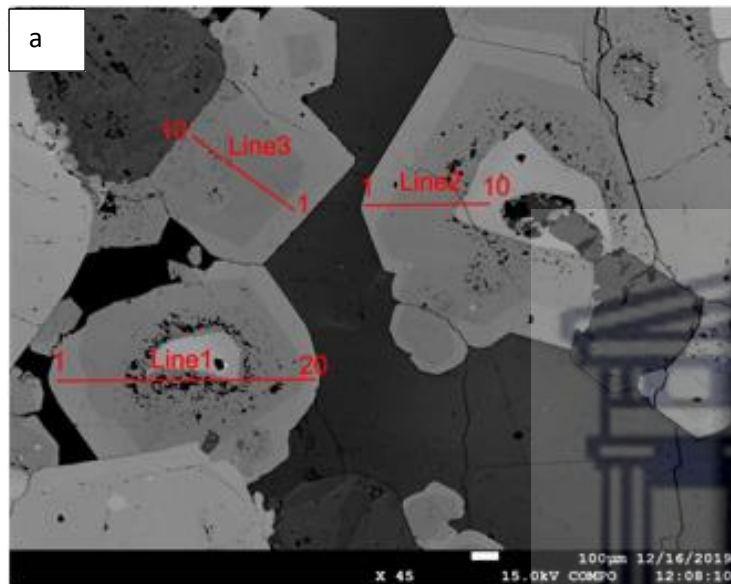| Sample	Na 203															Na 216						Na 210							
	Grt 1			Grt 2			Grt 3			Grt 4			Grt 5			Grt 1			Grt 3			Grt 1		Grt 2		Grt 3		Grt 4	
comment	distinctly zoned birefringent show crystal faces			distinctly zoned birefringent show crystal faces			distinctly zoned birefringent show crystal faces			homogeneous isotropic anhedral			homogeneous isotropic anhedral			homogeneous isotropic anhedral			weakly zoned isotropic anhedral			Homogeneous Isotropic anhedral		Homogeneous Isotropic anhedral		Homogeneous Isotropic anhedral		Homogeneous Isotropic anhedral	
	Line 1			Line 2			Line 3			Line 1			Line 2			Line 1			Line 3			Line 1		Line 2		Line 3		Line 4	
	core	intm	rim	core	intm	rim	core	intm	rim	core	intm	rim	core	intm	rim	core	intm	rim	core	intm	rim	core	rim	core	rim	core	rim	core	rim
major oxides weight percentage																													
SiO_2	37,90	39,39	38,91	39,37	39,24	39,76	39,33	39,46	40,04	39,14	38,95	38,63	38,85	38,98	38,95	38,90	38,89	38,77	38,76	38,76	38,18	38,08	38,59	38,03	38,08	38,41	38,21	38,18	38,19
TiO_2	0,54	0,00	0,36	0,44	0,03	0,42	0,00	0,00	0,14	0,68	0,71	0,75	0,74	0,67	0,72	1,25	1,22	0,95	1,15	1,07	0,73	1,06	1,08	1,12	1,06	1,13	1,07	1,06	1,07
Al_2O_3	17,46	21,79	19,49	18,30	21,87	20,58	22,07	22,17	20,60	17,10	17,11	17,10	17,11	16,96	17,31	15,98	16,15	16,84	16,36	16,49	17,42	14,30	14,53	14,32	14,46	14,46	14,34	14,53	14,61
Cr_2O_3	0,05	0,00	0,00	0,01	0,00	0,00	0,00	0,02	0,00	0,04	0,00	0,00	0,03	0,00	0,02	0,04	0,04	0,04	0,02	0,01	0,01	0,00	0,00	0,00	0,00	0,00	0,00	0,04	0,00
Fe_2O_3	0,00	0,00	0,00	0,00	0,00	0,00	0,00	0,00	0,00	0,00	0,00	0,00	0,00	0,00	0,00	0,00	0,00	0,00	0,00	0,00	0,00	0,00	0,00	0,00	0,00	0,00	0,00	0,00	0,00
FeO	6,26	0,89	3,53	5,97	0,95	2,87	0,85	0,89	2,93	7,15	7,18	6,83	7,06	7,19	6,80	7,72	7,58	6,76	7,47	7,42	6,45	9,89	9,84	10,16	9,82	9,97	9,74	9,96	9,72
MnO	0,20	0,17	0,14	0,19	0,14	0,13	0,06	0,07	0,10	0,21	0,18	0,22	0,16	0,21	0,24	0,12	0,18	0,19	0,15	0,19	0,18	0,20	0,24	0,22	0,22	0,25	0,24	0,21	0,28
MgO	0,43	0,00	0,01	0,37	0,01	0,01	0,01	0,00	0,01	0,46	0,44	0,48	0,39	0,42	0,45	0,42	0,39	0,34	0,47	0,45	0,32	0,38	0,36	0,35	0,30	0,36	0,38	0,39	0,36
CaO	35,84	37,86	37,38	36,45	38,15	37,73	38,09	38,11	37,45	35,91	35,91	35,86	36,06	35,91	35,97	35,93	35,99	36,11	35,87	35,75	36,37	35,31	35,37	35,39	35,23	35,44	35,51	35,40	35,48
Total	98,68	100,10	99,83	101,10	100,38	101,50	100,40	100,72	101,28	100,69	100,49	99,88	100,40	100,34	100,46	100,37	100,44	100,00	100,24	100,15	99,66	99,22	100,01	99,59	99,17	100,02	99,49	99,77	99,70
Formula																													
Si	2,933	2,958	2,956	2,970	2,938	2,965	2,943	2,944	2,990	2,977	2,969	2,960	2,964	2,976	2,967	2,981	2,977	2,971	2,969	2,971	2,929	2,970	2,986	2,957	2,972	2,973	2,971	2,961	2,963
Al	0,067	0,042	0,044	0,030	0,062	0,035	0,057	0,056	0,010	0,023	0,031	0,040	0,036	0,024	0,033	0,019	0,023	0,029	0,031	0,029	0,071	0,030	0,014	0,043	0,028	0,027	0,029	0,039	0,037
Sum Tet	3,000	3,000	3,000	3,000	3,000	3,000	3,000	3,000	3,000	3,000	3,000	3,000	3,000	3,000	3,000	3,000	3,000	3,000	3,000	3,000	3,000	3,000	3,000	3,000	3,000	3,000	3,000	3,000	3,000
Ti	0,031	0,000	0,021	0,025	0,002	0,023	0,000	0,000	0,008	0,039	0,041	0,043	0,043	0,038	0,041	0,072	0,070	0,055	0,066	0,062	0,042	0,062	0,063	0,066	0,062	0,066	0,063	0,062	0,062
Al	1,526	1,887	1,701	1,597	1,868	1,773	1,889	1,893	1,804	1,511	1,506	1,505	1,502	1,502	1,521	1,424	1,434	1,493	1,447	1,461	1,505	1,284	1,311	1,270	1,302	1,292	1,286	1,289	1,298
Cr	0,003	0,000	0,000	0,000	0,000	0,000	0,000	0,001	0,000	0,003	0,000	0,000	0,002	0,000	0,000	0,003	0,003	0,003	0,001	0,001	0,001	0,000	0,000	0,000	0,000	0,000	0,002	0,000	0,000
Fe^{2+}	0,000	0,000	0,000	0,000	0,000	0,000	0,000	0,000	0,000	0,016	0,009	0,000	0,003	0,014	0,005	0,046	0,038	0,009	0,028	0,032	0,000	0,024	0,048	0,019	0,034	0,039	0,015	0,023	0,016
Fe^{3+}	0,405	0,056	0,224	0,377	0,059	0,179	0,053	0,055	0,183	0,432	0,444	0,438	0,448	0,445	0,429	0,449	0,448	0,424	0,451	0,444	0,414	0,621	0,578	0,641	0,602	0,603	0,618	0,623	0,615
Mn^{3+}	0,013	0,011	0,009	0,006	0,009	0,008	0,004	0,004	0,006	0,000	0,000	0,011	0,000	0,000	0,000	0,000	0,000	0,000	0,000	0,000	0,012	0,000	0,000	0,000	0,000	0,000	0,000	0,000	0,000
Mg	0,022	0,001	0,001	0,000	0,001	0,001	0,001	0,000	0,000	0,000	0,000	0,003	0,003	0,048	0,003	0,007	0,009	0,017	0,008	0,001	0,027	0,008	0,000	0,004	0,000	0,000	0,019	0,000	0,009
sum A	2,000	1,953	1,957	2,005	1,939	1,985	1,946	1,954	2,001	2,000	2,000	2,000	2,000	2,048	1,999	2,000	2,000	2,000	2,000	2,000	2,000	2,000	2,000	2,000	2,000	2,000	2,000	2,000	2,000
Fe^{2+}	0,000	0,000	0,000	0,000	0,000	0,000	0,000	0,000	0,000	0,000	0,005	0,000	0,000	0,000	0,000	0,000	0,000	0,000	0,000	0,000	0,000	0,000	0,010	0,000	0,005	0,003	0,000	0,000	0,000
Mn^{2+}	0,000	0,000	0,000	0,006	0,000	0,000	0,000	0,000	0,000	0,014	0,012	0,003	0,010	0,014	0,015	0,008	0,012	0,013	0,010	0,013	0,013	0,013	0,016	0,014	0,014	0,016	0,016	0,014	0,018
Mg	0,028	0,000	0,000	0,042	0,000	0,000	0,000	0,000	0,001	0,052	0,050	0,052	0,042	0,048	0,048	0,042	0,036	0,022	0,046	0,051	0,010	0,036	0,042	0,037	0,035	0,042	0,026	0,045	0,033
Ca	2,972	3,046	3,043	2,946	3,061	3,014	3,053	3,046	2,997	2,927	2,933	2,944	2,948	2,938	2,936	2,950	2,952	2,965	2,944	2,936	2,990	2,951	2,932	2,949	2,946	2,939	2,959	2,942	2,949
Sum B	3,000	3,046	3,043	2,994	3,061	3,014	3,053	3,046	2,998	3,000	3,000	3,000	3,000	3,000	3,000	3,000	3,000	3,000	3,000	3,000	3,000	3,000	3,000	3,000	3,000	3,000	3,000	3,000	3,000
Endmember																													
Blythite	0,0%	0,0%	0%	0,2%	0,0%	0,0%	0,0%	0,0%	0,0%	0,0%	0,0%	0,1%	0,0%	0,0%	0,0%	0,0%	0,0%	0,0%	0,0%	0,0%	0,0%	0,0%	0,0%	0,0%	0,0%	0,0%	0,0%	0,0%	0,0%
Hutcheonite	1,6%	0,0%	1%	1,2%	0,1%	1,2%	0,0%	0,0%	0,4%	1,1%	1,6%	2,0%	1,8%	1,2%	1,6%	1,0%	1,2%	1,4%	1,5%	1,4%	2,1%	1,5%	0,7%	2,1%	1,4%	1,4%	1,4%	2,0%	1,9%
Morimotoite	0,0%	0,0%	0%	0,0%	0,0%	0,0%	0,0%	0,0%	0,0%	1,6%	0,9%	0,0%	0,3%	1,4%	0,5%	4,6%	3,8%	0,9%	2,8%	3,2%	0,0%	2,4%	4,8%	1,9%	3,4%	3,9%	1,5%	2,3%	1,6%
Morimotoite-Mg	0,0%	0,0%	0%	0,0%	0,0%	0,0%	0,0%	0,0%	0,3%	0,0%	0,0%	0,3%	0,3%	0,0%	0,3%	0,7%	0,9%	1,7%	0,8%	0,1%	0,0%	0,8%	0,0%	0,4%	0,0%	0,0%	1,9%	0,1%	0,9%
Uvarovite	0,2%	0,0%	0%	0,0%	0,0%	0,0%	0,0%	0,1%	0,0%	0,1%	0,0%	0,1%	0,1%	0,0%	0,1%	0,1%	0,1%	0,1%	0,1%	0,0%	0,0%	0,0%	0,0%	0,0%	0,0%	0,0%	0,1%	0,1%	0,0%
Spessartine	0,0%	0,0%	0%	0,0%	0,0%	0,0%	0,0%	0,0%	0,0%	0,5%	0,4%	0,0%	0,4%	0,5%	0,5%	0,3%	0,4%	0,4%	0,3%	0,4%	0,4%	0,4%	0,5%	0,5%	0,5%	0,5%	0,5%	0,5%	0,6%
Pyrope	0,9%	0,0%	0%	1,4%	0,0%	0,0%	0,0%	0,0%	0,1%	1,7%	1,7%	1,7%	1,4%	1,6%	1,6%	1,4%	1,2%	0,7%	1,5%	1,7%	0,3%	1,2%	1,4%	1,2%	1,2%	1,4%	0,9%	1,5%	1,1%
Almandine	0,0%	0,0%	0%	0,0%	0,0%	0,0%	0,0%	0,0%	0,0%	0,2%	0,2%	0,0%	0,0%	0,0%	0,0%	0,0%	0,0%	0,0%	0,0%	0,0%	0,0%	0,0%	0,3%	0,0%	0,2%	0,1%	0,0%	0,0%	0,0%
Grossular	75,4%	94,3%	85%	78,5%	93,4%	88,7%	94,4%	94,6%	90,1%	73,1%	73,1%	73,5%	73,4%	73,1%	74,0%	69,6%	70,1%	73,5%	70,5%	71,0%	74,9%	62,6%	63,3%	61,8%	63,3%	62,6%	62,9%	62,5%	63,2%
Andradite	20,3%	2,8%	11%	18,5%	3,0%	9,0%	2,7%	2,8%	9,2%	21,6%	22,2%	21,9%	22,4%	22,3%	21,4%	22,5%	22,4%	21,2%	22,6%	22,2%	20,7%	31,0%	28,9%	32,1%	30,1%	30,2%	30,9%	31,2%	30,7%
Remainder	2,0%	3,0%	3%	0,2%	3,5%	1,2%	2,9%	2,5%	0,3%	0,0%	0,0%	0,4%	0,0%	0,0%	0,0%	0,0%	0,0%	0,0%	0,0%	0,0%	1,9%	0,0%	0,0%	0,0%	0,0%	0,0%	0,0%	0,0%	0,0%
Total	100,3%	100,1%	100%	100,0%	100,0%	100,0%	100,0%	100%	100,0%	100,0%	100,0%	100,0%	100,0%	100,0%	100,0%	100,0%	100,0%	100,0%	100,0%	100,0%	100,0%	100,0%	100,0%	100,0%	100,0%	100,0%	100,0%	100,0%	100,0%

Figure 25: BSE images and compositional profiles of garnet (Sample Na 203). (a) BSE image showing textural features of garnet (scale bar=100 microns). The red lines indicate line locations for microprobe analysis and nearby numbers indicate beginning and end of line. (b) Compositional profile of zoned garnet from rim to rim representing line 1. (c) Compositional profile of zoned garnet from rim to core, representing line 2. (d) Compositional profile of zoned garnet from rim to core representing line 3.
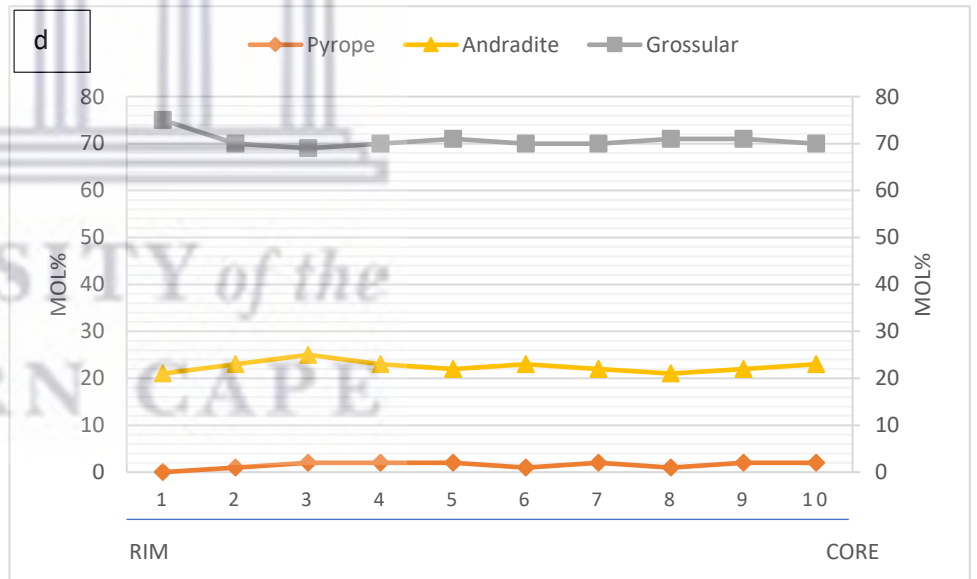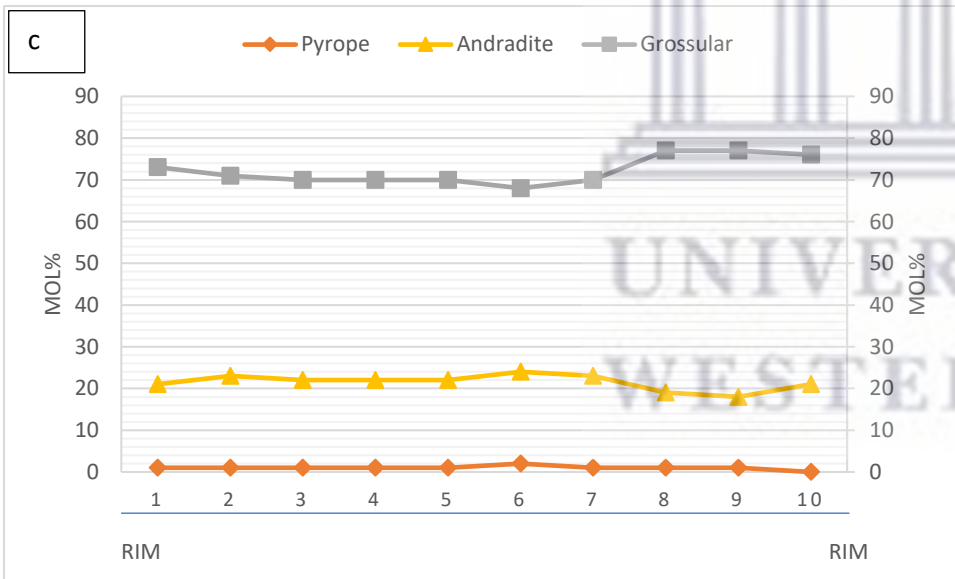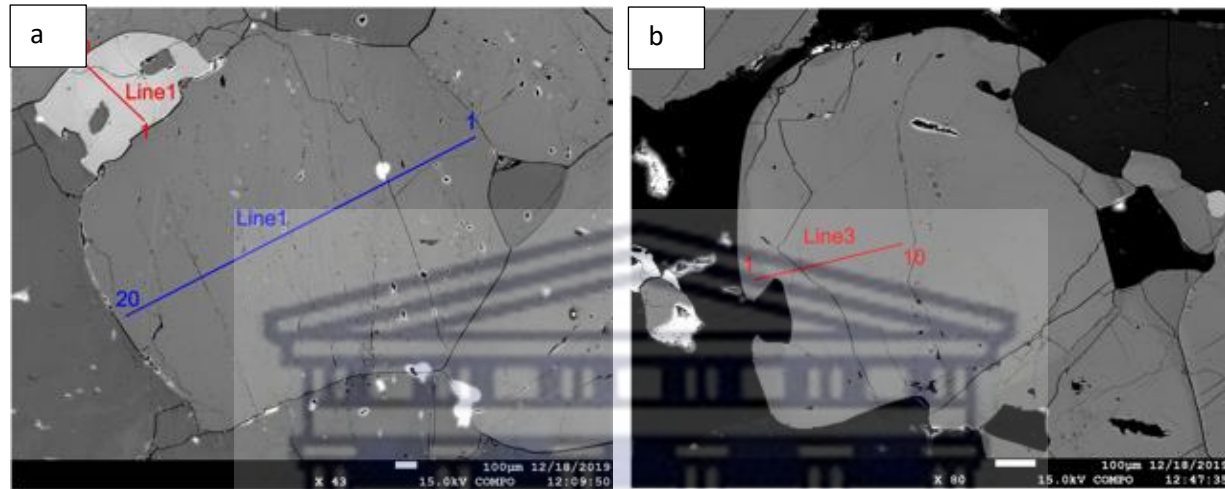
Figure 26: BSE images and compositional profiles of garnet (Sample Na 216). (a-b) BSE images showing textural features of garnet (scale bar=100 microns). The red lines indicate line locations for microprobe analysis for garnet and nearby numbers indicate beginning and end of line. Blue line represents clinopyroxene. Notice how garnet grain is weakly zoned at the rim (c) Compositional profile of weakly zoned garnet from rim to rim representing line 1. (d) Compositional profile of a weakly zoned garnet represented from rim to core representing line 3. Notice slight decrease in Fe at the rim while all other elements remain relatively constant.
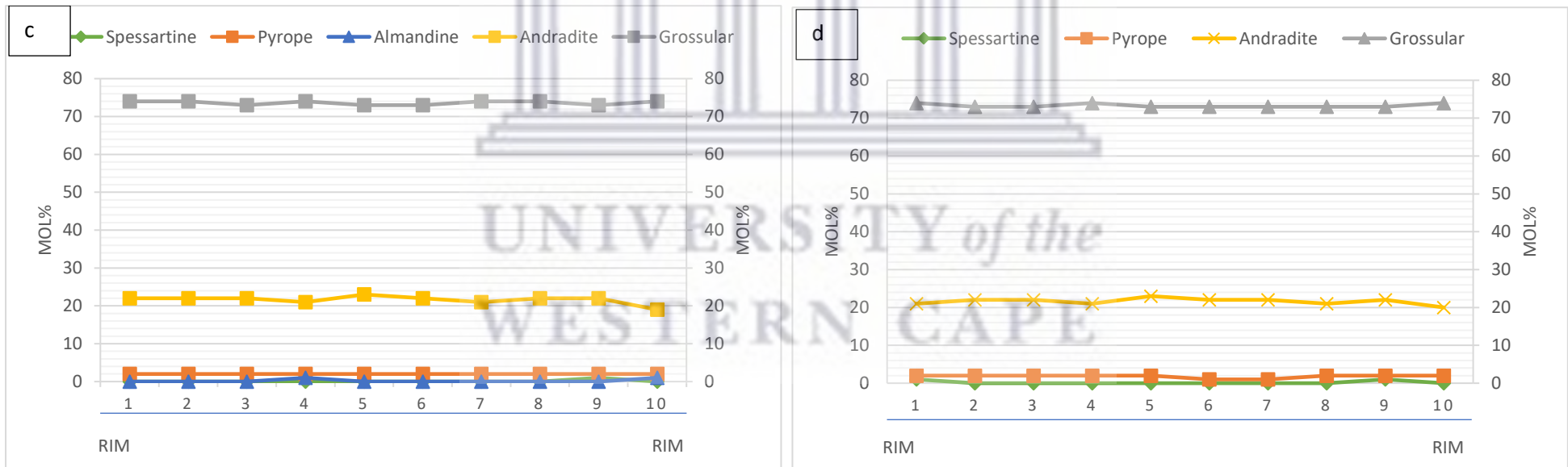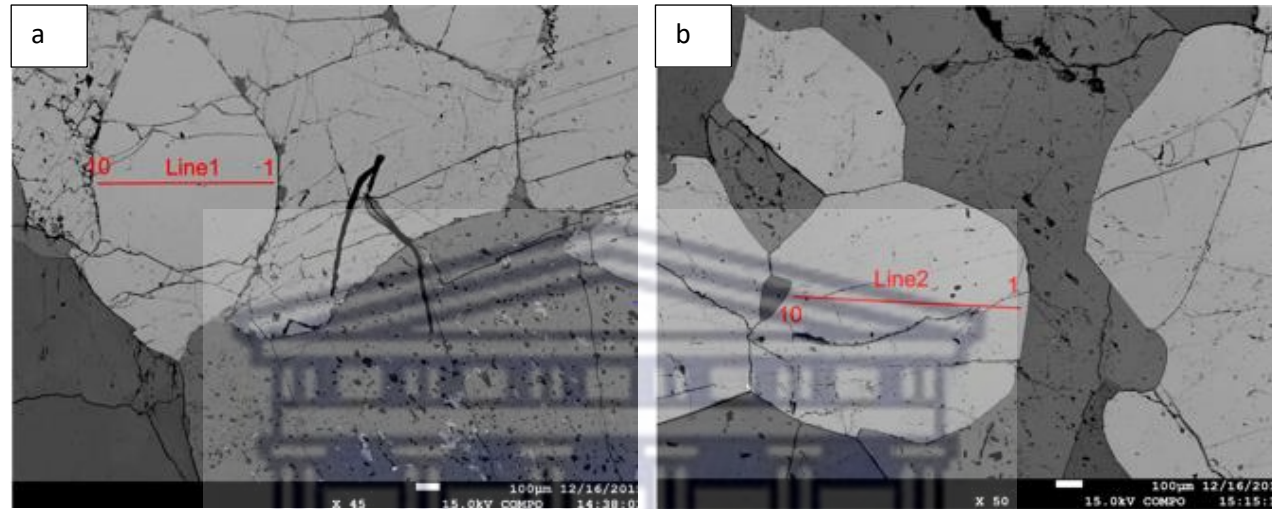
Figure 27: BSE images and compositional profiles of garnet (Sample Na 203). (a-b) BSE images showing textural features of garnet (scale bar=100 microns). The red lines indicate line locations for microprobe analysis and nearby numbers indicate beginning and end of line number. (c) Compositional profile of zoned garnet from rim to rim representing line 1. (d) Compositional profile of zoned garnet from rim to rim, representing line 2.

50

Figure 28: BSE images and compositional profiles of homogeneous garnet (Sample Na 210). (a-b) BSE images showing textural features of garnet (scale bar=100 microns). The red lines indicate line locations for microprobe analysis for garnet and nearby numbers indicate beginning and end of line. Blue lines 1 and 2 represents clinopyroxene. (c) Compositional profile of garnet from rim to rim representing line 2. (d) Compositional profile of garnet represented from rim to rim representing line 4.
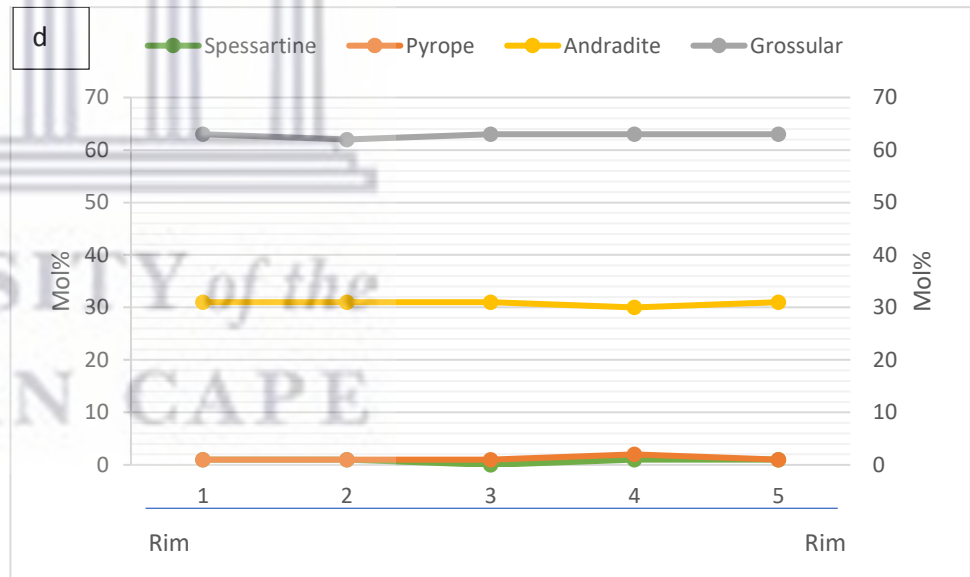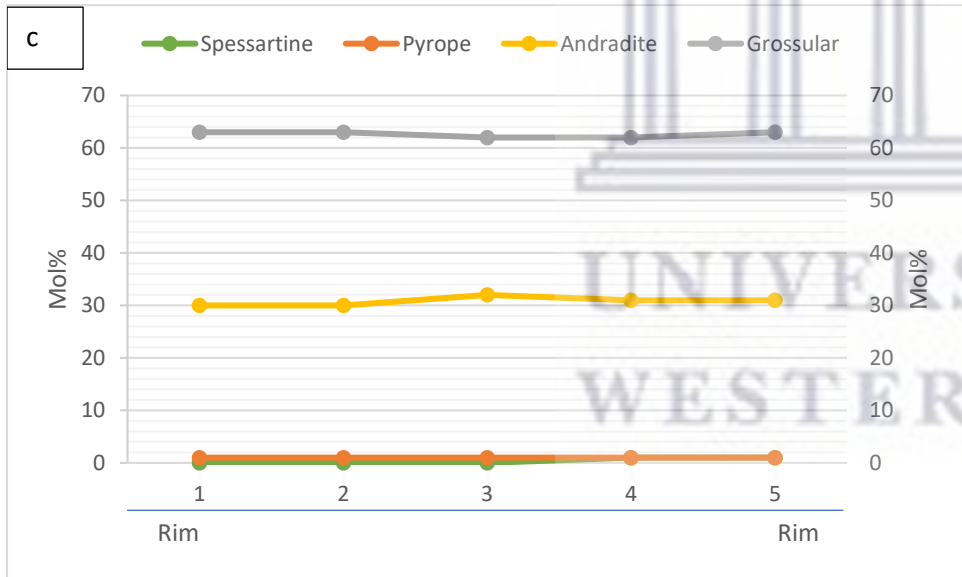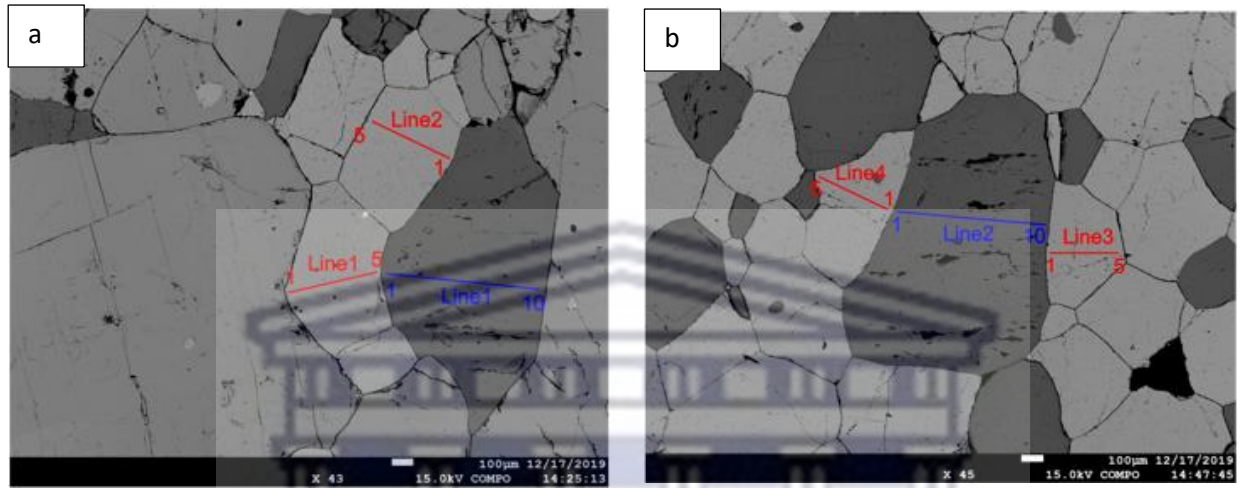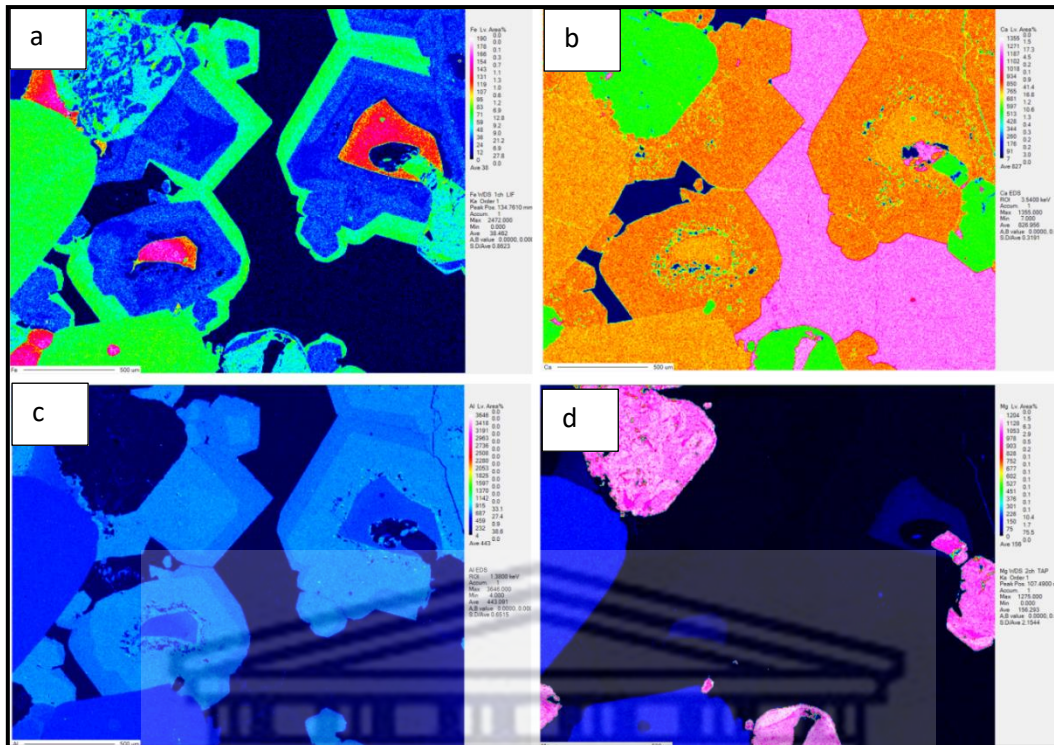
51

Figure 29: Element distribution maps of (a) Fe (b) Ca (c) Al (d) Mg in zoned garnet (Sample Na 203).
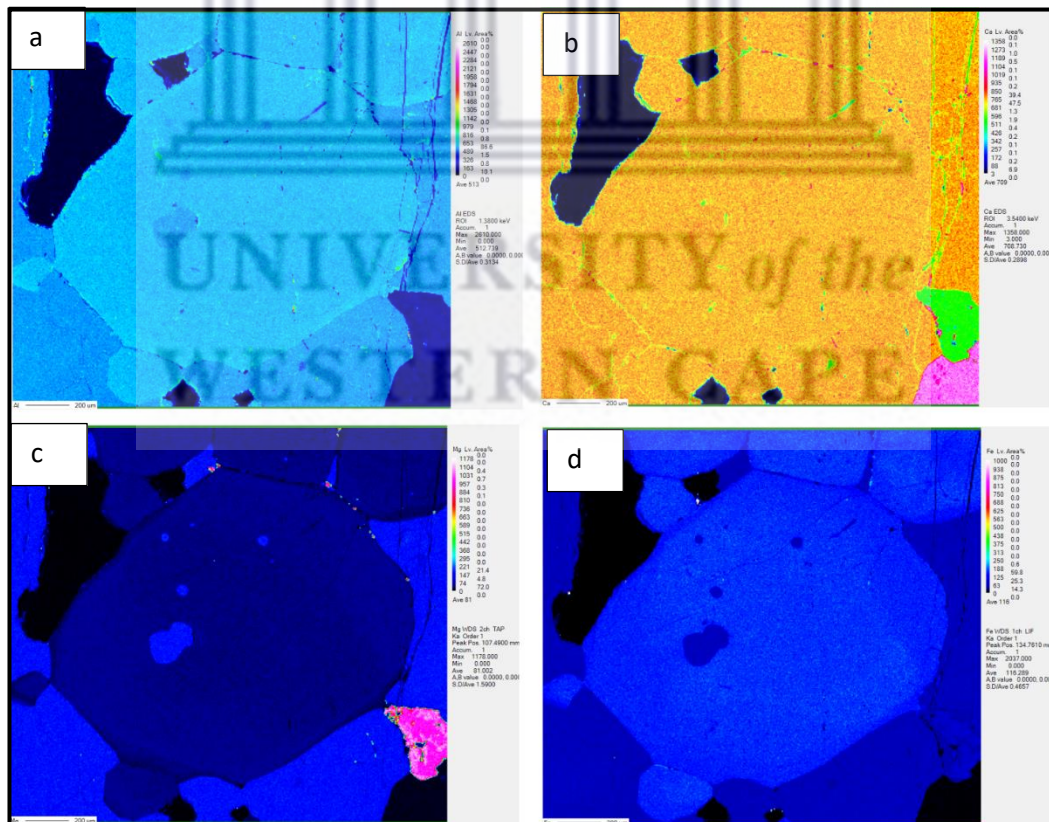

Figure 30: Element distribution maps of (a) Al (b) Ca (c) Mg (d) Fe in homogeneous garnet grains.

3.3.2. Vesuvianite

Vesuvianite stoichiometry was calculated on the basis of 78 anions; the resultant data from the microprobe analyses is presented in Table 8. Vesuvianite chemistry shows a significant amount of fluorine, with concentrations ranging from 1.28- and 1.97 wt.%. BSE images indicate that vesuvianite has a homogeneous chemical composition similar to garnet in the same samples with no distinct variation in their chemistry from rim to core.

Table 9: Representative point analyses of vesuvianite

Sample	Na203	Na207	Na209	Na216
SiO_2	35,56	35,93	35,60	35,54
TiO_2	1,57	0,89	1,97	3,32
Al_2O_3	17,30	18,13	16,78	16,13
FeO	2,93	2,55	3,35	3,20
MnO	0,06	0,04	0,06	0,04
MgO	2,40	2,54	2,50	2,40
CaO	36,18	36,40	36,10	35,93
Na_2O	0,03	0,01	0,04	0,04
K_2O	0,00	0,00	0,00	0,00
Cl	0,02	0,02	0,02	0,01
F	1,68	1,97	1,67	1,28
TOTAL	97,08	97,82	97,42	97,23
O=F,Cl	0,71	0,83	0,70	0,54
TOTAL	96,37	96,99	96,71	96,69
Formula				
Si	18,620	18,650	18,620	18,550
Al	0,000	0,000	0,000	0,000
Ti	0,620	0,350	0,770	1,300
Al	10,680	11,090	10,340	9,920
Fe^{2+}	1,280	1,110	1,470	1,400
Mn	0,030	0,020	0,020	0,020
Mg	1,870	1,970	1,950	1,870
Ca	20,300	20,250	20,230	20,100
Na	0,030	0,010	0,040	0,040
K	0,000	0,000	0,000	0,000
Cl	0,010	0,020	0,010	0,000
F	2,790	3,230	2,750	2,110
TOTAL	53,430	53,450	53,450	53,200

3.3.3. Clinopyroxene

Clinopyroxene composition was calculated based on 6 oxygens. The analysed clinopyroxenes were quantitatively identified as diopside-hedenbergite-Ca-Tschermak-jadeite and johannsenite components. Representative point analyses are given in Table 9. The dominant endmembers include diopside (Di) with a range of 74.4-94.7 mol% and hedenbergite (Hd) ranging from 3.9-20.2 mol%. Ca-Tschermak's molecule (Ca-Ts) varies a bit, but is commonly the third most abundant endmember ranging from 0.0-10.5 mol%. Jadeite (Jd) and johannsenite (Jo) contents vary with a range of 0.4-2.5 mol% and 0.2-0.9 mol% respectively.

In order to calculate the endmember components, a strategic approach was followed assuming that the main endmembers will be Ca-clinopyroxenes (i.e., diopside and hedenbergite). The normalised analyses of the original probe data were used and Fe^{3+} was kept at zero since Fe concentrations is relatively low and can be expected to be dominantly contained in hedenbergite. Calculating Fe^{3+} from the remaining, a very small amount of Fe would introduce a potentially large error when trying to calculate an acmite component. Since Na contents are generally very low, all Na was assigned to jadeite. Na and Ca was then assigned to the M2 site and the rest of the elements to the M1 site, after filling the Si gap in the tetrahedral site with Al. The remaining Al is assigned to the M1 site. The endmember percentages are then calculated from the M1 site occupation, except for Na from the M2 site which gives the jadeite component. Mg, Fe and Mn all combine with Ca to calculate diopside, hedenbergite and johannsenite proportions, respectively. The Ca-Ts component is calculated from the tetrahedral Al and a corresponding amount of Al in M1. The analysed clinopyroxenes exhibit relatively small deviations from an ideal composition with little to no "remainders" present in the endmember calculation.

In the Wo-En-Fs component system, the formal wollastonite (Wo) component is generally dominant and always lies above the Wo 50 mol% line (Fig. 31), with a range of 50.6-52.7 mol%. This excess Ca is taken up by the johannsenite, and more importantly, by the Ca-Tschermak's component. The formal enstatite (En) content varies from 38.8-46.9 mol%, while ferrosilite (Fs) is restricted to a range of 2.1-10.1 mol%.

Representative line scan analyses are given in Table 10. The line scans from the analysed pyroxenes reveal slightly zoned grains with a relatively homogeneous core. BSE images (Fig.

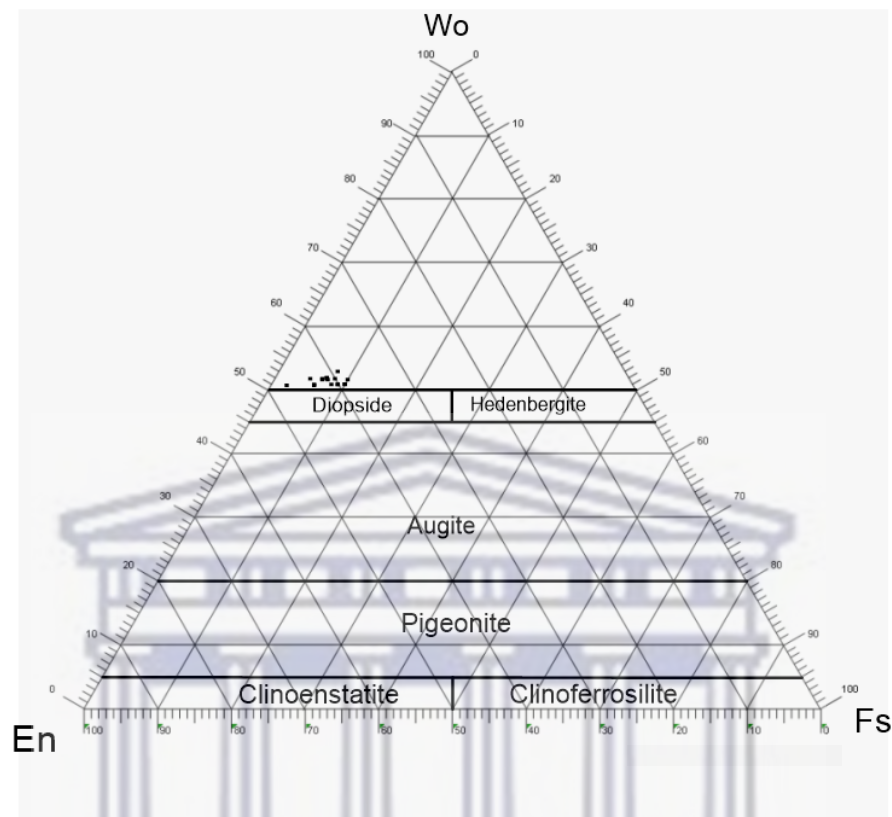32a; Fig. 33a) show a very minor variation between rim to grain centre, with a slightly darker outer rim.

Figure 31: Ternary plot for representative point analyses of clinopyroxene.

Compositional profiles of clinopyroxenes are shown in Fig. 32 b-c and Fig. 33 b-c. Clinopyroxenes from samples Na216-1, Na216-2, Na206-1, Na210-1 and Na210-2 show endmember contents of diopside which has a sharp rimward increase and decreases towards the core. Compositional profiles show that hedenbergite remains relatively constant from rim to rim slightly decreasing or increasing with an increase or decrease in diopside. Ca-Tschermak's molecule show low amounts at the grain boundary increasing towards the core and a sharp rimward decrease near the grain boundary. Both jadeite and johannsenite remain constant from rim to rim with very low amounts.

The compositional profiles along with elemental distribution maps (Fig. 34) indicate weak compositional zoning in some pyroxenes revealing a narrow Mg-rich rim slightly decreasing towards the centre and a narrow Al-poor rim. Al is relatively high in the grain interior while dropping to almost zero at the rim. With an increase in Al there is a decrease in Mg. Mg is high at the rim and slightly decreasing towards the centre.

55

Table 10: Representative point analyses of clinopyroxene

Sample	Na 200		Na 203				Na 206	Na 208			Na 209		Na 210			Na 213		Na 216			Na 221
	Cpx 1	Cpx 2	Cpx 1	Cpx 2	Cpx 3	Cpx 4	Cpx 1	Cpx 1	Cpx 2	Cpx 3	Cpx 1	Cpx 2	CpX 1	Cpx 2	Cpx 3	Cpx 1	Cpx 2	Cpx 1	Cpx 2	Cpx 3	Cpx 1
Oxide weight percentage																					
SiO_2	53,36	50,34	53,00	54,87	52,84	51,58	52,80	52,48	52,00	51,09	52,55	52,31	52,37	52,36	51,42	50,86	52,91	53,29	53,15	53,99	52,15
TiO_2	0,00	0,28	0,00	0,06	0,02	0,13	0,00	0,12	0,25	0,07	0,00	0,01	0,09	0,00	0,18	0,17	0,00	0,06	0,00	0,01	0,09
Al_2O_3	0,10	3,66	1,15	0,19	1,43	2,91	1,55	3,08	3,67	3,87	1,81	1,85	1,76	1,58	2,06	4,98	1,14	1,37	0,46	1,37	2,85
Cr_2O_3	0,00	0,00	0,00	0,00	0,00	0,00	0,03	0,00	0,00	0,01	0,03	0,00	0,00	0,03	0,00	0,00	0,00	0,00	0,00	0,00	0,00
FeO	6,53	5,64	3,39	1,40	3,90	4,17	3,86	4,49	4,61	4,85	4,31	4,11	6,08	6,00	5,46	5,22	5,09	4,11	4,14	4,00	4,80
MnO	0,17	0,16	0,20	0,20	0,16	0,18	0,15	0,08	0,11	0,09	0,07	0,06	0,22	0,22	0,24	0,23	0,28	0,21	0,15	0,11	0,11
MgO	14,22	13,99	15,41	17,17	15,59	14,35	15,16	14,71	14,36	14,01	14,89	14,71	13,75	14,00	14,52	13,31	14,86	15,02	15,83	15,20	14,41
CaO	25,46	25,25	25,56	26,01	25,73	25,43	25,27	25,43	25,44	25,41	25,57	25,61	25,44	25,45	25,71	25,14	25,60	25,72	26,09	25,82	25,66
Na_2O	0,06	0,32	0,11	0,06	0,19	0,22	0,20	0,20	0,19	0,20	0,19	0,16	0,15	0,09	0,13	0,15	0,12	0,16	0,09	0,17	0,18
K_2O	0,00	0,01	0,00	0,00	0,00	0,00	0,00	0,01	0,05	0,00	0,00	0,00	0,01	0,00	0,01	0,00	0,00	0,00	0,00	0,00	0,00
Totals	99,91	99,65	98,82	99,96	99,87	98,97	99,02	100,60	100,68	99,60	99,42	98,83	99,87	99,73	99,72	100,06	100,00	99,94	99,91	100,67	100,24
Formula																					
Si	1,988	1,860	1,964	1,994	1,937	1,914	1,960	1,916	1,900	1,897	1,949	1,943	1,943	1,952	1,901	1,875	1,949	1,959	1,950	1,969	1,914
Al	0,000	0,069	0,021	0,002	0,024	0,056	0,027	0,059	0,072	0,078	0,033	0,035	0,033	0,031	0,041	0,103	0,021	0,024	0,007	0,024	0,056
Sum Tet	1,988	1,929	1,985	1,996	1,961	1,969	1,987	1,975	1,972	1,975	1,982	1,978	1,976	1,983	1,942	1,978	1,970	1,983	1,957	1,992	1,969
Ti	0,000	0,008	0,000	0,002	0,001	0,004	0,000	0,003	0,007	0,002	0,000	0,000	0,003	0,000	0,005	0,005	0,000	0,002	0,000	0,000	0,002
Al	0,004	0,092	0,029	0,006	0,038	0,072	0,041	0,073	0,086	0,092	0,046	0,047	0,044	0,038	0,049	0,114	0,029	0,035	0,013	0,036	0,068
Cr	0,000	0,000	0,000	0,000	0,000	0,000	0,000	0,000	0,000	0,000	0,000	0,000	0,000	0,000	0,000	0,000	0,000	0,000	0,000	0,000	0,000
Fe^{+2}	0,203	0,047	0,075	0,038	0,043	0,076	0,120	0,093	0,098	0,151	0,134	0,084	0,145	0,187	0,061	0,127	0,097	0,096	0,041	0,107	0,091
Mn	0,005	0,005	0,006	0,006	0,005	0,006	0,005	0,002	0,004	0,003	0,002	0,002	0,007	0,007	0,007	0,007	0,009	0,007	0,005	0,003	0,003
Mg	0,790	0,771	0,851	0,930	0,852	0,794	0,839	0,800	0,782	0,776	0,823	0,815	0,760	0,778	0,800	0,732	0,816	0,823	0,866	0,826	0,788
Sum M1	1,003	0,922	0,962	0,982	0,938	0,951	1,005	0,973	0,977	1,023	1,005	0,948	0,960	1,010	0,923	0,984	0,951	0,963	0,925	0,972	0,952
Ca	1,016	1,000	1,015	1,013	1,010	1,011	1,005	0,994	0,996	1,011	1,016	1,019	1,011	1,016	1,018	0,993	1,011	1,013	1,026	1,009	1,009
Na	0,004	0,023	0,008	0,004	0,014	0,016	0,014	0,014	0,014	0,014	0,013	0,012	0,011	0,007	0,009	0,011	0,008	0,011	0,006	0,012	0,012
Sum M2	1,021	1,022	1,023	1,017	1,024	1,026	1,020	1,009	1,009	1,025	1,029	1,031	1,022	1,023	1,028	1,004	1,019	1,024	1,032	1,020	1,021
Endmembers (%)																					
Di	78,8	83,6	88,5	94,7	90,8	83,5	83,5	82,2	80,0	75,9	81,9	86,0	79,2	77,0	86,7	74,4	85,0	85,5	93,6	85,0	82,8
Hd	20,2	5,1	7,8	3,9	4,6	8,0	11,9	9,6	10,0	14,8	13,3	8,9	15,1	18,5	6,6	12,9	10,2	10,0	4,4	11,0	9,6
Jo	0,5	0,5	0,6	0,6	0,5	0,6	0,5	0,2	0,4	0,3	0,2	0,2	0,7	0,7	0,8	0,7	0,9	0,7	0,5	0,3	0,3
Jd	0,4	2,5	0,8	0,4	1,5	1,7	1,4	1,4	1,4	1,4	1,3	1,3	1,1	0,7	1,0	1,1	0,8	1,1	0,6	1,2	1,3
Ca-Ts	0,0	7,5	2,2	0,2	2,6	5,9	2,7	6,1	7,4	7,6	3,3	3,7	3,4	3,1	4,4	10,5	2,2	2,5	0,8	2,5	5,9
Remainder	0,1	0,8	0,1	0,2	0,0	0,3	0,0	0,5	0,8	0,0	0,0	0,0	0,5	0,0	0,5	0,4	0,9	0,2	0,1	0,0	0,1
Total	100,0	100,0	100,0	100,0	100,0	100,0	100,0	100,0	100,0	100,0	100,0	100,1	100,0	100,0	100,0	100,0	100,0	100,0	100,0	100,0	100,0
W-En-Fs system																					
Wo	50,6	51,4	51,5	51,0	51,0	52,3	51,2	51,5	51,9	52,2	51,5	52,0	51,6	51,3	51,2	52,7	50,9	51,6	50,8	51,5	51,9
En	39,3	39,6	43,2	46,9	43,0	41,0	42,7	41,4	40,8	40,0	41,7	41,5	38,8	39,2	40,3	38,8	41,1	41,9	42,9	42,2	40,5
Fs	10,1	9,0	5,3	2,1	6,0	6,7	6,1	7,1	7,3	7,8	6,8	6,5	9,6	9,5	8,5	8,5	7,9	6,4	6,3	6,2	7,6
Total	100,0	100,0	100,0	100,0	100,0	100,0	100,0	100,0	100,0	100,0	100,0	100,0	100,0	100,0	100,0	100,0	100,0	100,0	100,0	100,0	100,0

Table 11: Representative analyses of clinopyroxene from line scans

| Sample	Na 216		Na 216		Na 206		Na 210		Na 210	
	Cpx 1		Cpx 2		Cpx 1		Cpx 1		Cpx 2	
comment	Line 1		Line 2		Line 1		Line 1		Line 2	
	core	rim	core	rim	core	rim	core	rim	core	rim
major oxides weight percentage										
SiO$_2$	50,63	53,45	50,81	53,63	51,12	53,58	50,79	52,23	50,68	51,73
TiO$_2$	0,25	0,03	0,16	0,02	0,22	0,03	0,22	0,12	0,05	0,11
Al$_2$O$_3$	4,32	1,45	4,28	1,57	3,59	0,70	3,05	1,63	3,07	2,10
Cr$_2$O$_3$	0,01	0,00	0,01	0,00	0,00	0,00	0,00	0,02	0,00	0,01
FeO	4,98	4,04	4,98	3,89	4,14	4,39	6,08	5,87	6,14	5,49
MnO	0,16	0,10	0,12	0,14	0,18	0,21	0,22	0,27	0,18	0,20
MgO	13,48	15,30	13,43	15,21	14,36	15,22	13,23	13,72	13,95	13,82
CaO	25,11	25,56	24,94	25,56	25,31	25,38	25,36	25,41	25,34	25,56
Na$_2$O	0,3	0,17	0,31	0,17	0,31	0,25	0,17	0,13	0,14	0,13
K$_2$O	0,02	0,00	0,01	0,01	0,00	0,00	0,00	0,00	0,00	0,00
Totals	99,24	100,09	99,05	100,19	99,23	99,75	99,11	99,39	99,55	99,15
Formula										
Si	1,888	1,958	1,897	1,963	1,889	1,973	1,898	1,947	1,880	1,929
Al	0,084	0,026	0,083	0,028	0,067	0,006	0,061	0,031	0,062	0,042
Tet Sum	1,972	1,984	1,980	1,991	1,956	1,979	1,959	1,978	1,942	1,970
Ti	0,007	0,001	0,004	0,001	0,006	0,001	0,006	0,003	0,001	0,003
Al	0,106	0,038	0,105	0,040	0,089	0,024	0,073	0,040	0,072	0,051
Cr	0,000	0,000	0,000	0,000	0,000	0,000	0,000	0,000	0,000	0,000
Fe^{+2}	0,155	0,093	0,155	0,103	0,052	0,095	0,121	0,146	0,077	0,118
Mn	0,005	0,003	0,004	0,004	0,006	0,006	0,007	0,009	0,006	0,006
Mg	0,749	0,836	0,747	0,830	0,791	0,835	0,737	0,762	0,771	0,768
Sum M1	1,023	0,970	1,017	0,977	0,945	0,961	0,944	0,961	0,928	0,946
Ca	1,003	1,003	0,997	1,003	1,002	1,001	1,015	1,015	1,007	1,021
Na	0,022	0,012	0,022	0,012	0,022	0,018	0,012	0,009	0,010	0,009
Sum M2	1,025	1,015	1,020	1,015	1,024	1,019	1,027	1,024	1,017	1,030
Endmembers										
Di	73,2	86,2	73,5	85	83,7	86,9	78,1	79,3	83,1	81,2
Hd	15,2	9,6	15,2	10,5	5,5	9,9	12,8	15,2	8,3	12,5
Jo	0,5	0,3	0,4	0,4	0,6	0,6	0,7	0,9	0,6	0,6
Jd	2,2	1,2	2,2	1,2	2,3	1,9	1,3	0,9	1,1	1,0
Ca-Ts	8,2	2,7	8,2	2,9	7,1	0,6	6,5	3,2	6,7	4,4
Remainder	0,7	0,0	0,5	0,0	0,8	0,1	0,6	0,5	0,2	0,3
Total	100,0	100,0	100,0	100,0	100,0	100,0	100,0	100,0	100,0	100,0
Wo-En-Fs system										
Wo	52,6	51,1	52,5	51,4	52,2	50,8	52,3	51,8	51,1	52,1
En	39,3	42,6	39,3	42,5	41,2	42,4	37,9	38,9	39,2	39,2
Fs	8,1	6,3	8,2	6,1	6,7	6,9	9,8	9,3	9,7	8,7
Total	100,0	100,0	100,0	100,0	100,0	100,0	100,0	100,0	100,0	100,0
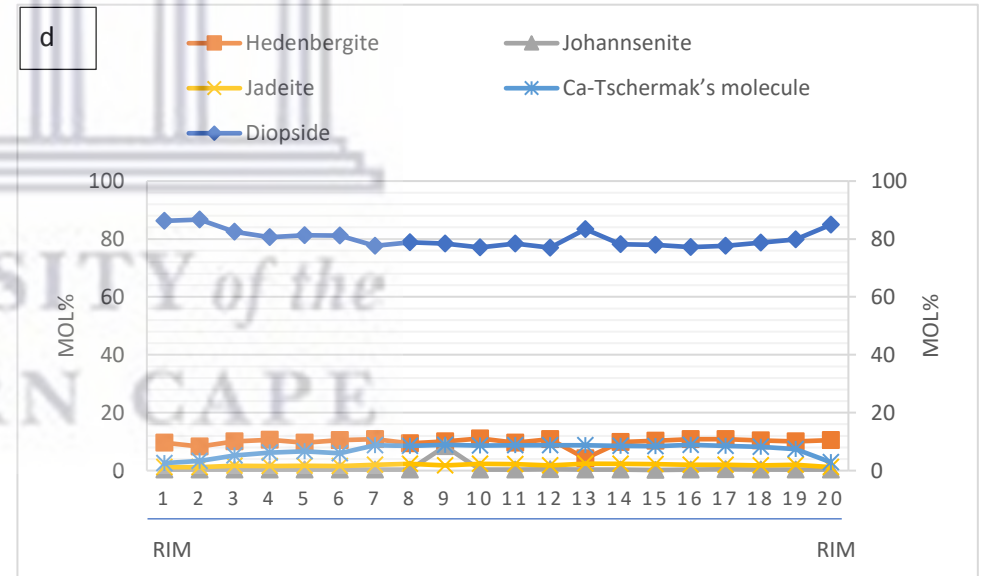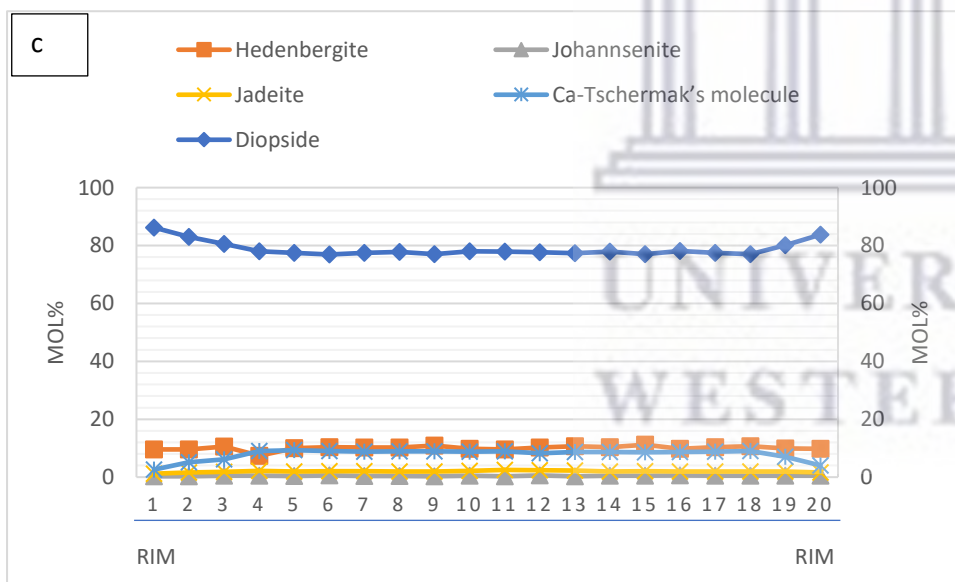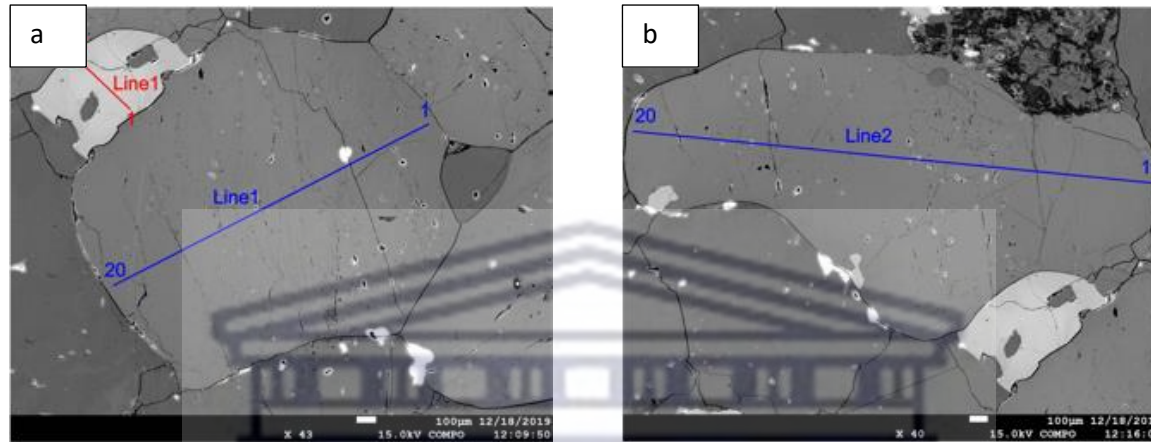
Figure 32: BSE images and compositional profiles of clinopyroxene (Sample Na 216). (a-b) BSE images showing textural features of zoned clinopyroxene represented by medium grey colour (scale bar=100 microns). The blue lines indicate line locations for microprobe analysis of clinopyroxene and nearby numbers indicate beginning and end of line. Red lines indicate microprobe analysis for garnet represented by light grey minerals. (c) Compositional profile of clinopyroxene from rim to rim representing line 1. (d) Compositional profile of clinopyroxene from rim to rim, representing line 2.

58
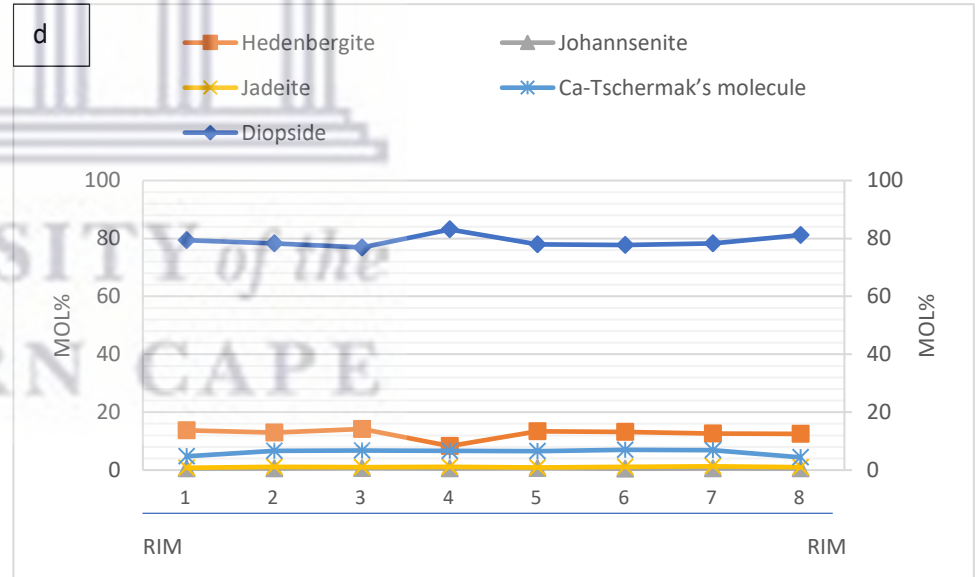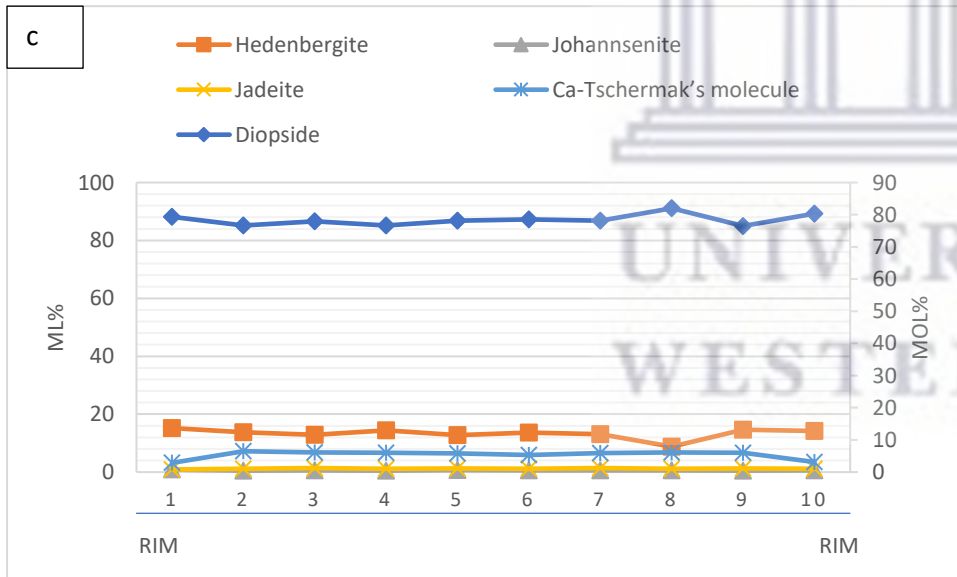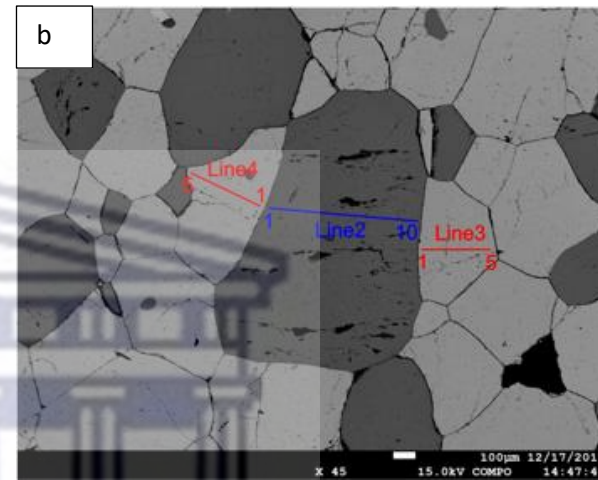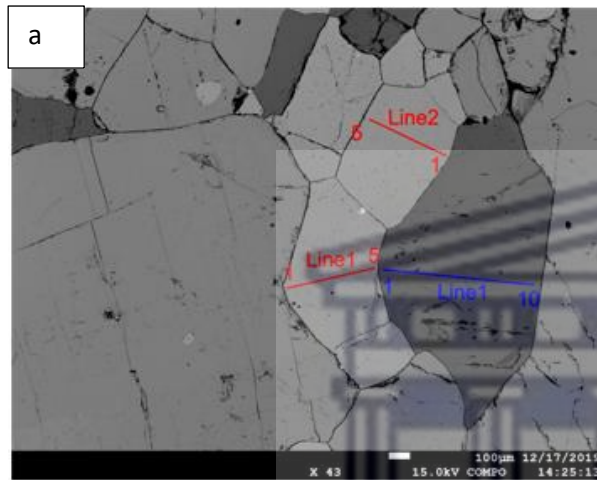
Figure 33: BSE images and compositional profiles of clinopyroxene (Sample Na 210). (a-b) BSE images showing textural features of clinopyroxene represented by dark grey colour (scale bar=100 microns). The blue lines indicate line locations for microprobe analysis of clinopyroxene and nearby numbers indicate beginning and end of line. Red line indicates microprobe analysis for garnet represented by light grey mineral. (c) Compositional profile of clinopyroxene from rim to rim representing line 1. (d) Compositional profile of clinopyroxene from rim to rim, representing line 2.
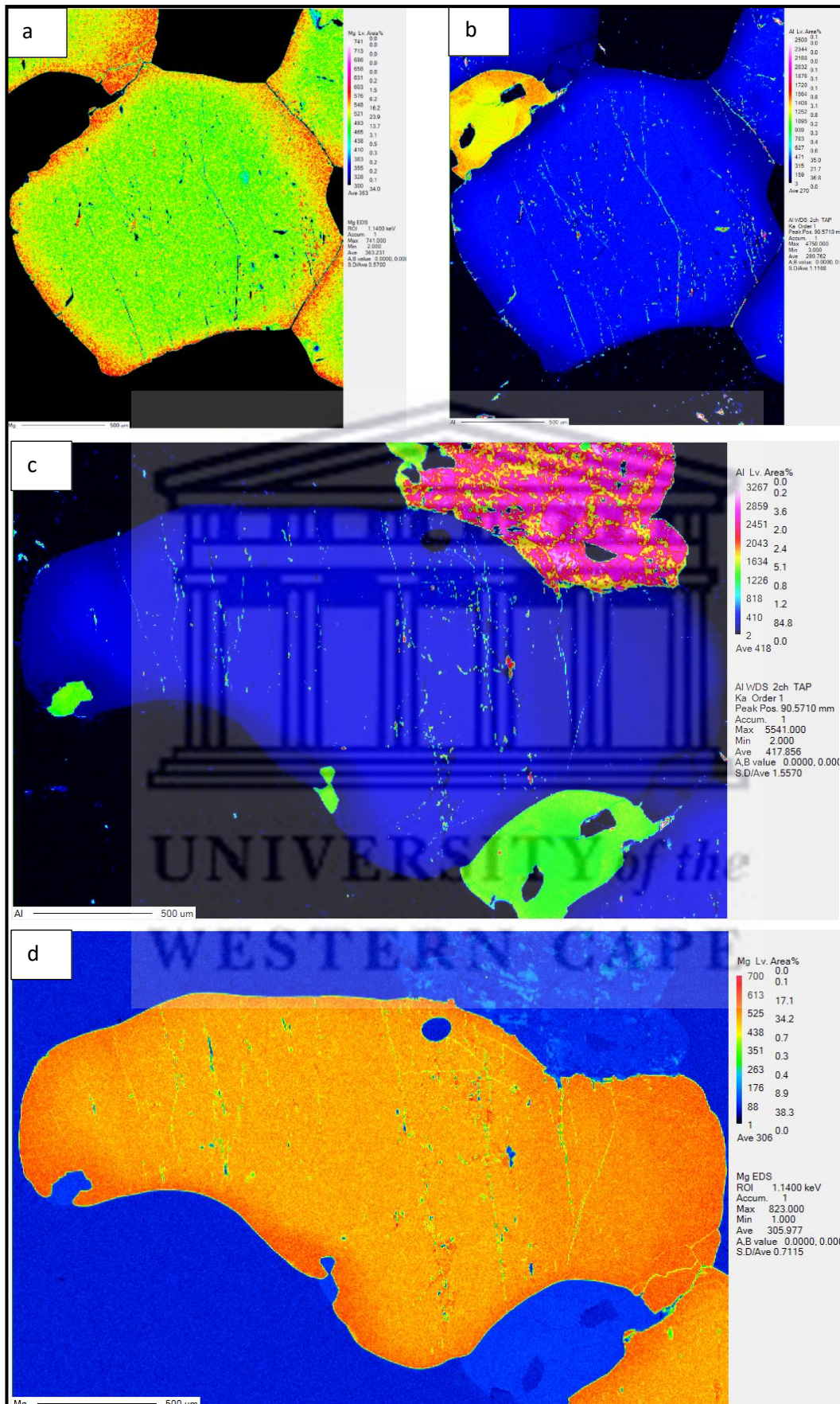
Figure 34: Element distribution maps of (a) Mg (b) Al (c) Al (d) Mg in zoned clinopyroxene. Notice narrow Mg-rich rim and wide Al-rich core.

3.3.4. Wollastonite

Wollastonite is typically a relatively pure Ca-Si phase. Wollastonite point analyses are given in Table 11. The wollastonite component ranges from 99.4-99.8 mol% while a minute enstatite and ferrosilite component has been calculated to a range of 0.0-0.2 mol% and 0.2-0.4 mol% respectively using a simple wollastonite (Ca) – enstatite (Mg) – ferrosilite (Fe) composition system.

Table 12: Representative point analyses of wollastonite

Sample	Na 221	Na 200	Na 203	Na 206	Na 209	Na 210			Na 213		Na 221
	Wo 1	Wo 1	Wo 1	Wo 1	Wo 1	Wo 1	Wo 2	Wo 3	Wo 1	Wo 2	Wo 1
oxide weight percentage											
SiO_2	51,30	51,04	51,14	50,90	51,02	51,25	51,10	51,01	51,24	51,06	51,40
TiO_2	0,02	0,05	0,00	0,03	0,03	0,00	0,04	0,10	0,00	0,04	0,02
Al_2O_3	0,00	0,11	0,00	0,03	0,06	0,01	0,02	0,01	0,00	0,00	0,00
Cr_2O_3	0,01	0,00	0,00	0,00	0,00	0,00	0,00	0,00	0,00	0,00	0,01
FeO	0,13	0,13	0,17	0,17	0,15	0,24	0,24	0,24	0,19	0,23	0,12
MnO	0,08	0,16	0,07	0,05	0,11	0,15	0,18	0,12	0,12	0,15	0,06
MgO	0,03	0,04	0,04	0,05	0,06	0,06	0,09	0,07	0,06	0,06	0,02
CaO	48,97	48,36	48,84	48,73	48,96	48,57	48,41	48,44	48,88	48,48	49,00
Na_2O	0,00	0,01	0,00	0,02	0,01	0,00	0,01	0,02	0,00	0,00	0,00
K_2O	0,00	0,08	0,00	0,01	0,00	0,00	0,00	0,00	0,00	0,00	0,00
Totals	100,54	99,98	100,26	99,98	100,40	100,29	100,09	100,00	100,49	100,02	100,63
Formula											
Si	1,973	1,974	1,972	1,968	1,964	1,976	1,974	1,973	1,971	1,974	1,975
Al	0,000	0,005	0,000	0,002	0,003	0,001	0,001	0,001	0,000	0,000	0,000
Al	0,000	0,000	0,000	0,000	0,000	0,000	0,000	0,000	0,000	0,000	0,000
Ti	0,001	0,001	0,000	0,001	0,001	0,000	0,001	0,003	0,000	0,001	0,001
Cr	0,000	0,000	0,000	0,000	0,000	0,000	0,000	0,000	0,000	0,000	0,000
Fe^{+3}	0,004	0,004	0,005	0,005	0,005	0,008	0,008	0,008	0,006	0,007	0,004
Mn	0,003	0,005	0,002	0,001	0,004	0,005	0,006	0,004	0,004	0,005	0,002
Mg	0,002	0,002	0,002	0,003	0,003	0,003	0,005	0,004	0,003	0,004	0,001
Ca	2,018	2,003	2,018	2,018	2,020	2,007	2,004	2,007	2,015	2,009	2,017
Na	0,000	0,001	0,000	0,001	0,001	0,000	0,001	0,001	0,000	0,000	0,000
K	0,000	0,004	0,000	0,000	0,000	0,000	0,000	0,000	0,000	0,000	0,000
Endmembers											
Wo	99,7	99,7	99,6	99,6	99,6	99,4	99,4	99,4	99,5	99,5	99,8
En	0,1	0,1	0,1	0,1	0,2	0,2	0,2	0,2	0,2	0,2	0,0
Fs	0,2	0,2	0,3	0,3	0,2	0,4	0,4	0,4	0,3	0,4	0,2
Total	100,0	100,0	100,0	100,0	100,0	100,0	100,0	100,0	100,0	100,0	100,0

Chapter 4: Discussion

Devolatilisation reactions are generally sensitive to fluid composition. Where carbonates and graphite are absent, fluids tend to be essentially hydrous. However, mixed silicate-carbonate equilibria tend to produce mixed volatiles (H_2O-CO_2 fluids), which adds an extra controlling parameter, apart from rock composition, pressure and temperature. Determining pressure, temperature and fluid composition simultaneously is commonly not possible from a calc-silicate rock, unless there is an invariant equilibrium. However, that itself is difficult to verify if the system is chemically complex, with both prograde and retrograde phases potentially involved, or if metamorphism is polycyclic. As fluid compositions are commonly indirectly derived (as opposed to mineral compositions), it is best to establish either P or T, or both, from close by domains near both study areas where thermobarometric data are already available. This way, fluid composition can be more easily constrained.

4.1 Kliprand calc-silicate pod

For the Kliprand area, peak metamorphic conditions had been determined from the abundant metapelitic gneisses. According to Albat (1984); Waters (1986, 1989); (Baars, 1990) and Nowicki et al. (1995), the rocks of the 3018 Loeriesfontein mapped area (Macey et al., 2011) fall within an upper granulite-facies subzone and experienced peak metamorphic conditions of ~750–870 °C and 4.5–6 kbars. Osumilite, which occurs in metapelites near the southern edge of the Loeriesfontein mapped area, indicates peak metamorphic temperatures in the Bushmanland Domain as high as 870 °C (Waters, 1989; Nowicki et al., 1995).

The peak-metamorphic assemblage for the studied calc-silicate pod is Scp + Di + Wo + Qz ± Plg ± Kfs ± Cal ± Ttn ± Opq. With diopside being the only ferro-magnesian phase at peak conditions, the chemical system for discussing the peak assemblage can be simplified to include Scp, Wo, Qz, Cal and Plg, as a first approach. The reactions delimiting diopside stability are well outside the P-T range considered here. At conditions of 5 kbar, diopside is stable in the presence of calcite or quartz (not both once the wollastonite-forming reaction has been crossed) from about 600 to well over 900°C (Spear, 1995). A further simplification can be applied by ignoring Na in Plg and Scp. Calc-silicate rocks commonly contain An-rich plagioclase, and there is a simple H_2O-CO_2-independent reaction connecting albite to marialite:

Albite + NaCl ⇌ Marialite (21)

To discuss the peak equilibria in this simplified framework, an isobaric T-X_{CO_2} reaction diagram will be used (Fig. 35). The pressure of 5 kbar is appropriate for the Kliprand area. The assemblages would be much less sensitive to minor P variations than they are to temperature and fluid composition.

For convenience, the reactions as described in the text correspond to the numbers of reactions listed in Fig. 36. Therefore, any reactions listed in Fig. 35 that are not listed in Fig. 36 will receive a number following the last reaction listed in Fig. 36. Since the reactions listed in Fig. 36 are not all used in this study, the numerical order for the reactions as they appear in the text will not be in a continuous order. Reaction 21 above has been given the last number in the reactions listed since it does not form part of any reactions listed in Fig. 35 and Fig. 36.

Wollastonite is commonly produced by the prograde reaction;

Calcite + Quartz ⇌ Wollastonite + CO₂ (5) (Hiroi et al., 1987; Motoyoshi et aI., 1991; Harley and Buick, 1992; Hoeffbauer and Spiering, 1994; Satish-Kumar et al., 1995),

forming one of the most important reactions in this calc-silicate assemblage. The formation of wollastonite is favoured by high temperatures and low X_{CO_2} conditions as shown by the positive slope of the reaction curve in T-X_{CO_2} space (Fig. 35). The presence of wollastonite in association with scapolite and quartz requires a minimum X_{CO_2} of 0.5, but some wollastonite may have formed earlier, at lower temperature and lower X_{CO_2}. Under reaction-buffered conditions, wollastonite would have formed from calcite and quartz over a T interval as the assemblage moves along the wollastonite-forming reaction. According to Fig. 35, wollastonite is stable under high X_{CO_2} conditions only at high-temperatures of > 800 °C if scapolite is present, which is in accordance with the prevailing low-P, high-T granulite facies metamorphism in the Bushmanland Domain. The Scp-Wo-Qz stability field at high X_{CO_2} indicates that the system was essentially internally buffered at peak conditions by one of the two reactions enclosing that P-T field (reactions 5 and 20). Evidently, no externally derived H_2O was infiltrating. The complete absence of garnet further supports the notion that the fluid near peak conditions could not have been H_2O-rich (cf. Fig. 35). All the assemblages on the H_2O-rich side involve grossular, while no garnet has been observed in the studied calc-

silicate rocks. This means, that the equilibria involved X_{CO2} rich conditions ($X_{CO2} > 0.5$) at temperatures of 800-870 °C.
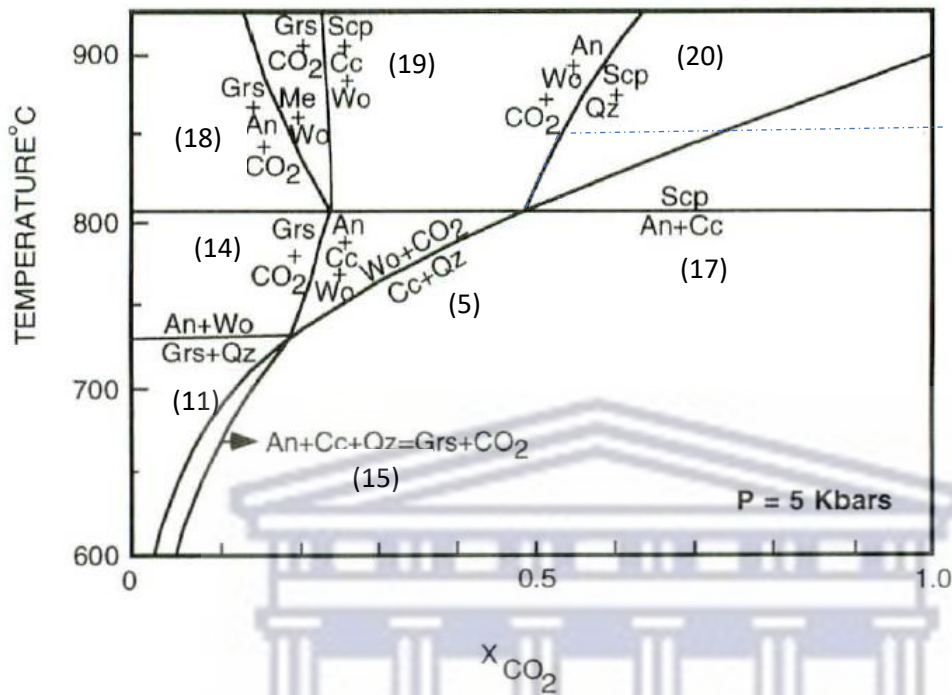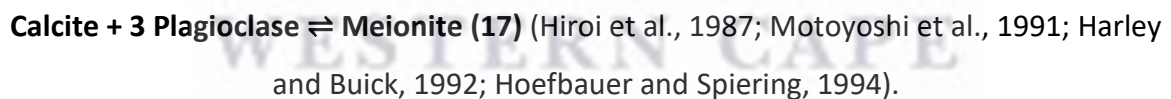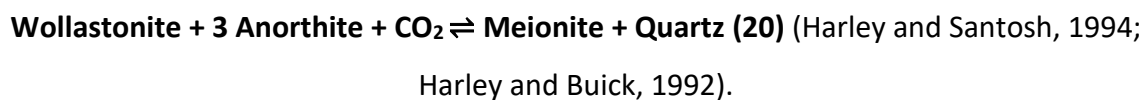

Figure 35: X_{CO2} diagram showing the relevant reaction curves in the system CaO-Al$_2$O-SiO$_2$-CO$_2$-H$_2$O at 5 kbars (modified after Moecher and Essene, 1990).

Using the Ca-endmember of scapolite (meionite), it is evident that scapolite (from scapolite-diopside-rich layers) most probably formed through the solid-solid reaction;

Calcite + 3 Plagioclase ⇌ Meionite (17) (Hiroi et al., 1987; Motoyoshi et al., 1991; Harley and Buick, 1992; Hoefbauer and Spiering, 1994).

Layers that are predominantly comprised of scapolite + quartz may indicate the formation of scapolite through the reaction:

Wollastonite + 3 Anorthite + CO$_2$ ⇌ Meionite + Quartz (20) (Harley and Santosh, 1994; Harley and Buick, 1992).

The absence of grossular in the analysed sections suggests that the formation of meionite did not result from the breakdown of grossular. Reaction 17 is independent of fluid infiltration and is completely temperature controlled at constant pressure (Satish-Kumar et al., 1995) while reaction 20, is dependent on fluid composition. To proceed to the right-hand side, CO$_2$

64

infiltration is required. A potential source may be very wollastonite-rich layers that formed from a simple calcite + quartz breakdown reaction. Scapolite initially formed through the breakdown of plagioclase and calcite (reaction 17). This reaction is also supported by the absence of plagioclase + calcite in scapolite-rich layers, which could be indicative of plagioclase and calcite being consumed. Scapolite is still found to be in equilibrium with plagioclase, suggesting that not all the plagioclase was consumed when peak metamorphic temperatures were reached. Plagioclase remained in excess, while calcite was used up completely.

Reaction 20 characteristically occurs in CO_2-rich environments (Harley and Santosh, 1995; Harley and Buick, 1992). It can be argued that scapolite may have formed through this reaction as temperatures increased above 800 °C, excluding all grossular forming reactions. Evidence for such prograde textural features is observed in thin sections, where wollastonite and plagioclase reacted to form scapolite. This could indicate that peak metamorphism reached the reaction curve of scapolite formation before cooling (Satish-Kumar et al., 1995). This reaction may also be supported by scapolite-quartz symplectites (Fig. 16c) and scapolite coronas between wollastonite and plagioclase.

Evidence for retrograde metamorphic reaction textures is represented by the breakdown of wollastonite to calcite + quartz and the breakdown of scapolite to calcite and plagioclase (locally minor amounts of quartz).

Scapolite-quartz symplectites are most likely a result of minor CO_2 fluid infiltration (Harley and Santosh, 1994). Infiltration of a CO_2-rich fluid can also be supported by retrogressive textural features such as the replacement of wollastonite by a calcite-quartz assemblage (Fig. 16d) since any isothermal increase in X_{CO2} favours the calcite-quartz assemblage. However, the possibility that any reaction in the studied calc-silicate pod may be related to the infiltration of an externally-derived CO_2-rich fluid is very unlikely, since there is no CO_2 generated in the surrounding gneisses being carbonate- and graphite- free. This suggests that the fluid in these specific calc-silicate layers was derived from reactive layers within the calc-silicate pod.

4.2. Garies wollastonite quarry

The Garies wollastonite quarry presents a structurally intricate deposit, making it challenging to ascertain the original lithological relationships and the precise metasomatic processes that extensively altered these relationships, based on the exposed features. According to Harris and Maboane (2021), due to the rarity of low- $\delta^{18}O$ rocks, especially of low- $\delta^{18}O$ carbonates in the Garies wollastonite deposit, it is most likely that the deposit represents a hydrothermal skarn, which had been subsequently subjected to regional granulite-facies metamorphism, re-equilibrating mineralogically and also isotopically.

Skarn deposits are usually formed through metasomatism in metamorphic aureoles between carbonate- and silicate rocks, commonly an intrusive rock that provides both heat (to create fluid circulation), as well as being a potential fluid source itself (such as late-magmatic fluids typically released from hot hydrous silicate intrusion such as granite). Among all the rocks observed in the area, the M1 rock group can serve as a potential candidate for providing the necessary heat and to initiate fluid access to cause metasomatism. The M1 rock group was identified as microcline-garnet-hornblende-rich metamorphic rocks which surrounded the main deposit and also smaller calc-silicate outcrops further away from the quarry. Due to the regional-metamorphic overprint and deformation, it is difficult to determine what the protolith of the source rock was before metamorphism. Because of the high content of feldspar, it may be possible that the original rock was some kind of granitoid. The fluids are externally derived, hydrous, and therefore did not originate in the carbonates. Since skarn formation occurred before the peak metamorphism, it's likely that the igneous rock intruded a stratigraphic sequence that still contained significant amounts of water. As a result, the intrusion would have initiated fluid circulation, leading to intensive fluid-rock interactions with high fluid-to-rock ratios.

Phases analysed with the electron microprobe include wollastonite, vesuvianite, garnet and clinopyroxene. Wollastonite is a relatively pure Ca-Si phase. The dominant clinopyroxene endmembers include diopside (Di) with a range of 74.4-94.7 mol% and hedenbergite (Hd) ranging from 3.9-20.2 mol%, with all other components (CaTs, Jd, Jo) being at very low concentrations. Garnet was identified as a grossular-andradite solid solution, grossular being the dominant endmember with a range between 63.2-77.5 mol%. The andradite content varies from 17.8-30.6 mol%. By examining the mineral composition of garnet, it can be

66

deduced that the prevailing type of garnets are typical calc-silicate garnets. Two types of garnets were identified which includes a group of homogeneous, isotropic and anhedral garnets, and a less common group of garnets that are more heterogeneous and birefringent, with euhedral crystal faces developed. The second group of garnets also displays distinctive zonation patterns.

At granulite-facies temperatures, garnets of moderate size - as seen in these samples - will tend to be more homogenous (excluding any late effects, like diffusional adjustment at rims or late overgrowths). Usually, garnets tend to grow as zoned crystals, with the zoning reflecting any changes in P, T, effective bulk composition, as well as fluid composition (e.g., Spear, 1995). Element fractionation also occurs as the garnet grows and locks up elements inside the crystals that no longer equilibrate with the other minerals. Once temperatures become high, the chemical zoning is homogenised over the entire garnet, which means that the garnets lose their growth record and re-equilibrate with all other minerals. A garnet growth-forming profile will only be preserved if the duration of the high-temperature peak is short. However, this is not very likely at granulite-facies regional metamorphism.

Looking at the less common, zoned, euhedral garnets in this study, their core composition is very similar to the composition of the homogenous garnets, while their outer zones are not. Therefore, the evidence points towards these outer zones relating to a post-peak event. The lack of homogenisation also points to lower-temperature conditions. That implies, the skarn-forming event and subsequent regional metamorphism cannot be clearly differentiated within the peak equilibrium assemblages. The post-peak birefringent garnets, however, grew at lower T, on the cooling paths.

Most of the clinopyroxenes in this study show chemical zoning at the outer rim. Unlike garnet, pyroxenes homogenise more readily at high temperatures, and an outer rim may represent either a last segment of growth at peak conditions or more likely, a late diffusive adjustment during cooling and/or decompression.

Garnet coexists with clinopyroxene in most skarn deposits (Rose and Burt, 1979). Baghban et al. (2015) suggest that if there is no presence of replacement textures between garnet and clinopyroxene, especially where clinopyroxenes have low concentrations of TiO_2, MnO, and Cr_2O_3, high Ca values in both garnet and clinopyroxene, as observed in the minerals analysed

in this study. It indicates simultaneous growth of these two minerals. This suggests that fO_2 was moderate and temperature was relatively high (Burt, 1972).

A wide variety of mineral assemblages are present in the studied calc-silicate rocks of the Garies deposit. Based on field evidence and petrographic studies, the reaction textures and structural features that were observed preserve a high-temperature metamorphic imprint, with all the original sedimentary sequences and earlier formed mineral assemblages being strongly overprinted. Four calc-silicate assemblages (CS1, CS2, CS3, and CS4) are characterised by their distinctive mineralogical components. Among the four groups, CS1 is most suitable to estimate peak metamorphic conditions.

For the gneisses of the Garies area, peak metamorphic conditions had been determined in previous literature by Seto et al. (2006) and Macey et al. (2011), where P-T estimates for this area, varied at 800-860 °C and 4-6 kbar. These data will be used here to constrain fluid present at peak P-T. The peak metamorphic assemblage for the studied wollastonite calc-silicates is **Cal + Wo + Di + Grt +Ves ± Ttn ± Ep.**

The chemical system for discussing the peak assemblage can be simplified to include Grt, Ves, Wo, Cal and Di. To discuss the peak equilibria in this simplified framework, a petrographic grid which shows the P-T topology for the CMASV (Calc-alkaline, Metaluminous, Silicic, Volcanic) system calculated at different X_{CO_2} conditions was used (Fig. 36 a-e).

Topological analysis done by Valley et al. (1985) indicated that vesuvianite-bearing assemblages will limit the P-T-X (CO_2-H_2O) conditions for the formation of many calc-silicate assemblages. As can be seen in Fig. 36, the vesuvianite stability field is strongly dependent on fluid composition at any given range of P and T (Dey et al., 2019). According to Valley et al. (1985) vesuvianite, in the presence of garnet and wollastonite, is restricted to very high X_{H_2O}, low X_{CO_2} conditions as well as high-temperature conditions in the absence of quartz.

Fig. 36 illustrates that the stability field of vesuvianite is limited to the high T-side of reaction 16;

Calcite + Diopside + Anorthite + Grossular + H_2O ⇌ Vesuvianite + CO_2 (16) (Valley et al., 1985).
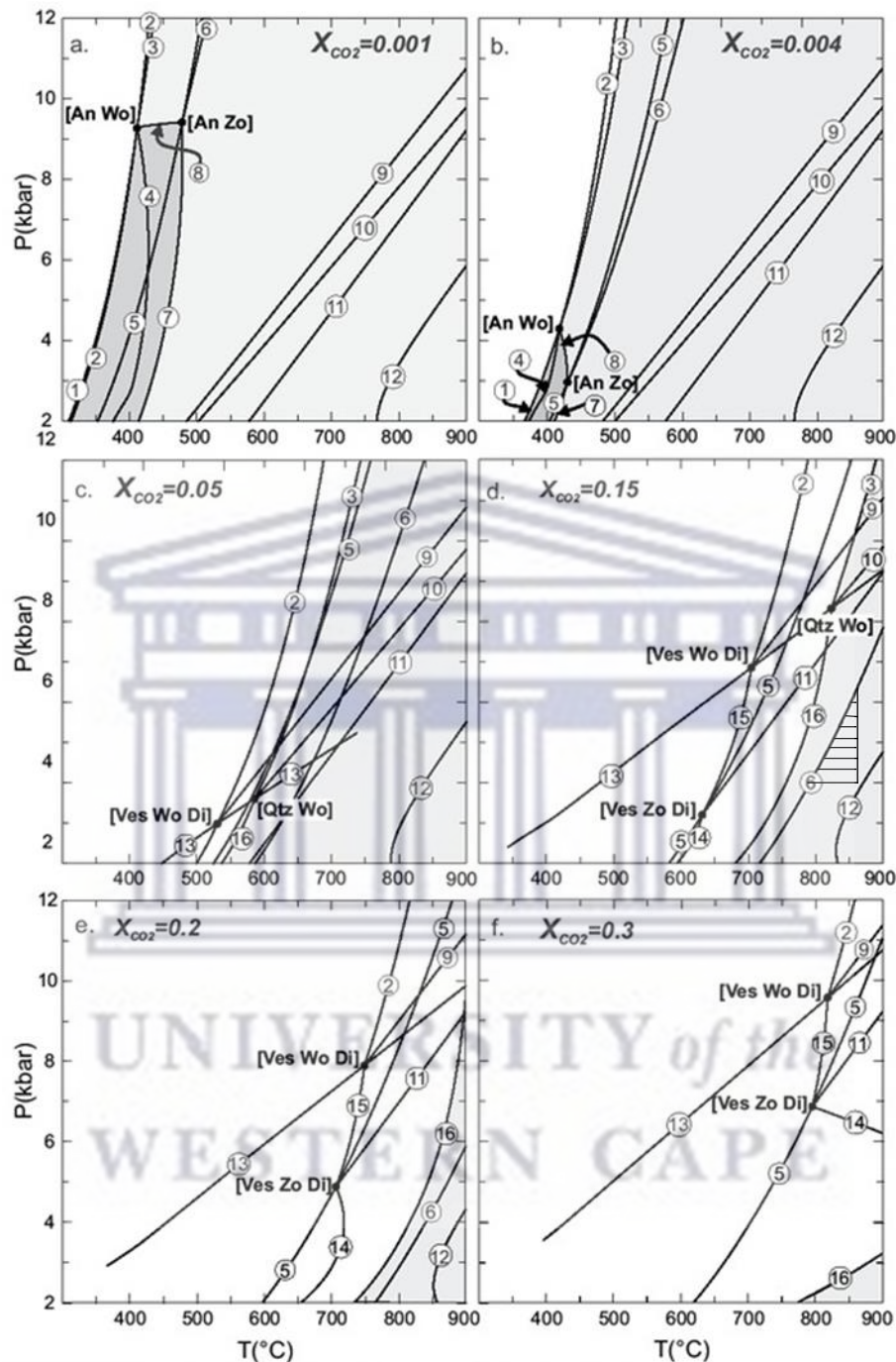
Figure 36: (a–f) P-T topology of the CMASV system calculated at different X_{CO2} conditions. The reaction numbers are consistent throughout the figures a–f. The lighter shaded region represents the stability fields of vesuvianite while the darker shaded region represents the stability field of vesuvianite-quartz assemblage. Reaction band represent the stability field of the Garies rock at the chosen P-T conditions. Reaction equations are written with the high-T assemblage to the right of the = sign (a reaction that has changing slopes with X_{CO2}, is named following the slope of its first appearance) (Dey et al., 2019).

1. Cal Di Zo Qtz = Ves
2. Cal Zo Qtz = Grs
3. Cal Di Zo Grs = Ves
4. Zo Qtz Ves = Di Grs
5. Cal Qtz = Wo
6. Cal Di Grs = Ves Wo
7. Ves Qtz = Di Wo Grs
8. Di Cal Grs= Qtz Ves
9. Qtz Zo = An Grs
10. Di Grs Zo = An Ves
11. Grs Qtz = An Wo
12. Di Grs = An Ves Wo
13. Zo = Cal An
14. Cal Wo An = Grs
15. Cal Qtz An = Grs
16. Cal Di An Grs = Ves

69

Since anorthite is absent from the CS1 rocks, it is evident that reaction 16 reached completion, and the stability field for the Garies rocks is restricted to the high-T side of reaction 16. Reaction 6,

Calcite + Diopside + Grossular + H_2O ⇌ Wollastonite + Vesuvianite + CO_2 (6) (Valley et al., 1985).
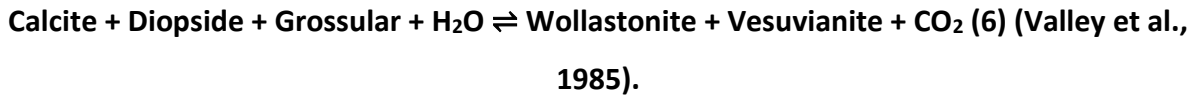
restricts the stability field of the calc-silicate equilibria to even higher temperatures. Since all the phases involved in reaction 6 are coexisting, this reaction is representative of the peak P-T-X conditions. In the endmember CMAS system presented in Fig. 36, the reaction is univariant at fixed X_{fluid}. However, as the real compositions of the mafic phases at Garies involve Fe, reaction 6 becomes continuous in the CMFAS system, and thus forms a reaction band in the P-T diagrams of Fig. 36. The peak conditions of the Garies calc-silicates lie within this band. Importantly, the independently derived P-T conditions for the wall rocks, if plotted within Fig. 36, impose tight limits on fluid compositions. At $X_{CO2} > 0.2$, vesuvianite is no longer stable within the chosen P-T field (4-6 kbar; 800-860 °C). Thus, the stability field is limited to H_2O- rich conditions at $0.2 < X_{CO2} > 0.15$.

Although the presence of wollastonite in association with vesuvianite and grossular requires hydrous fluid compositions at peak conditions, some wollastonite may have formed earlier at lower temperatures and pressure conditions through the reaction;

Calcite + Quartz ⇌ Wollastonite + CO_2 (5)

This reaction is also observed in reverse, as a partial retrogression of wollastonite along its grain boundaries, typically being replaced by a quartz-calcite assemblage (Fig. 19 b-c). This retrograde reaction of wollastonite is indicative of cooling or increasing in X_{CO2}, therefore favouring the stability of quartz-calcite assemblage. Since the extent of this retrograde reaction is only minor, it could be due to a minimal local build-up of CO_2 and poor permeability of the contact rocks (Waters, 198) for a short period. As illustrated by Fig. 36, an increase in X_{CO2} will shift the reaction curve to higher temperatures and pressures; hence, the formation of wollastonite will occur in lower X_{CO2} conditions only. It can thus be assumed that CO_2 created by reaction 5 had escaped to a large extent. Taking into consideration that garnet-

forming reactions are high-temperature decarbonisation reactions, it is assumed that the calc-silicate rocks acted as local CO_2 sources at peak metamorphism.

The stability field at low X_{CO2} conditions indicates that the system was essentially externally buffered at peak conditions. Evidently, externally derived H_2O was infiltrating the system from the surrounding rocks. Since not much H_2O is released within the rocks, the H_2O must have been derived externally.

The presence of quartz associated with the calc-silicate minerals seen in CS4 samples of garnet and vesuvianite, suggests that silica had been introduced by externally derived volatiles. In the analysed sections, there is no quartz in the rock matrix, but is restricted to small pockets in association with the euhedral birefringent garnets, displaying their crystal faces against the quartz. (Fig. 23; Fig. 24 a-b). This suggests that the quartz must have come in as a late-stage growth in originally fluid-filled micro-pockets.

The formation of reaction textures, such as garnet rims around vesuvianite (Fig. 20 c-f), requires a rather more complex explanation. According to Dey et al. (2019), the curved non-interfering boundary between vesuvianite and garnet suggests that both were in equilibrium. This suggests that after the formation of vesuvianite, vesuvianite-garnet became the stable assemblage and the vesuvianite grains allowed passive growth of a garnet corona without being involved in the reaction (Dey et al., 2019). This may also be evidence of a retrograde reaction that never reached completion.

Complex retrograde reaction textures, such as fine-grained retrograde material forming rings in the centre of garnet grains (Fig. 24c), may be indicative of intermittent metamorphism. It can be assumed that this type of reaction texture may be indicative of an initial growth of garnet during prograde metamorphism followed by a cooling stage which caused garnet grains to be replaced by a fine-grained retrograde material at the mineral grain boundary. The growth of garnet around this fine-grained retrograde material suggests reheating in the system during a second stage of metamorphism which allowed the garnet grains to continue their growth after cooling.

4.3. Comparison of the Garies and Kliprand occurrences

Major differences between the Garies wollastonite quarry and the Kliprand calc-silicate pod include their mineralogical components. Both Garies and Kliprand have high abundances of

71

wollastonite. Garies, however, has minerals present such as vesuvianite and garnet with no presence of scapolite while vesuvianite and garnet are absent in the Kliprand pod. Kliprand calc-silicates are also abundantly rich in scapolite. Although calc-silicates from both areas are very rich in wollastonite, their fluid compositions at peak metamorphism are very different. In the Garies wollastonite deposit, the calc-silicate rocks and minerals have equilibrated under externally controlled H_2O-rich fluid conditions. This is also indicated by the presence of minerals such as vesuvianite. One of the mechanisms attributed for the H_2O enhancement is a pervasive influx of water-rich fluids from surrounding gneisses or a magmatic source. The absence of grossular from-calc silicates in the Kliprand area is indicative that the rocks and minerals equilibrated under CO_2-rich fluid conditions. Since there is no evidence for an external CO_2 source in the surrounding gneisses, it is suggested that the fluid composition during peak metamorphism was internally controlled.

5. Conclusions

Calc-silicate rocks from both study areas (Kliprand and Garies) equilibrated at granulite facies conditions. The Kliprand calc-silicate pod is dominated by scapolite, diopside, quartz, calcite, wollastonite, K-feldspar and plagioclase. The Garies calc-silicates can be divided into five rock groups (CS1, CS2, CS3 CS4 and M1). Peak assemblages include Cal + Wo + Di + Grt +Ves ± Ttn ± Ep (CS1), Grt + Di + Ves + Wo ± Fld ± Cal (CS2), Grt + Di + Ves ± Wo ± Cal ± Mc (CS3), Grt + Ves ± Di (CS4) and Mc + Grt + Hbl+ Di ± Ttn (M1). Within the quarry, wollastonite, garnet, diopside, calcite and vesuvianite are the dominant phases. Mineral analysis and stoichiometric calculations for four major phases (garnet, vesuvianite, clinopyroxene and wollastonite) from the Garies calc-silicate rocks indicate that the garnets are essentially grossular-andradite solid solutions, grossular being the dominant end-member. Two generations of garnet are identified which included a group of homogeneous, isotropic, anhedral garnets, and a less common group of late-formed garnets that display distinctive zonation patterns and are more heterogeneous and birefringent. The dominant clinopyroxene endmembers include diopside (Di) and hedenbergite (Hd), with all other components (CaTs, Jd, Jo) being at very low concentrations. Wollastonite is a relatively pure Ca-Si phase.

Estimations based on the calc-silicate equilibria and previous literature are suggestive of peak temperatures in excess of 800°C (800-870°C at 4-6 kbar; Seto et al., 2006; Macey et al., 2011)

for both areas. Extensive and multiple reworking of exposures in the Garies area led to difficulty in the deriving of original lithological relationships. From lithological evidence and a relatively recent isotope study by Harris and Maboane (2021), it is implied that the Garies calc-silicate rocks can be interpreted as a hydrothermal skarn that initially formed through water-rock interaction between the carbonate wall rock and a felsic magma, to be later overprinted by regional high-grade metamorphism. Mineral parageneses and T-X_{CO2} diagrams imply that calc-silicate rocks from the two different localities (Garies and Kliprand) had highly contrasting CO_2 activities with $0.2 < X_{CO2} > 0.15$ and $X_{CO2} > 0.5$ respectively. The mineral equilibria in the Garies area indicate that the system was essentially externally buffered at low X_{CO2} conditions, at peak metamorphic conditions. Since there was no CO_2 generated in the surrounding gneisses in the Kliprand area, the CO_2-rich fluids in these specific calc-silicate layers were derived from reactive layers within the calc-silicate pod, keeping the system internally buffered. There is no evidence for influx of externally derived hydrous fluids from the surrounding rocks and no evidence for a skarn-forming event related to an intrusion.
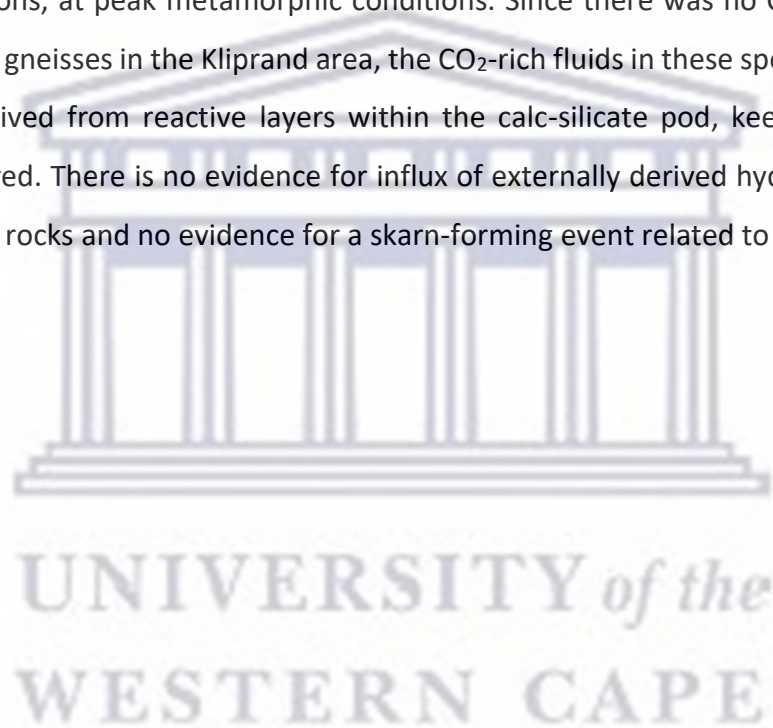
References

Agenbacht, A.L.D. (2007). The geology of the Pofadder area. 1:250 000 map sheet explanation 2918. Council for Geoscience, p. 89.

Albat, H.M. (1984). The Proterozoic granulite facies terrane around Kliprand, Namaqualand Metamorphic complex. Bull., Precambrian Research. Unit, University of Cape Town, 33, p. 386.

Andreoli, M.A.G., Andersen, N.J.B., Levin, M., Niemand, N. (1987). Geology of the Vaalputs radioactive waste disposal site in the Republic of South Africa. Explanatory notes for the geological map of the site on the scale 1:250 000, Department of Geotechnology Atomic Energy Corporation of South Africa, Limited, 39 pp.

Ashwal, L.D., Andreoli, M.A.G., Page, T., Armstrong, R.A., Tucker, R.D. (1997). Geology and geochronology of high temperature granulites, Vaalputs area, central Namaqualand, South Africa. In: Abstracts, 13th Conference of the Tectonic Division of the Geological Society of South Africa. February 1997. Johannesburg, South Africa, University of the Witwatersrand, pp. 1–3.

Baars, F.J. (1990). Geologic and Petrologic Evidence for Granulite-facies Partial Melting in the Garies-Platbakkies supra-crustal Gneiss Belt, Namaqualand Metamorphic Complex, South Africa. M.Sc. thesis (unpubl.). University of Cape Town, pp. 128.

Baghban, S., Hosseinzadeh, M.R., Moayyed, M., Mokhtari, M.A.A., Gregory, D. (2015). Geology, Mineral Chemistry and Formation Conditions of Calc-Silicate Minerals of Astamal Fe-LREE Distal Skarn Deposit, Eastern Azarbaijan Province, NW Iran. Ore Geology Reviews. 68. 79-96.

Bailie, R., Armstrong, R., Reid, D.L. (2007a). Composition and single zircon U-Pb emplacement and metamorphic ages of the Aggeneys Granite Suite, Bushmanland, South Africa. South African Journal of Geology. 110, 87–110.

Bailie, R., Armstrong, R., Reid, D.L. (2007b). The Bushmanland Group supracrustal succession, Aggeneys, Bushmanland, South Africa: Provenance, age of deposition and metamorphism. South African Journal of Geology. 110, 59–86.

Bailie, R., Gutzmer, J., Rajesh, H.M. (2010). Lithogeochemistry as a tracer of the tectonic setting, lateral integrity and mineralization of a highly metamorphosed Mesoproterozoic volcanic arc sequence on the eastern margin of the Namaqua Province, South Africa. Lithos 119, 345–362.

Bailie, R., Gutzmer, J., Rajesh, H.M., Armstrong, R. (2011). Age of ferroan A-type posttectonic granitoids of the southern part of the Keimoes Suite, Northern Cape Province, South Africa. Journal of African Earth Sciences. 60, 153–174.

Bailie, R., Rajesh, H.M., Gutzmer, J. (2012). Bimodal volcanism at the western margin of the Kaapvaal Craton in the aftermath of collisional events during the Namaqua-Natal Orogeny: The Koras Group, South Africa. Precambrian Research. 200–203, 163–183.

Bailie, R., Macey, P.H., Nethenzheni, S., Frei, D., le Roux, P. (2017). The Keimoes Suite redefined: The geochronological and geochemical characteristics of the ferroan granites of the eastern Namaqua Sector, Mesoproterozoic Namaqua-Natal Metamorphic Province, southern Africa. Journal of African Earth Sciences. 134, 737-765. http://dx.doi.org/10.1016.j.jafrearsci.2017.07.017

Bailie, R., Abrahams, G., Bokana, R., van Bever Donker, J., Frei, D., and le Roux, P. (2019). The geochemistry and geochronology of the upper granulite facies Kliprand dome: Comparison of the southern and northern parts of the Bushmanland Domain of the Namaqua Metamorphic Province, southern Africa and clues to its evolution: Precambrian Research. 330, 58-100.

Barker, A.J. (1998). Introduction to Metamorphic Textures and Microstructures, 2nd Edition. Cheltenham: Stanley Thornes (Publishers) Ltd.

Best, M.G. (2003). Igneous and Metamorphic Petrology, 2nd Edition. Malden: Blackwell Science Ltd, pp. 426.

Blignault, H.J., Van Aswegen, G., Van der Merwe, S.W., Colliston, W.P. (1983). The Namaqualand Geotraverse and environs: part of the Proterozoic mobile belt. In: Botha, B.J.V. (Ed.), Namaqualand Metamorphic Complex. Special Publication of the Geological Society of South Africa, pp. 1–29.

75

Brady, J., College, S., Perkins, D. (2022). Mineral Formulae Recalculation: Teaching Phase Equilibria. Retrieved May 9, 2021, from https://serc.carleton.edu/research_education/ equilibria/mineralformulaerecalculation.html.

Buick, I.S., Harley, S.L., Cartwright, I.C. (1993). Granulite facies metasomatism: zoned calc-silicate boudins from the Rauer Group, East Antarctica. Contributions to Mineralogy and Petrology. 113, 557-571.

Burt, D.M. (1972). Mineralogy and geochemistry of Ca–Fe–Si skarn deposits. Unpublished PhD thesis, Harvard University, 256 pp.

Clifford, T.N., Barton, E.S., Retief, E.A., Rex, D.C., Fanning, C.M. (1995). A crustal progenitor for the intrusive anorthosite-charnockite kindred of the cupriferous Koperberg Suite, O'okiep district, Namaqualand, South Africa: New isotope data for the country rocks and intrusives. Journal of Petrology. 36, 231–258.

Clifford, T.N., Barton, E.S., Stern, R.A., Duchesne, J. (2004). U-Pb zircon calendar for Namaquan (Grenville) crustal events in the granulite facies terrane of the O'okiep Copper District of South Africa. Journal of Petrology. 45, 669–691.

Clifford, T.N., Barton, E.S. (2012). The O'okiep Copper District, Namaqualand, South Africa: a review of the geology with emphasis on the petrogenesis of the cupriferous Koperberg Suite. Mineral Deposit. 47, 837–857.

Colliston, W.P., Schoch, A.E. (1998). Tectonostratigraphic features along the Orange River in the western part of the Mesoproterozoic Namaqua mobile belt. South African Journal of Geology. 101, 91–100.

Cornell, D.H., Kröner, A., Humphreys, H., Griffin, G. (1990). Age of origin of the polymetamorphosed Copperton Formation, Namaqua-Natal Province, determined by single grain zircon dating. South African Journal of Geology. 93, 709–716.

Cornell, D.H., Thomas, R.J., Moen, H.F.G., Reid, D.L., Moore, J.M., Gibson, R.L. (2006). The Namaqua-Natal Province. In: Johnson, M.R., Anhaeusser, C.R., Thomas, R.J. (Eds.), The Geology of South Africa. Geological Society of South Africa, Johannesburg/Council for Geoscience, Pretoria, pp. 325–379.

Cornell, D.H., Pettersson, Å. (2007). Ion probe dating of the Achab Gneiss, a young basement to the Central Bushmanland Ore District? Journal of African Earth Sciences. 47, 112–116.

Cornell, D.H., Pettersson, Å., Whitehouse, M.J., Scherstén, A. (2009). A new chronostratigraphic paradigm for the age and tectonic history of the Mesoproterozoic Bushmanland Ore District, South Africa. Economic Geology. 104, 385–404.

Cornell, D.C., van Schijndel, V., Simonsen, S., Frei, D. (2014). Geochronology of Mesoproterozoic hybrid intrusions in the Konkiep Terrane, Namibia, from passive to active continental margin in the Namaqua-Natal Wilson Cycle. Precambrian Research. 265, 166–188.

De Beer, C.H., Gresse, P.G., Theron, J.N., Almond, J.E. (2002). The geology of the Calvinia area. 1:250 000 map sheet explanation 3118. Council for Geoscience, p. 92.

De Beer, C.H. (2010). The geology of the Garies area. 1:250 000 map sheet explanation 3017. Council for Geoscience, p. 110.

De Jager, D.H. and Simpson, W. (1962). Wollastonite near Garies, Namaqualand. Annals of the Geological Survey of South Africa. 1, 127–135.

Dey, A., Roy C.S., Mukherjee, S., Sanyal, S., Sengupta, P. (2019). Origin of vesuvianite-garnet veins in calc-silicate rocks from part of the Chotanagpur Granite Gneiss Complex, East Indian Shield: The quantitative P-T-X_{CO2} topology in parts of the system CaO-MgO-Al$_2$O$_3$-SiO$_2$-H$_2$O-CO$_2$ (+Fe$_2$O$_3$, F). American Mineralogist. 104 (5): 744–760

Diener, J.F.A. (2014). Low-P-high-T metamorphism of the Aggeneys Terrane, Namaqua Metamorphic Complex, South Africa. South African Journal of Geology. 117 (1), 31–44.

Diener, J., Thomas, R., and Macey, P. (2017). Pan-African accretionary metamorphism in the Sperrgebiet Domain, Gariep Belt, SW Namibia: Precambrian Research, v. 292, p. 152-162.

Eglington, B.M., Armstrong, R.A. (2003). Geochronological and isotopic constraints on the Mesoproterozoic Namaqua-Natal Belt: evidence from deep borehole intersections in South Africa. Precambrian Research. 125, 179–189.

Eglington, B.M. (2006). Evolution of the Namaqua-Natal Belt, southern Africa – A geochronological and isotope geochemical review. Journal of African Earth Sciences 46, 93–111.

Ferry, J.M. (1992). Regional metamorphism of the Waits River Formation, eastern Vermount: delineation of a new type of giant metamorphic hydrothermal system. Journal of Petrology. 33, 45-94.

Geringer, G.J., Botha, B.J.V., Pretorius, J.J., Ludick, D.J. (1986). Calc-alkaline volcanism along the eastern margin of the Namaqua mobile belt, South Africa – a possible middle Proterozoic volcanic arc. Precambrian Research. 33, 139–170.

Geringer, G.J., Humphreys, H.C., Scheepers, D.J. (1994). Lithostratigraphy, protolithology and tectonic setting of the Areachap Group along the eastern margin of the Namaqua Mobile Belt, South Africa. South African Journal of Geology. 97, 78–100.

Grantham, G.H., Eglington, B.M., Armstrong, R.A. (2000). The geochronology of some lithologies from sheet 3018AC Leliefontein, Namaqua Metamorphic Province Internal Report, Council for Geoscience, p. 17.

Gresse, P.G., Macey, P.H., Smith, H., Hartnady, M.I., Frei, D. (2016). The Pre-Gariep geology east of Rosh Pinah, Karas Region, S. Namibia. Explanation to parts of 1:50 000 Geological Map Sheets 2716DA, 2716DB, 2716DC, 2716DD, 2717CC, 2816BB and 2817AA. Geological Survey of Namibia, Council for Geoscience S.A., pp. 193.

Harley, S.L. and Buick, I.S. (1992). Wollastonite-scapolite assemblages as indicators of granulite pressure temperature-fluid histories: the Rauer Group, East Antarctica. Journal of Petrology. 33, 693-728.

Harley, S.L. and Santosh, M. (1995). Wollastonite at Nuliyam, Kerala, southern India: a reassessment of CO_2-infiltration and charnockite formation at a classic locality. Contributions to Mineral Petrology. 120, 83–94.

Harris, C., and Maboane, L. (2021) The Garies wollastonite deposit, Namaqualand, South Africa: High-Temperature metamorphism of a low-$\delta^{18}O$ skarn? The Canadian Mineralogist. 59, 495-510.

Hartnady, C., Joubert, P., Stowe, C. (1985). Proterozoic crustal evolution in south-western Africa. Episodes 8, 236–244.

Hiroi, Y., Shiraishi, K., Motoyoshi, Y., Katsushima, T. (1987). Progressive metamorphism of calc-silicate rocks from the Prince Olav and Soya Coasts. East Antarctica. Proceedings of the NIPR Symposium on Antarctic Geosciences. 1, 73-97.

Hiroi, Y., Motoyoshi, Y., Shiraishi, K., Hokada, T., Tsuchiya, N., Grantham, G. (2001). Retrograde metamorphism of calc-silicate granulites from Namaqualand, South Africa. NIPR symposium 2001, Abstract (in Japanese).

Hoeffbauer, R. and Spiering, B. (1994). Petrologic phase equilibria and stable isotope fractionations of carbonate-silicate parageneses from granulite-grade rocks of Sri Lanka. Precambian Research. 66, 325-349.

Joubert, P. (1971). The regional tectonism of the gneisses of part of the Namaqualand Metamorphic Complex. Bull. Precambrian Research. Unit, University of Cape Town 10, 220 pp.

Joubert, P. (1986). Namaqualand – a model of Proterozoic accretion? Transactions of the Geological Society of South Africa. 89, 79–96.

Kisters, A.F.M., Potgieter, J.E., Charlesworth, E.G., Anhauesser, C.R., Gibson, R.L., Watkeys, M.K. (1994). Emplacement features of cupriferous noritoids in the Okiep Copper District, Namaqualand, South Africa. Exploration and Mining Geology. 3(3), 297–310.

Locock, A. (2008). An Excel spreadsheet to recast analyses of garnet into end-member components, and a synopsis of the crystal chemistry of natural silicate garnets: Computers and Geosciences. v. 34, no. 12, p. 1769-1780, doi: 10.1016/j.cageo.2007.12.013.

Macey, P.H. (2001). The geology of the region between Garies and Kliprand, southern Namaqualand. 1:50 000 sheets 3018 CA (Buffelsfontein), 3018 CB (Suurdam), 3018 DA (Kliprand) and 3018 DB (Oubees). Council for Geoscience internal report (unpublished).

Macey, P. H., Siegfried, H. P., Minaar, H., Almond, J. E., Botha, P. M. W. (2011). The Geology of the Loeriesfontein Area. Explanation 1: 250 000 scale map 3018 Loeriesfontein, Council for Geoscience, Pretoria, South Africa, pp. 8-52.

Macey, P.H., Minnaar, H., Miller, J.A., Lambert, C., Kisters, A.F.M., Diener, J., Thomas, R. J., Groenewald, C., Indongo, J., Angombe, M., Smith, H., Shifatoka, G., Le Roux, P., Frei D. (2015).

The Precambrian geology of the Warmbad Region, southern Namibia. An interim explanation to 1:50 000 Geological Map Sheets of the 1:250 000 2818 Warmbad sheet. Geological Survey of Namibia and Council for Geoscience of South Africa.

Macey, P.H., Thomas, R.J., Minnaar, H., Gresse, P.G., Lambert, C.W., Groenewaldt, C.A., Miller, J.A., Indongo, J., Angombe, M., Shifotoka, G., Frei, D., Diener, J.F.A., Kisters, A.F.M., Dhansay, T., Smith, H., Doggart, S., Le Roux, P., Harnady, M.I., Tinguely, C. (2017). Origin and evolution of the ~1.9 Ga Richtersveld Magmatic Arc, SW Africa. Precambrian Research. 292, 417–451.

Macey, P., Bailie, R., Miller, J., Thomas, R., de Beer, C., Frei, D., le Roux, P. (2018). Implications of the distribution, age and origins of the granites of the Mesoproterozoic Spektakel Suite for the timing of the Namaqua Orogeny in the Bushmanland Subprovince of the Namaqua-Natal Metamorphic Province, South Africa: Precambrian Research. 312, 68-98.

Marais, J.A.H., Agenbacht, A.L.D., Prinsloo, M., Basson, W.A. (2001). The geology of the Springbok area. 1:250 000 map sheet explanation, sheet 2916. Council for Geoscience, p. 103.

McCourt, S., Armstrong, R.A., Grantham, G.H., Thomas, R.J. (2006). Geology and evolution of the Natal belt, South Africa. Journal of African Earth Sciences. 46, 71–92.

McClung, C.R. (2006). Basin analysis of the Mesoproterozoic Bushmanland Group of the Namaqua metamorphic province, South Africa: Ph.D. thesis, University of Johannesburg. (Unpublished).

Miller, R. McG. (2008). The Geology of Namibia Volume 1 Archaean to Mesoproterozoic, Geological Survey, Windhoek, Namibia.

Moecher, D.P. and Essene, E.J. (1990). Phase equilibria for calcic scapolite, and implications of variable Al-Si disorder for P-T, T-X_{CO_2}" and a-X relations. Journal of Petrology. 31, 997-1024.

Moen, H.F.G. (1999). The Kheis Tectonic Subprovince, southern Africa: a lithostratigraphic perspective. South African Journal of Geology. 102 (1), 27–42.

Moen, H.F.G., Toogood, D.J. (2007). The Geology of the Onseepkans area. Map and explanation, sheet 2818 Onseepkans (1:250 000), Council for Geoscience, p. 101.

Motoyoshi, Y, Thost, D.E., Hensen, B.J. (1991). Reaction textures in calc-silicate granulites from the Bolingen Islands, Prydz Bay, East Antarctica: implications for the retrograde P-T path. Journal of Metamorphic Geology. 9, 293-300.

Nowicki, T.E., Frimmel, H.E., Waters, D.J. (1995) The occurrence of osumilite in pelitic granulites of the Namaqualand metamorphic complex, South Africa. South African Journal of Geology. 98, 191–201.

Pettersson, Å., Cornell, D.H., Moen, H.F.G., Reddy, S., Evans, D. (2007). Ion-probe dating of 1.2 Ga collision and crustal architecture in the Namaqua-Natal Province of southern Africa. Precambrian Research. 158, 79–92.

Pettersson, Å. (2008). Mesoproterozoic crustal evolution in Southern Africa, PhD thesis, Gothenburg University, A117; http://gupea.ub.gu.se/handle/2077/17269.

Raith, J.G and Harley, S.L. (1998). Low-P/high-T metamorphism in the Okiep Copper District, western Namaqualand, South Africa. Journal of Metamorphic Geology. 16, 281–305.

Raith, J.G., Cornell, D.H., Frimmel, H.E., De Beer, C.H. (2003). New insights into the geology of the Namaqua Tectonic Province, South Africa, from ion probe dating of detrital and metamorphic zircon. The Journal of Geology. 111, 347–366.

Robb, L.J., Armstrong, R.A., Waters, D.J. (1999). Nature and duration of mid-crustal granulite-facies metamorphism and crustal growth: evidence from single zircon U-Pb geochronology in Namaqualand, South Africa. Journal of Petrology. 40, 1747–1770.

Reid, D.L. (1979). Total rock Rb-Sr and U-Th-Pb isotopic study of Precambrian metavolcanic rocks in the lower Orange River region, southern Africa. Earth Planet. Science Letters Journal. 42, 368–378.

Reid, D.L. (1997). Sm–Nd age and REE geochemistry of Proterozoic arc-related igneous rocks in the Richtersveld Subprovince, Namaqua Mobile Belt, southern Africa Journal of African Earth Sciences. 24, 621–633.

Rose, A.W. and Burt, D.M. (1979). Hydrothermal alteration. In: Barnes, H.L. (Ed.), Geochemistry of Hydrothermal Ore Deposits: New York. John Wiley and Sons, United States, pp. 173–235

Rudnick, T.K. (2016). The Genesis of the Swartberg Base-Metal Sulphide Deposit, South Africa. MSc. Dissertation (unpubl.). Stellenbosch University. p. 207.

Satish-Kumar, M., Santosh, M., Yoshida, M. (1995). Reaction textures in calc-silicates as guides to the pressure- temperature-fluid history of granulite facies terrains in east Gondwana. Journal of Geosciences. 38, 89-114.

Satish-Kumar, M. and Harley, S. L. (1998). Reaction textures in scapolite wollastonite grossular calc-silicate rock from the Kerala Khondalite Belt, Southern India: evidence for high-temperature metamorphism and initial cooling. Lithos, 44, 83-99.

Satish-Kumar, M., Motoyoshi, Y., Suda, Y., Hiroi, S., Kagashima, S. (2006). Calc-silicate rocks and marbles from Lutzow-Holm Complex, East Antarctica, with special reference to the mineralogy and geochemical characteristics of calc-silicate mega boudins from Rundvagshetta. National Institute of Polar Research. 19, 37-61.

Schmitz, M.D. and Bowring, S.A. (2004). Lower crustal granulite formation during Mesoproterozoic Namaqua-Natal collisional orogenesis, southern Africa. South African Journal of Geology. 107, 261–284.

Seto, Y., Ohi, S., Shimobayashi, N., Kitamura, M., Miyake, A., Hiroi, Y., Grantham, G. (2006). Clinopyroxene exsolution in wollastonite from Namaqualand granulite, South Africa. American Mineralogist. 91, 446–450.

Spear, F.S. (1995). Metamorphic phase equilibria and pressure-temperature-time paths. Washington, D.C.: Mineralogical Society of America, p. 799.

Spreadsheets. (2011). https://www.gabbrosoft.org/spreadsheets

Thomas, R.J., Agenbacht, A.L.D., Cornell, D.H., Moore, J.M. (1994). The Kibaran of southern Africa: tectonic evolution and metallogeny. Ore Geology Reviews. 9, 131–160.

Thomas, R.J., de Beer, C.H., Bowring, S.A. (1996). A comparative study of the Mesoproterozoic late orogenic porphyritic granitoids of southwest Namaqualand and Natal, South Africa. Journal of African Earth Sciences. 23, 485–508.

Thomas, R.J., Macey, P.H., Spencer, C., Dhansay, T., Diener, J.F.A., Lambert, C.W., Frei, D., Aguno, A. (2016). The Sperrgebiet Domain, Aurus Mountains, SW Namibia: A ~2020-850 Ma window within the Pan-African Gariep Orogen. Precambrian Research. 286, 35–58.

Valley, J. W., Peacor, D. R., Bowman, J. R., Essene, E. J., Allard, M. J. (1985). "Crystal chemistry of a Mg-vesuvianite and implications of phase equilibria in the system $CaO-MgO-Al_2O_3-SiO_2-H_2O-CO_2$." Journal of Metamorphic Geology. 3(2), 137-153.

van Aswegen, G. (1983). The Gladkop Suite – the grey and pink gneisses of Steinkopf. In: Botha, B.J.V. (Ed.), Namaqualand Metamorphic Complex. Special Publications of the Geological Society of South Africa. 10, 31–44.

van Niekerk, H.S. (2006). The Origin of the Kheis Terrane and its relationship with the Archean Kaapvaal Craton and the Grenvillian Namaqua Province in Southern Africa. PhD thesis (unpubl.). University of Johannesburg, Johannesburg, pp. 241.

Waters, D.J. (1986). Metamorphic zonation and thermal history of pelitic gneisses from western Namaqualand, South Africa. Transactions of the Geological Society of South Africa. 89, 97–102.

Waters, D.J. (1988). Partial melting and the formation of granulite facies assemblages in Namaqualand, South Africa. Journal of Metamorphic Geology. 6, 387–404.

Waters, D.J. (1989). Metamorphic evidence for the heating and cooling path of Namaqualand granulites. In: Daly, J.S., Cliff, R.A., Yardley, W.D. (Eds.), Evolution of Metamorphic belts. Special Publications of the Geological Society., London 46, pp. 357–363.

Waters, D.J. (1991). Spinel-quartz granulites: phase relations, and implications for crustal processes. European Journal of Mineralogy, 3, 367–386.

Whitney, D. and Evans, B. (2010). Abbreviations for Names of Rock-Forming Minerals. American Mineralogist. 95, 185-187.

Winter, J.D. (2010). Principles of Igneous and Metamorphic Petrology, 2nd Edition. New Jersey: Prentice-Hall, pp.702.

Woolf, K. (2017). Petrology of calc-silicate lens in high-grade felsic gneiss, Kliprand, Western Cape province. Hons. Thesis (unpubl.), University of the Western Cape. p. 11-12.

Zelt, G.A. (1980). Granulite-facies metamorphism in Namaqualand, South Africa. Precambrian Research, 13, 253–274.

Appendix: 1

Instrument: JEOL-8230 Superprobe housed at the Shared Instrument Facility (SIF) of Louisiana State University (LSU).

Operating conditions: 15 kV, 20 nA (100 nA for titanite), focused beam except for vesuvianite (5 micron) and titanite (10 micron).

Standards (20 sec on peak, 10 sec on background, unless otherwise indicated):

Garnet:

Fe, Al, Si Almandine

Mn rhodonite

Cr chromite

Mg, Ca diopside

Ti rutile

Pyroxene (used for wollastonite and epidote):

Si, Mg, Ca diopside

Fe hypersthene

Mn rhodonite

Ti rutile

Cr chromite

Na jadeite

Al augite

K sanidine

Vesuvianite (amphibole setup, also used for apophyllite in NA-200):

Fe, Si, almandine

Mn rhodonite

Ti rutile

Cr chromite

Na albite

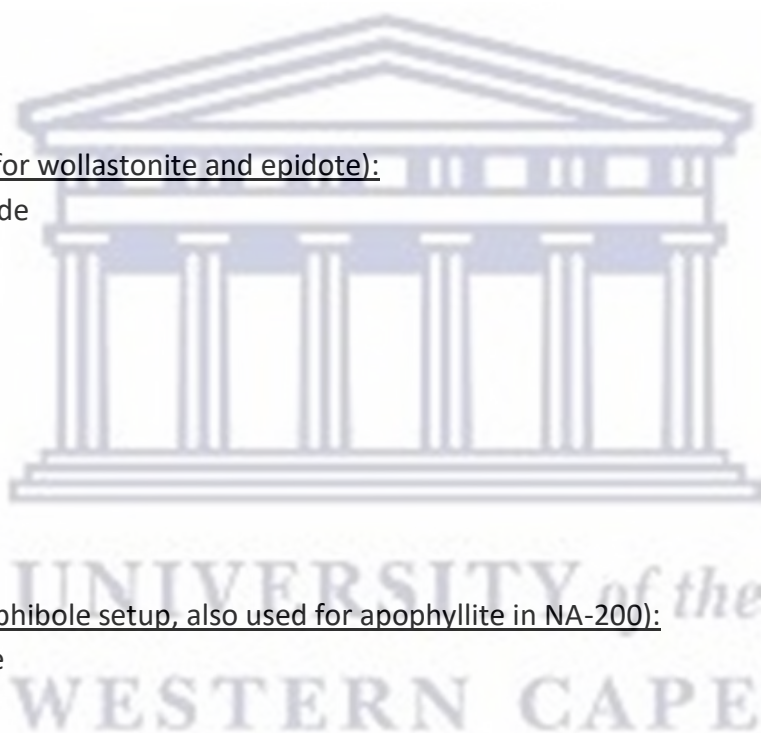F fluorite

Al hornblende

Mg, Ca diopside

K sanidine

Cl tugtupite

Titanite:

Fe, Al almandine

Ti rutile peak: 10s, background 5 s

Ca diopside peak: 10s, background 5 s

F fluorite
Si diopside peak 10 s, background 5 s
Zr zircon peak 60s, background 60s

Element mapping:

15 kV, 100 nA

5 micron step size, 50 msec dwell time (100 msec dwell time for 2nd run of mapping in July 2020).